

**RHEOLOGICAL PROPERTIES OF NON-EQUILIBRIUM
THIN POLYMER FILMS VIA DEWETTING FOR
ADVANCED NANOPHOTONIC SYSTEMS**

BY

MULAMA AUSTINE AMUKAYIA

**A THESIS SUBMITTED IN FULFILMENT OF THE
REQUIREMENTS FOR THE DEGREE OF DOCTOR OF
PHILOSOPHY IN PHYSICS**

SCHOOL OF PHYSICAL AND BIOLOGICAL SCIENCES

MASENO UNIVERSITY

© 2021

DECLARATION

I, **Mulama Austine Amukayia, PHD/SC/00001/2015** declare that the work presented in this thesis to the School of Graduate Studies at Maseno University is my original work. All the experimental work reported within this thesis has been carried out by the author in the Institute of Physics, Prof. Dr. Günter Reiter's Experimental Polymer Physics Group at the Albert-Ludwigs-University of Freiburg (Germany) between October 1, 2017 and September 29, 2019. No part of this thesis has been submitted or presented for an award to Maseno University or any other institution of higher learning.

Sign:  **Date: 24. 02. 2021**

This thesis has been submitted to the School of Graduate Studies with our approval as supervisors:

1. Prof. Dr. Günter Reiter

Experimental Polymer Physics Group,
Institute of Physics,
Albert-Ludwigs-University of Freiburg,
Germany.

Sign:  **Date: 24.02.2021**

2. Prof. Andrew Odhiambo Oduor

Condensed Matter Physics Group,
Department of Physics and Materials Science,
School of Physical and Biological Sciences,
Maseno University,
Kenya.

Sign:  **Date: 24.02.2021**

ACKNOWLEDGEMENT

First, I take this opportunity to thank the Almighty for the gift of life and all the blessings He has always directed towards me. Second, I sincerely thank my supervisors: Prof. Dr. Günter Reiter and Prof. Andrew O. Oduor for introducing me to the new field of science: Soft Matter Physics. I have gained an incredible amount of knowledge from them and have been encouraged from the inception to the completion of my PhD studies. Their supervision has prepared me for the challenges I will face in my future research. Their continuous support, positive criticisms, suggestions, patience, help, encouragement, guidance and leadership qualities have helped me to develop solid scientific attitude, knowledge and skills. I particularly thank Prof. Reiter for accepting me as one of his PhD students and giving me an opportunity to work in his dynamic Experimental Polymer Physics Group (Albert-Ludwigs-University of Freiburg, Germany) where all my experimental work was done. Prof. Reiter provided invaluable guidance and tips along the way, and created many shortcuts through the bureaucracy just for me! During my stay at his Group, I have learnt a lot about dynamics of polymer physics in general. In particular, I wish to thank him for the opportunities he gave me to present my work at the weekly departmental seminars and international conferences where I interacted with reknown experts in soft matter physics and made great connections. I will never forget his assistance, and am deeply indebted to him. I also thank Prof. Dr. Rolf Mülhaupt's Group (Department of Chemistry-University of Freiburg) for providing us with poly(*para*-methylstyrene) polymers used in this work.

I would like to thank the following Members of the Experimental Polymer Physics Group at the University of Freiburg for their fruitful discussions, encouragements, advice and support for the two years I spend with them: Ms. Susanne Brendl, Mrs. Silvia Siegenführ, Mrs. Barbara Heck, Mrs. Stefanie Dold, Mr. Konstantinos Roumpos (Kostas), Mr. Yaser Alshetwi, Mr.

Brahim Bessif, Mr. Tianyu Wu, Mr. Pengu Xu, Ms. Emna Khechine, Ms. Abhijna Das, Dr. Farzad Ramezani, Dr. Sivasurender Chandran (Siva), Dr. Pradipkanti D. Lairenjam (Kanti), Dr. Sumit K. Majumder, Dr. Purushottam Poudel, Dr. Thomas Pfohl and Dr. Renate Reiter. I particularly extend my gratitude to the wonderful works of the following techologists: Silvia, Stefanie and Barbara for the trainings (use of X-ray diffractometry, atomic force microscopy, scanning transmission electron microscopy, digital optical microscopy, differential scanning calorimetry, vacuum systems and UV-Vis optical microscopy) they took me through and always being available for technical assistance during performance of my experiments.

My PhD studies would not have come to an end without some good friends and lecturers in the Physics and Materials Science department at Maseno University-Kenya for standing by my side. I would like to thank Mr. Jack Okumu, Dr. George E. Omondi, Dr. Stephen O. Onyango, Dr. George O. Onyinge, Dr. Henry O. Otunga, Prof. Joseph A. Omolo and Prof. Herick Othieno. I am thankful to my mentor Prof. Reccab M. Ochieng' (University of Zambia) for always encouraging me to face life challenges with a clear and focused mind. The non teaching staff at the Physics and Materials Science department (Maseno University) is thanked for its support.

I thank my parents and siblings for their infinite love, sacrifice and support throughout my life. My sincere gratitude goes to my love Mrs. Betty N. Amukayia and my lovely children: Faustino (Fau), Natalie (Nata) and Aryana (Ari) for their continous support, encouragement, patience and love, which brought me so much happiness, courage and strength.

Finally, I would like to thank the National Commission for Science, Technology and Innovation (NACOSTI-Kenya) (Now National Research Fund-Kenya) for a grant offered to me (2016-2019) and the Deutscher Akademischer Austauschdeinst (DAAD) for the bi-nationally supervised scholarship (2017 – 2019) that helped complete the work with ease. In

addition, I would like to thank Maseno University for offering me tutorial fellowship and tuition fee waver for my PhD studies.

DEDICATION

I dedicate this work to my mother Mrs. Sapientia Khadiala Mulama and my late father Mr. Lawrence Mulama Amusibwa. Although my father did not live to see the final form of this work, I pray for his soul to rest in eternal peace.

ABSTRACT

The quest for increasing complex film architecture and multiphase systems and the continuous demands for enhanced performance, require a reliable assessment of stress on a submicron scale from spatially resolved techniques. Despite enormous efforts on production of well-controlled polymer nanostructures using direct focused methods such as multistage e-beam, no clear relationship among preparation parameters, rheological and morphological properties has been found. Further, there is inadequate information on the rheological properties of polystyrene (PS) when a nonpolar methyl group is introduced to the phenyl ring of styrene monomers to give rise to poly(*para*-methylstyrene) (PpMS) yet these monomers have advantages of strength and stability in comparison to styrene. The study investigated the influence of preparation parameters, dewetting temperature (T_{dew}) and isotactic PS (iPS) blending dynamics on rheological properties of isotactic PpMS (iPpMS) films spin-coated on slippery silicon substrates via dewetting. Based on its simplicity and effectiveness, dewetting of a thin polymer film has gained attention as a feasible process for improving the scalability and productivity. Further characterization on the spin-coated films was done by optical microscopy (OM), atomic force microscopy (AFM), X-ray diffractometer (XRD) and differential scanning calorimeter (DSC). No characteristic peaks were observed on the XRD spectroscopy, implying that iPpMS films were dominated by amorphous properties. However, a weak peak was noted at $\sim 23^\circ$ as an indication of one-dimensional chain – chain processes taking place in iPpMS films. Thinner films (≤ 140 nm) exhibited high residual stresses accompanied by shorter relaxation times compared to thicker films (> 140 nm). The amount of residual stress was not affected by T_{dew} at which dewetting was performed. Correspondingly, the shear modulus of iPpMS films was found to decrease monotonically with increasing temperature which might be related to the reduction of the activation energy for molecular relaxations. An activation energy ranging from 60 ± 10 kJ/mol (pure iPpMS) to 90 ± 10 kJ/mol (pure iPS) was obtained. It is clear that the activation energies characterizing the relaxation of preparation-induced residual stresses seem not to be affected by the size of the side groups. However, in comparison to iPS, iPpMS exhibited reduced energy barrier for flow indicating that presence of transient clusters of monomers have a short lifetime in iPpMS. The experiments suggest that preparation-induced residual stresses affect material properties such as elastic modulus and viscosity of iPpMS as a function of temperature. The results of this study will be useful in production of advanced nanophotonics such as biosensor chips and nanoantennas.

TABLE OF CONTENT

TITLE.....	i
DECLARATION	ii
ACKNOWLEDGEMENT	iii
DEDICATION.....	vi
ABSTRACT.....	vii
TABLE OF CONTENT	viii
LIST OF ABBREVIATIONS AND SYMBOLS	xii
LIST OF TABLES	xv
LIST OF FIGURES	xvi
LIST OF APPENDICES.....	xx
LIST OF PUBLICATIONS	xxi
CHAPTER ONE: INTRODUCTION	1
1.1 Background	1
1.2 Problem statement.....	7
1.3 Study objectives	7
1.3.1 General objective.....	7
1.3.2 Specific objectives.....	8

1.4 Justification of the study	8
1.5 Significance of the study	9
1.6 Assumptions of the study	10
1.7 Limitations of the study.....	10
CHAPTER TWO: LITERATURE REVIEW	11
2.1 Introduction	11
2.2 Basic information about polymer materials	11
2.3 Rheology and mechanical properties of polymers	13
2.3.1 Maxwell model	15
2.3.2 Kelvin-Voigt model	17
2.3.3 Standard linear solid model	17
2.4 Fundamentals of dewetting dynamics of thin polymer films	19
2.5 Previous studies: Rheological properties of thin polymer films via dewetting.....	27
2.5.1 Effect of preparation parameters and dewetting temperature.....	27
2.5.2 Blending dynamics in polymer materials	29
2.6 Nanophotonics in thin polymer films.....	33

CHAPTER THREE: MATERIALS AND EXPERIMENTAL TECHNIQUES.....	37
3.1 Introduction	37
3.2 Materials.....	37
3.3 Silicon wafer preparation and properties	38
3.4 Solution preparation	39
3.4.1 Concentration variation of isotactic poly(<i>para</i> -methylstyrene) (iPpMS).....	39
3.4.2 Isotactic poly(<i>para</i> -methylstyrene) (iPpMS) blend solution preparation.....	40
3.5 Thin film formation by spin-coating technique.....	41
3.6 Experimental methods.....	43
3.6.1 Thin film dewetting by optical microscopy (OM).....	44
3.6.2 Differential scanning calorimeter (DSC) measurements.....	45
3.6.3 Atomic force microscopy (AFM) technique	46
3.6.4 X-ray diffraction (XRD) spectroscopy technique	48
3.7 Measurement of hole radius, rim width and corresponding velocity.....	48
CHAPTER FOUR: RESULTS AND DISCUSSION	51
4.1 Introduction	51
4.2 Rheological properties of isotactic poly(<i>para</i> -methylstyrene) (iPpMS) films.....	51

4.2.1 Effect of spin-coating speed and solution concentration.....	54
4.2.1.1 Variation of spin-coating speed.....	54
4.2.1.2 Influence of solution concentration.....	61
4.2.2 Dynamics of dewetting temperature.....	73
4.2.3 Analysis of dewetting dynamics in iPpMS –iPS blend system.....	87
CHAPTER FIVE: CONCLUSIONS AND RECOMMENDATIONS	105
5.1 Introduction.....	105
5.2 Conclusions.....	105
5.3 Recommendations.....	107
5.3.1 Recommendations based on the study.....	107
5.3.2 Recommendations for further studies.....	109
REFERENCES.....	110
APPENDICES.....	121

LIST OF ABBREVIATIONS AND SYMBOLS

LIST OF ABBREVIATIONS

PS	polystyrene
aPS	atactic polystyrene
aPpMS	atactic poly(<i>para</i> -methylstyrene)
iPS	isotactic polystyrene
iPpMS	isotactic poly(<i>para</i> -methylstyrene)
iPP	isotactic polypropylene
PaMS	poly(<i>alpha</i> -methylstyrene)
PS-<i>b</i>-PMMA	polystyrene-block-poly(methylmethacrylate)
PET	polyethylene terephthalate
PTFE	polytetrafluoroethylene
PPO	poly(phenylene oxide)
PB	poly(butadiene)
dPS	deuterated atactic polystyrene
PDMS	polydimethylsiloxane
PC	polycarbonate

ABS	acrylonitrile butadiene styrene
UCST	upper critical solution temperature
PDI	polydispersity index
WLF	William – Landel - Ferry
CCD	charge - coupled device
UV	ultraviolet
OM	optical microscope
DSC	differential scanning calorimeter
AFM	atomic force microscope
XRD	X-ray diffractometer
3D	3-dimensional
2D	2-dimensional
M_w	molecular weight
M_e	entanglement molecular weight

LIST OF SYMBOLS

Si	silicon
SiO₂	silicon IV oxide

O₃	ozone
H₂O	water
Cu	copper
ε	strain
θ	contact angle
σ	stress
ω	angular speed
η	viscosity
t	time
G	shear modulus
v	velocity
γ	surface tension
λ	wavelength
T	temperature
τ	relaxation time
w	rim width
R	hole radius

LIST OF TABLES

Table	Caption	Page
4.1	Mean values of \overline{B}_v , \overline{B}_w for different iPS content	95

LIST OF FIGURES

Figure	Caption	Page
2.1	Mechanical models' arrangement representing viscoelastic behaviour of polymers.	15
2.2	Optical micrographs of typical dewetting patterns developing in a 200 nm isotactic poly(<i>para</i> -methylstyrene) (iPpMS608K) thin film.	20
2.3	Optical micrograph of a typical dewetting hole developing in a 200 nm iPpMS608K film and the corresponding cross-sectional profile of the rim.	21
2.4	Boundary conditions for a fluid moving over a surface showing no slip, partial slip and full slip conditions.	26
3.1	Silicon wafer preparation procedure.	39
3.2	The image of the spin-coater used to prepare polymer films.	41
3.3	A typical set up for spin-coating process.	43
3.4	Interference colors as a function of film thickness for a polystyrene film.	43
3.5	A set up showing dewetting process of a 200 nm iPpMS608K film.	45
3.6	Measurement of film thickness and contact angle of iPpMS608K films.	47
3.7	A demonstration on how the hole radius and rim width are measured of iPpMS608K films.	50
4.1	Heat flow as a function of temperature, XRD intensity as a function of 2θ , and film thickness as a function of solution concentration and spin-coating speed of iPpMS608K films of different molecular weight.	52
4.2	Optical micrographs showing nucleated holes obtained from spin-coating a 14 mg/ml of solution at different spin-coating speeds dewetting at 170 °C.	54
4.3	Dewetting hole radius, dewetting velocity and rim width as functions of dewetting time for the first dewetting holes of iPpMS608K films at a constant concentration and different spin-coating speeds dewetting at 170 °C.	56
4.4	Initial dewetting velocity as a function of incubation time, normalized dewetting velocity as a function of reduced time, the ratio of total stress to	59

	capillary stress and relaxation time as functions of spin-coating speed of <i>iPpMS608K</i> films dewetting at 170 °C.	
4.5	Optical micrographs showing nucleated holes obtained from spin-coating different solution concentrations at 500 rpm dewetting at 170 °C.	62
4.6	Dewetting hole radius, dewetting velocity and rim width as functions of dewetting time for the first dewetting holes of <i>iPpMS608K</i> films prepared from different solution concentrations but at constant spin-coating speed dewetting at 170 °C.	63
4.7	Initial dewetting velocity, maximum rim width as functions of incubation time, the ratio of total stress to capillary stress as a function of film thickness of <i>iPpMS608K</i> films dewetting at 170 °C.	65
4.8	Relaxation times as a function of dewetting temperature and as a function of reciprocal dewetting temperature for <i>iPpMS608K</i> films prepared from different solution concentrations but at constant spin-coating speed.	68
4.9	Dewetting velocity as a function of dewetting time, maximum dewetting velocity as a function of film thickness, combined hole radius and velocity as a function of dewetting time for $t_{inc} \gg \tau_{rel}$, and estimated slip length as a function of dewetting temperature.	70
4.10	Calculated viscosity as a function of inverse dewetting temperature.	73
4.11	Random nucleation of dewetting holes at different incubation times of a 200 nm <i>iPpMS608K</i> film.	74
4.12	Temporal evolution of a dewetting hole of a 200 nm <i>iPpMS608K</i> film at a dewetting temperature of $T_{dew} = 220$ °C.	76
4.13	Radius of dewetting holes, corresponding dewetting velocity, width of the rim as functions of dewetting time of <i>iPpMS608K</i> films.	77
4.14	The initial dewetting velocity and the maximum width of the rim as functions of incubation time for holes nucleated progressively of a 200 nm <i>iPpMS608K</i> film dewetting at 210 °C.	79
4.15	A plot of characteristic relaxation times and τ_{rep}, τ_r as functions of T_{dew}^{-1} of 200 nm <i>iPpMS608K</i> films.	80

4.16	Representation of the ratios B_v and B_w as functions of dewetting temperature for the earliest appearing dewetting holes of 200 nm iPpMS608K films.	82
4.17	Initial dewetting velocity as a function of T_{dew}^{-1} for dewetting holes nucleated at increasing t_{inc} .	83
4.18	Ratio of $R(t_{\text{dew}})/2w(t_{\text{dew}})$ as a function of $w(t_{\text{dew}})$ and ε_{max} as a function of T_{dew} for the earliest nucleated dewetting holes and of 200 nm iPpMS608K films.	85
4.19	$G(T_{\text{dew}})$ as a function of T_{dew} and $G(T_{\text{dew}}) \cdot \tau(T_{\text{dew}})$ as a function of T_{dew}^{-1}	86
4.20	Optical micrographs showing nucleated holes obtained from a 200 nm iPpMS608K – iPS400K films at different iPS400K content	88
4.21	Optical micrographs and AFM images for the 95 % iPpMS608K – 5 % iPS400K binary system dewetting at $T_{\text{dew}} = 240$ °C.	89
4.22	$R(t_{\text{dew}})$, $v_{\text{dew}}(t_{\text{dew}})$ and $w_{\text{dew}}(t_{\text{dew}})$ as functions of dewetting time of 200 nm iPpMS608K – iPS400K blend films dewetting at $T_{\text{dew}} = 240$ °C.	90
4.23	$v_i(t_{\text{inc}})$ and $w_{\text{max}}(t_{\text{inc}})$ as functions of incubation time for 200 nm iPpMS608K – iPS400K blend films of varying iPS400K content dewetting at $T_{\text{dew}} = 240$ °C.	92
4.24	Normalized initial dewetting velocity and normalized maximum rim width as functions of reduced incubation time for 200 nm iPpMS608K – iPS400K blend films of varying iPS400K content dewetting at $T_{\text{dew}} = 240$ °C.	93
4.25	Ratios B_v , B_w as functions of T_{dew} for 200 nm iPpMS608K – iPS400K blend thin films of varying iPS400K content.	94
4.26	Relaxation times τ_v , τ_w as functions of iPS400K content for 200 nm iPpMS608K – iPS400K blend films.	96
4.27	Relaxation time as a function of $1000/T_{\text{dew}}$ for 200 nm iPpMS608K – iPS400K blend films and activation energy as a function of iPS400K content.	97
4.28	Initial dewetting velocity of the earliest nucleated dewetting holes, limiting values of $v_i(0)$ and $v_i(\infty)$, respectively, as functions of $1000/T_{\text{dew}}$ for	99

- dewetting holes at increasing iPS400K content. Ratio $v_i(0)/v_i(\infty)$ as a function of the iPS400K content.
- 4.29** $R(t_{\text{dew}})/2w(t_{\text{dew}})$ as a function of $w(t_{\text{dew}})$ for the earliest nucleated dewetting holes of 200 nm iPPMS608K - iPS400K films at various iPS400K content and at $T_{\text{dew}} = 240$ °C and ε_{max} as a function of iPS400K content and T_{dew} , respectively. **100**
- 4.30** Capillary stress, residual stress and total stress as functions of iPS400K content for the averaged values of B_v ; shear modulus as a function of T_{dew} at different iPS400K content; effective viscosity as a function of $1000/T_{\text{dew}}$ at different iPS400K content. **101**
- 4.31** Linear plot of activation energy E_η as a function of iPS400K content. **103**

LIST OF APPENDICES

Appendix	Caption	Page
A	Supporting information for chapter one	121
B	Supporting information for chapter two	122
C	Supporting information for chapter three	124
D	Supporting information for chapter four	127

LIST OF PUBLICATIONS

1. **Mulama A. A.**, Roumpos K., Pradipkanti L., Oduor A. O., & Reiter G. (2020). Comparative Dewetting Study of Thin Films of Blends of Isotactic Polystyrene and Isotactic Poly(*para*-methylstyrene). *Macromolecules*, **53**(20), 9122 – 9130.
2. **Mulama A. A.**, Chandran S., Roumpos K., Oduor A. O., & Reiter G. (2019). Dewetting Rheology for Determining Viscoelastic Properties of Non-equilibrium Thin Polymer Films. *Macromolecules*, **52**(20), 7894 – 7903.

CHAPTER ONE

INTRODUCTION

1.1 Background

The demand for nano-structured polymer surfaces for production of device structures that are scalable, sensitive, reproducible and cost-effective for new photonic nanostructures in functional devices (coatings, sensors, optoelectronic devices, electronic chip technology, photovoltaics, fuel cell electrodes and smart adhesives) has led to advanced research on ultrathin polymer films on solid substrates (Atwater, & Polman, 2010; Koenderink, Alù, & Polman, 2015; Makhoulouf, 2014). In most cases, such ultrathin films disclose features that differ from their bulk counterparts with major implications in nanotechnology (Osswald, & Rudolph, 2015, Reiter, 2013).

Polymer materials have unique characteristics that can be monitored and controlled such as lightweight and mechanical flexibility (Bower, 2003; Cho, Robinstein, & Colby, 2003). However, polymers used in industrial applications (e.g., structural engineering) are often subjected to appreciable stresses (Boyd, & Smith, 2007). Consequently, an understanding of preparation-induced residual stresses, changes in morphology and blending dynamics on rheological properties of thin polymer films is important. While previous studies on thin films of atactic polystyrene (aPS) and isotactic polystyrene (iPS) show enhanced viscoelastic properties over a wide range of temperature, they show low impact strength, experience poor crystallization speed, inhomogeneity and the inability to predict temperature and thickness dependence on the microstructure and mechanical properties (Majumder et al., 2018; Poudel et al., 2018a). Previous studies on non-equilibrium dynamics of thin polymer films has also not been well understood due to inconsistent changes in glass transition temperature, T_g (Forrest,

& Dalnoki-Veress, 2001; Kanaya, 2013; Malhotra et al., 1980), unexpected instabilities (Reiter, 2005, 2013; Reiter et al., 2009; Schäffer, 2001; Schäffer et al., 2002), unusual ageing (Raegen et al., 2010), deviations in mobility (Reiter, 1993, 1994), dewetting dynamics (Marquant, 2013; Redon et al., 1991; Reiter et al., 2009; Ziebert, & Raphaël, 2009), deformed chain conformations (Chandran et al., 2019; Fetters, Lohse & Graessley, 1999) and changes in relaxation processes (Al Akhrass et al., 2008; Bodiguel, & Fretigny, 2006; Brochard-Wyart et al., 1997; Vilmin et al., 2006). Despite an increase in literature on dynamics of thin polymer films, the source of these puzzling properties of thin polymer films is still unclear (Chandran, & Reiter, 2016, 2019; Reiter, 2020). At the moment we are still missing a consistent understanding of how rheological properties are affected upon film preparation and confinement (Chandran et al., 2015; Reiter et al., 2009, 2013, 2020; Röttele et al., 2003). As a consequence, a deeper understanding of the processes governing the dynamics and equilibrium statics of a thin film on a fundamental level is needed.

It has been found from previous studies that a possible cause for the non-equilibrium behaviour in thin polymer films originate from sample preparation (Chandran et al., 2017; Chandran, & Reiter, 2019). For instance, rapid solvent evaporation during spin-coating introduces deviations in chain conformations, yielding residual stresses. These stresses, if left unchecked, can severely reduce materials' performance and reliability by inducing mechanical instabilities (Damman et al., 2007; Reiter et al., 2005; Sharma, & Reiter, 1996). There are many factors (i.e., processing routes, thermal history, molecular weight, film thickness, substrate surface energy, temperature and viscoelastic properties of films) that contribute to the generation of residual stresses in thin polymer films, and therefore, understanding and controlling residual stresses is a complex undertaking (Reiter, 2013, 2020).

Although various experimental approaches such as curvature (Kanaya, 2013), sum frequency generation (McGraw et al., 2014; McGraw, Jago, & Dalnoki-Veress, 2011), studies of crazing (Chung et al., 2009) have been used to measure the preparation-induced residual stresses, the required infrastructure is costly in addition to their limited measurement resolution. Moreover, due to the small sample volume, probing the viscoelastic properties of non-equilibrated polymer films in a traditional rheometric device is not a trivial task. In this study, we aim to quantify these residual stresses through dewetting. Dewetting, which is a process of retraction of a fluid from a non-wettable surface it was forced to cover, is a simple technique that can probe rheological properties of polymer materials in thin film form (Al Akhrass et al., 2008; Reiter, 1993, 1994, 2013; Reiter et al., 2005; Reiter, & Tikhomirov, 2001).

Dewetting starts with nucleation and growth of holes, which coalesce to form a tessellation pattern, before breaking into droplets (i.e. from non-equilibrium to equilibrium states) (de Gennes, Brochard-Wyart, & Quéré, 2004). The process of dewetting provides the possibility to measure the response of the molten polymer film to an applied force, generated directly and intrinsically by the film itself. In addition, taking advantage of the fact that dewetting is not initiated at the same time everywhere on a single sample, it allows to follow the evolution of non-equilibrium properties in time, providing for example a means for determining the equilibration time. The biggest advantage of dewetting is that no external input (no externally applied force) is required, eliminating a potential source of uncertainties in measurements. Since the pioneering work of Reiter on dewetting in thin polymer films two decades ago, there has been an increase in research on dewetting in non-crystallizable polymers providing time-dependent information (i.e. elastic modulus, viscosity) in thin polymer films (Kchaou et al., 2018; Reiter, 2005, 2013; Reiter, & Tikhomirov, 2001; Vilmin et al., 2006). However, many

open questions regarding the symmetry breaking of thin films during dewetting still remain unanswered (Reiter, 2020).

Introducing a nonpolar methyl group to the position 4 (or *para*-position) of the phenyl ring of styrene monomers, leads to formation of poly(*para*-methylstyrene) (P4MS or P*p*MS) (Callaghan, & Paul, 1993; Thomas, Grohens, & Jyotishkumar, 2015; Utracki, Leszek, & Wilkie, 2014). Methylstyrene as opposed to styrene monomers have the ability to improve the performance of polymer materials in terms of material strength, chemical modification and stability (Chang, & Woo, 2003a, 2003b). Whereas most of the previous studies focused on dewetting dynamics in atactic or isotactic polystyrene (aPS or iPS) (Chandran et al., 2015; Chandran, & Reiter, 2019), there are few reports on atactic and isotactic P*p*MS (Gunesin, & Gustafson, 1989; Li et al., 2012; Wu et al., 2019). Available reports on aP*p*MS or iP*p*MS films and corresponding blends concentrated on glass transition, miscibility/immiscibility and activation energy dynamics at the expense of rheological behaviour (Wang, Shyong, & Porter, 1995).

Although dewetting studies on aPS and iPS films display excellent mechanical and structural properties, time-temperature dependence of elastic and shear moduli did not come out clearly (Chandran, & Reiter, 2016, 2019; Reiter, 2013). To understand these concepts well, there is need for independent and complementary experiments that may decouple the effects of elastic modulus and preparation-induced residual stresses in thin polymer films. Further, some of the results from previous experiments performed at temperatures less than or slightly above the T_g on aPS or iPS films have shown relaxation times that are much less than the reptation time, τ_{rep} (longest relaxation time), suggesting that the experiments carried out for the preparation-induced residual stresses may not have relaxed completely and the polymer films may not yet be fully equilibrated (Chandran et al., 2015; Chandran, & Reiter, 2016; Kchaou et al., 2018).

Consequently, different experiments need to be performed at elevated temperatures to properly account for the effects of preparation conditions on polymer properties.

Despite the importance of crystallizable and semi-crystallizable polymers in thermo-forming processes in which polymers are subjected to large deformations, inadequate studies have been done on the non-equilibrium rheological dynamics on these kinds of polymers. For instance, although Glück investigated dewetting dynamics in *iPpMS* films and obtained promising results, no details of rheological properties were discussed (Glück, 2016). At this point, we may ask the following questions: Can the non-equilibrium states in *iPpMS* films widen the spectrum of its viscoelastic properties? Is it possible to deduce molecular events underlying the relaxation dynamics in thin *iPpMS* films from relaxation time spectrum? Can the relaxation dynamics be much more pronounced for some relaxing variables than for others? If so, are the differences systematic in any way? Extending these efforts further, we quantitatively determine residual stresses and related preparation-induced changes in material properties (i.e., the elastic modulus, viscosity and activation energy) in spin-coated *iPpMS* films.

Even though polymer blends exhibit property profiles superior to those of individual homopolymers as well as saving material and production costs (Colmenero, & Arbe, 2007; Harismiadis et al., 1996; Thomas, Grohens, & Jyotishkumar, 2015), there is limited information available on the dewetting dynamics on the resulting blend films' stability, morphology, mechanical performance, and composition distribution into one another. One of the reasons could be issues to do with compatibility and equilibrium of solution mixtures in blends which is a challenge (Harismiadis et al., 1996; Wang, Lin & Tseng, 2006). For instance, though faster dewetting was observed for the atactic *PpMS* (*aPpMS*) layer than for the deuterated PS (*dPS*) layer in the *dPS/aPpMS* blend system, to some extent, dewetting process

had to compete with phase separation (Müller-Buschbaum, Gutmann & Stamm, 2000; Müller-Buschbaum et al., 1998).

Despite the fact that polymers of different tacticity in molten states are expected to show similar dynamics, it has been established through dewetting that the viscosity of iPS is higher by orders of magnitude than that of aPS (Chandran et al., 2017; Kchaou et al., 2018). Moreover, the same authors observed an enhanced activation energy for iPS films, which they alluded to the possibility of transient clusters of monomers exhibiting cooperative dynamics in iPS (Chandran et al., 2017; Kchaou et al., 2018). However, the role of tacticity in the dewetting dynamics of iPS films did not come out clearly and it would be interesting to find out the effect of tacticity on the miscibility and dewetting behaviour of the resulting iPS-iPpMS blends. Compared to aPS and iPS polymer films, PpMS films have been found to exhibit low activation energy due to presence of the nonpolar methyl group on the aromatic ring and it would be motivating to find out how the resulting activation energies will be affected by mixing iPS and iPpMS polymers (Colmenero, & Arbe, 2007; Shu, & Woo, 2006; Thomas, Grohens, & Jyotishkumar, 2015). Further, we set out to investigate if the already observed induced transient cooperative process on other monomers within a cluster of oriented segments in iPS exist in the blend of iPS-iPpMS system.

In this study, we performed dewetting experiments to investigate the influence of iPS (of different molecular weight and dispersity) concentrations in the iPpMS matrix and to probe the consequences on the viscoelastic properties of the resulting blends. The blend dynamics between iPS and iPpMS is interesting since it has been established that compared to iPS, iPpMS does not have a clearly identifiable melting temperature (Wu et al., 2019). Furthermore, compared to other polymers, flow in iPS requires cooperative movement of a higher number of segments (Chandran, & Reiter, 2016). Thus, the iPS-iPpMS blend system is expected to

create compositional and configurational disorders compared to pure individual polymer films resulting in relatively better stable structures allowing to widen the range of applications.

1.2 Problem statement

The advancement in electronic chip technology and photonic nanostructures require materials with high dielectric constants, great mechanical strength and ease of processing (Makhlouf, 2014). Although ferroelectric ceramics have high dielectric constants, they are brittle and require high temperature during processing, posing a hindrance to the current integrated circuit technologies (Ye, Zuev & Makarov, 2018). Despite the intensive research on dewetting dynamics in thin polystyrene (PS) films, investigation of the dewetting behaviour when the phenyl ring is substituted with methyl group to give rise to poly(*para*-methylstyrene) (PpMS) films and the influence of tacticity, preparation and post deposition conditions on the viscoelastic properties of PpMS and its blend has not been given attention. Therefore, this study investigates rheological properties of thin isotactic PpMS (iPpMS) films with respect to chain conformations, microscopic compositions, preparation conditions and blending on the dewetting dynamics. This will lead to understanding the basics of their behaviour by influencing and modifying their properties to produce materials which are adaptable to specific applications.

1.3 Study objectives

1.3.1 General objective

To probe the rheological properties of non-equilibrium polymer films via dewetting based on thin isotactic poly(*para*-methylstyrene) (iPpMS) films on slippery silicon wafers prepared by

spin-coating technique to realize the corresponding morphologies and structures for application in nanophotonics.

1.3.2 Specific objectives

- i. To determine the influence of spin-coating speed and solution concentration on the preparation-induced residual stresses, their relaxation and corresponding viscoelastic properties of thin iPpMS films.
- ii. To analyze the influence of dewetting temperature on the relaxation dynamics in thin iPpMS films.
- iii. To determine the influence of iPS content on the rheological properties of iPpMS-iPS blend system.

1.4 Justification of the study

The increasing interest in thin polymer films requires new approaches in order to improve the functional properties for more demanding applications like in electronic chip technology (Makhlouf, 2014). The large molecular weight of most polymers renders them unique properties such as toughness, entanglement and viscoelasticity (Ferry, 1980). In addition, when two or more chemically distinct monomers are used to form the polymers, different properties arise for different applications (Harismiadis et al., 1996; Utracki, 2003)

Although poly(*alpha*-methylstyrene) (P α MS) and poly(*para*-methylstyrene) (PpMS) isomers can be produced by the same synthetic routes, the synthesis of *para* (*p*-) isomer is preferred due to its greater accessibility and compatibility of the functional groups on the produced polymers and that the copolymerization process in which *p*-isomer is involved is extremely clean (i.e. end products are all gases) (Utracki, 2003; Utracki, Leszek, & Wilkie, 2014). In

addition, *p*-methylstyrene is preferred as it leads to production of rigid polymers of pendant methyl repeating units with attractive thermal, mechanical, high-glass transition temperatures, low density, low viscosity and dielectric constants (Stroeks, Paquaij & Nies, 1991)

Despite enormous efforts in understanding the rheological properties in atactic polystyrene (aPS) and isotactic polystyrene (iPS) probed by dewetting process, inadequate information is available on the P*p*MS system (Wu et al., 2019). Additionally, even though there have been considerable efforts to characterize the mechanical properties of nanometre-sized polymer films over the past decades, unfortunately, consensus on the thickness-dependent elastic modulus of polymer films has not been found within the reported results (Damman et al., 2007; Reiter, 2013, 2020; Sunthar, 2010; Vilmin et al., 2006). Therefore, there is need to investigate tinnier details of thin P*p*MS films in terms of production, blending and characterization to help tune the properties to current technological trends. Blending iP*p*MS with available polymers saves money, energy, time and produces blend films whose profiles are complimentary to the useful characteristics of each individual polymers and superior to those of its single homopolymers (e.g. light weight, increased roughening, enhanced ozone resistance, extended service temperature range, improved modulus and hardness) (Thomas, Grohens & Jyotishkumar, 2015).

1.5 Significance of the study

Next generation electronic chip technology in telecommunication and related applications rely on the development of polymer systems with optimized physical properties that are compatible with miniaturized packaging requirements (Sunthar, 2010; Young, & Lovell, 1991). This requires appropriate considerations as to material choice, stability, and long-term ageing behaviour. According to the recently published work by Reiter (Reiter, 2020), the variation

between non-equilibrium and equilibrium state properties of thin polymer films provides polymers with capacities for responding and adapting to changes in environmental conditions and to external stimuli. The author suggests that the deviation represents the ‘memory’ (ability to establish a link between the past and future in terms of material properties) of the polymer films. In this regard, it is important to carefully examine polymer processes (which can help in information encoding!) such as shearing, temperature variations, ageing dynamics, blending, structural modification, relaxation behaviour to tune thin polymer films for future memory chip technology, phase change memory and semiconductor devices.

1.6 Assumptions of the study

To derive viscosity, the following assumptions were considered: The polymer has negligible vapour pressure, exhibit high viscosity, is incompressible, the melt flow is fully developed, steady, isothermal and laminar to ensure mass conservation for the dewetting process to be slow enough to allow simple, time-resolved measurements (Cho, Robinstein, & Colby, 2003; Sunthar, 2010; Reiter, 2013). In addition, the total deformation was considered to consist of a sum of independent elastic and viscous components.

1.7 Limitations of the study

The isotactic poly(*para*-methylstyrene) (iPpMS) polymers used in this study were synthesized in the laboratory. Thus, we could not analyze iPpMS polymers of higher molecular weight (> 608 kg/mol) (increase in entanglement) as they had not been synthesized by the end of the experimental work. Highly entangled polymers would have led to decreased dewetting dynamics of iPpMS films.

CHAPTER TWO

LITERATURE REVIEW

2.1 Introduction

In the following sections, basic description of polymer materials, viscoelasticity and corresponding viscoelastic models, fundamentals of dewetting, review of previous studies and nanophotonics in thin polymer films is provided to set the stage for the current study.

2.2 Basic information about polymer materials

Polymers are macromolecules (consisting of long, flexible, chain-like molecules) made by linking a number of repeating subunits (monomers) through covalent bonds (Cho, Rubinstein & Colby, 2003). The number of monomers (degree of polymerization) can range from ~ 10 up to $\sim 10\,000$ for a typical polymer chain. The length of a chain consists of numbers of monomeric units per chain which when long enough to entangle (interpenetrate neighbouring coils) causes topological constraints responsible for the viscoelastic nature of polymers (de Gennes & Deutsch, 1991; Ferry, 1980). The origin and the nature of entanglement in thin polymer films are still poorly understood (Reiter, 2013, 2020). A flexible polymer chain can acquire many conformations depending upon the interaction between the monomers on the chain, interaction with surrounding chains and how flexible the chain is (Osswald & Rudolph, 2015).

Based on the type of monomers, we can categorize polymers as homopolymers (single species of monomers) (e.g. polystyrene: PS) and copolymers (mixture of species of monomers) (e.g. polystyrene-block-poly(methylmethacrylate): PS-b-PMMA) (Utracki, 2003; Harismiadis et al., 1996). Factors that can lead to changes in the chemical, optical, electrical, structural and physical properties of polymers include but not limited to control of the degree of

polymerization, variation of molecular weight, chemical structures and chain conformations. For instance, some polymer properties may strongly depend on molecular weight (M_w) (e.g. melt viscosity), while others like density are only weakly dependent on M_w (Utracki, Leszek, & Wilkie, 2014; Young, & Lovell, 1991). Polymer melts can be classified into semi-crystalline, glassy, elastic or viscous depending on their intermolecular interactions.

Polymer tacticity decides between semi-crystalline (i.e., isotactic or syndiotactic) and amorphous (i.e., atactic, characterized by the absence of all the crystalline order) conformational states (Sunthar, 2010; Utracki, 2003). Semi-crystalline polymers include linear polyethylene (PE), polyethylene terephthalate (PET), polytetrafluoroethylene (PTFE), isotactic polypropylene (iPP), isotactic polystyrene (iPS) and isotactic poly(*para*-methylstyrene) (iPpMS). Semi-crystalline polymers exhibit benefits in strength, stiffness, chemical resistance and stability compared to amorphous polymers (Bower, 2003). Macroscopic properties of thin polymer films depend on the morphological structures and dynamics, influenced by external conditions such as preparation pathways, temperature, pressure, deformation, physical ageing and blending.

The glass transition temperature T_g , marks the crossover from the equilibrium melt state to the out-of-equilibrium glass. Physical aging, that is the recovery of equilibrium of the glass, in nanoscale confinement has been deeply investigated in recent years (Reiter, 2005, 2013; Reiter et al., 2009; Schäffer et al., 2002). This phenomenon is intimately linked to the thermal glass transition. A T_g decrease indicates the ability of the glass to equilibrate more efficiently. Hence, if confinement dependent T_g is observed, it is obvious to expect deep effects also in the physical aging behaviour (Raegen et al., 2010). It has been established that at higher temperatures than T_g , the diffusive motion of polymer chains takes place. According to Flory (Flory, 1942), when the chain length of a polymer increases, the internal friction between chains sliding past each

other increases. For polymer chains whose molecular weight (M_w) \geq entanglement molecular weight (M_e), the chains start to entangle, and consequently the motion of the chains decreases due to topological constraints around the chains (resembling a tube) which hinders their transverse motion. Subsequently, the chains have to reptate out of the tube. In this case, the viscosity (η) of most polymers has been found to scale linearly with molecular weight such that $\eta \sim M_w^{3.4}$ (Damman et al., 2007).

In the following sub-sections, we establish polymer rheology, viscoelastic mechanical models, dewetting dynamics in thin polymer films and a review of literature on what has been done as regards the viscoelastic properties of dewetted polymer films.

2.3 Rheology and mechanical properties of polymers

Rheology is the science of deformation and flow dynamics in materials. It involves the study of stress-strain relationship of materials. The response of polymers to an applied stress or strain is distinct from elastic solids such as metals and ceramics as it depends upon the rate or time period of loading. This is in contrast to elastic materials which, at low strains, obey Hooke's law and the stress is in most cases proportional to the strain and independent of loading rate (Boyd, & Smith, 2007; Rauscher et al., 2005; Young, & Lovell, 1991). For viscous liquids, their behaviour is best described by Newton's law in which the stress is proportional to the strain-rate and independent of the strain. Behaviour of most polymers lies between elastic solids and viscous liquids. As a result, at low temperatures and high rates of strain they display elastic behaviour whereas at high temperatures and low rates of strain they behave in a viscous manner, flowing like a liquid. Hence, polymers are referred to as viscoelastic materials (Ferry, 1980; Young, & Lovell, 1991). Polymers used in engineering applications are often subjected to stress for prolonged periods of time, but it is not possible to know how a polymer will

respond to a particular load without an understanding of its viscoelastic properties (Ferry, 1980; Gabriele et al., 2006).

In Physics, stress and strain parameters are related by a constitutive law whose relationship can be sought experimentally by measuring how much stress is needed to stretch a given material. Here, the more a material is pulled the more it deforms and for small strain values, this relationship is said to be elastic linear (Hooke's law) consisting of both elastic and viscous components and that the deformation in the polymers can be described by a combination of Hooke's and Newton's laws (Ferry, 1980; Gabriele et al., 2006). The slope of the elastic linear relationship give rise to Young's elastic modulus (E) which is a property of the material. We know that for a linear elastic system obeying Hooke's law, the stress (σ) is directly proportional to strain (ε) such that (Sunthar, 2010; Young, & Lovell, 1991):

$$\sigma = E \cdot \varepsilon \quad (2.1)$$

Differentiation of equation (2.1) with respect to time leads to equation (2.2)

$$\dot{\sigma} = E \cdot \dot{\varepsilon} \quad (2.2)$$

Newton's law describes the linear viscous behaviour through equation (2.3)

$$\sigma = \eta \cdot \dot{\varepsilon} \quad (2.3)$$

where η is the viscosity and $\dot{\varepsilon} = d\varepsilon/dt$ is the strain rate. It should be noted that the equations outlined above apply only at small strain. To clearly formulate elastic and viscous behaviour in polymers, use of viscoelastic mechanical models such as Maxwell, Kelvin-Voigt, Standard linear solid models are important. In this case, the elastic spring of modulus E obeying Hooke's law (eqn. (2.1)) and a viscous dashpot of viscosity, η obeying Newton's law (eqn. (2.3)) are used.

2.3.1 Maxwell model

In polymer science, the mechanical response of polymer systems is poorly represented by either the spring or the dashpot. To better approximate the relaxation behaviour of viscoelastic materials, Maxwell suggested a combination of the spring and the dashpot in series leading to what is currently referred to as the Maxwell's spring-dashpot model (Bodiguel & Fretigny, 2006; Cho, Robinstein, & Colby, 2003; Young, & Lovell, 1991). Consider a spring and a dashpot in series (Fig. 2.1(a)).

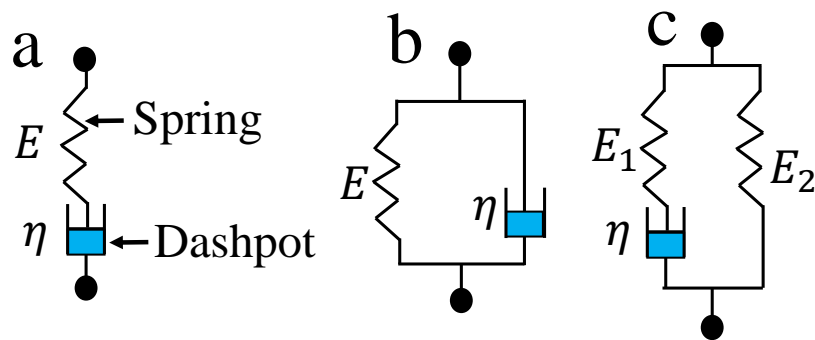


Fig. 2.1: Mechanical models' arrangement representing viscoelastic behaviour of polymers:(a) Maxwell model, (b) Kelvin-Voigt model and (c) Standard linear solid model.

The arrangement in Fig. 2.1(a) is such that the spring and the dashpot are both subjected to the same stress but their deformations are additive (Fleming, & Bower, 2003);

$$\sigma = \sigma_s = \sigma_D \quad (2.4a)$$

$$\sigma_s = E \cdot \varepsilon_s \quad (2.4b)$$

$$\sigma_D = \eta \cdot \dot{\varepsilon}_D \quad (2.4c)$$

$$\varepsilon = \varepsilon_s + \varepsilon_D \quad (2.5)$$

where E is elastic modulus, η is viscosity; σ_s , σ_D ; ε_s , ε_D are stress and strain with respect to spring and dashpot, respectively.

The spring element models time-independent elastic behaviour whereas the dashpot element models time-dependent viscous behaviour. Elastic behaviour in polymer materials is due to strong covalent intramolecular bonds, while viscous behaviour is due to weak intermolecular Van der Waals bonds (Cho, Robinstein, & Colby, 2003). If we differentiate the tensile deformation (eqn. (2.5)) with respect to time once, we obtain:

$$\dot{\varepsilon} = \dot{\varepsilon}_s + \dot{\varepsilon}_D \quad (2.6)$$

In terms of stress term (after dropping the subscripts), eqn. (2.6) becomes:

$$\dot{\varepsilon} = \dot{\sigma}/E + \sigma/\eta \quad (2.7)$$

Equation (2.7) is a linear combination of the deformation rates of the perfectly elastic behaviour of the polymers as given in the time derivative of Hooke's law (first term on the right hand side) and perfectly viscous behaviour as stated in the Newton's law (second term) (Young, & Lovell, 1991). The first term represents the short-time changes in the strain whereas the second term represents the long-time changes in strain. If the deformation is held constant ($\varepsilon = \varepsilon_0$) during the experiment for the total time $t \in (0, t_E)$, then the deformation rate is zero ($\dot{\varepsilon} = 0$). The body will respond to this compression by a change in stress. Therefore, integration of eqn. (2.7) by separation of variables under the above conditions yields (Ferry, 1980):

$$\sigma = \sigma_0 \cdot \exp[-(E/\eta)t] = \sigma_0 \cdot \exp[-t/\tau] \quad (2.8)$$

where $\tau = \eta/E$ is a constant for each Maxwell model and is referred to as relaxation time (the time at which the stress is reduced to $\sim 37\%$ or $(1/e)$ th of the original value), t is the time and we can identify τ/t as the Deborah number ($De = \tau/t$) (Ferry, 1980). Deborah number is used to account for the non-uniform stretch history of a given fluid under flow. If $De \ll 1$, then it means the polymer under consideration relaxes much faster than the fluid packet transverses a characteristic distance, i.e. the fluid packet is said to have 'no memory' of its state at time t

earlier. Further, if $De \sim 1$, then the polymer has not sufficiently relaxed and the state at time t earlier can now influence the motion of the fluid packet. From the foregoing, it is clear that the Maxwell model predicts an exponential decay of stress (stress relaxation).

2.3.2 Kelvin-Voigt model

Kelvin-Voigt model consists of a spring and a dashpot just like in Maxwell model but the elements are in parallel (Fig. 2.1(b)) (Boschetti-de-Fierro et al, 2007; Cho, Robinstein, & Colby, 2003). As a consequence, the strains of the spring and the dashpot are uniform ($\varepsilon = \varepsilon_s = \varepsilon_D$) and the stresses are additive:

$$\sigma = \sigma_s + \sigma_D = E \cdot \varepsilon_s + \eta \cdot \dot{\varepsilon}_D \quad (2.9)$$

Re-arrangement (and dropping the subscripts) of eqn. (2.9) yields:

$$\dot{\varepsilon} = (\sigma - E \cdot \varepsilon) / \eta \quad (2.10)$$

The Kelvin-Voigt model is useful in describing the behaviour during creep where the stress is held constant at $\sigma = \sigma_0$. Hence eqn. (2.10) changes to eqn. (2.11):

$$\dot{\varepsilon} + E \cdot \varepsilon / \eta = \sigma_0 / \eta \quad (2.11)$$

The differential eqn. (2.11) has the following solution:

$$\varepsilon = \sigma_0 \cdot [1 - \exp(-t/\tau)] / E \quad (2.12)$$

From eqn. (2.12), it is clear that the strain rate decreases with time and $\varepsilon \rightarrow \sigma_0/E$ as $t \rightarrow \infty$, representing the correct form of behaviour for a polymer undergoing creep. On the other hand, the model is unsuccessful in predicting the stress relaxation behaviour of a polymer since it fails to show instantaneous response or continued flow under equilibrium stress.

2.3.3 Standard linear solid model

We have observed that Maxwell model describes the stress relaxation of a polymer to a first approximation whereas the Kelvin-Voigt model describes creep. To obtain a combination of

these two phenomena, the standard linear solid model (Fig. 2.1(c)) is considered (Brochard-Wyart et al., 1997; Young, & Lovell, 1991). This model consists of Maxwell model in parallel to an additional spring. Let elastic moduli E_1 and E_2 represent the spring in Maxwell model and the additional spring, respectively (Ferry, 1980). For the Maxwell model;

$$E_1 \cdot \dot{\varepsilon} = \dot{\sigma}_1 + \sigma_1/\tau \quad (2.13)$$

with $\tau = \eta/E_1$. For the additional spring ($\sigma_2 = E_2 \cdot \varepsilon$), we have;

$$E_2 \cdot \dot{\varepsilon} = \dot{\sigma}_2 \quad (2.14)$$

The total stress is $\sigma = \sigma_1 + \sigma_2$ and the constitutive equation will be the sum of equations (2.13) and (2.14):

$$\dot{\varepsilon} \cdot (E_1 + E_2) = \dot{\sigma}_1 + \sigma_1/\tau + \dot{\sigma}_2 \quad (2.15)$$

If we add $E_2 \cdot \varepsilon/\tau$ on the left hand side and σ_2/τ on the right hand side of (2.15), we obtain:

$$\dot{\varepsilon} \cdot (E_1 + E_2) + E_2 \cdot \varepsilon/\tau = \dot{\sigma} + \sigma/\tau \quad (2.16)$$

Equation (2.16) is the differential equation for the standard linear solid model of Fig. 2.1(c). To obtain relaxation function from eqn. (2.16), we take Laplace transform of the differential equation and the fact that the stress and the strain histories are assumed to begin after time zero which may be considered to occur in the remote past (Mainardi, & Spada, 2011; Thomas et al., 2011). Therefore, the relaxation function for the standard linear solid is a decreasing exponential of the form:

$$E(t) = E_2 + E_1 \cdot \exp(-t/\tau) \quad (2.17)$$

To successfully describe relaxation dynamics in thin isotactic poly(*para*-methylstyrene) (iPpMS) and corresponding blends, the study is based on Maxwell model in which the stress is uniformly distributed throughout the system (the spring and the dashpot elements) but the macroscopic strain being the sum of elastic and viscous deformations.

2.4 Fundamentals of dewetting dynamics of thin polymer films

When a large amount of a liquid is dropped onto a solid surface, the liquid can completely cover the surface even if the liquid ‘does not like’ the surface (hydrophobic). In this case, the thick liquid will remain stable due to the effects of gravity. However, when the thickness of the liquid gets thinner (< 100 nm), the spreading of the liquid on the solid surface will be determined by the surface energy and the interfacial energy (between the liquid and the solid surface) (de Gennes, Brochard-Wyart, & Quéré, 2004; Ferry, 1980). The spreading coefficient, S , describes the ability of the drop to spread on or to dewet (retract) from a surface and is related to an imbalance of surface forces such that (Bower, 2003; de Gennes, 1990);

$$S = \gamma_S - (\gamma_{LS} + \gamma_L) \quad (2.18)$$

where, γ_L (liquid-vapor), γ_{LS} (liquid-substrate) and γ_S (substrate-vapor) represent the interfacial tensions which act at the three-phase contact line of a drop, i.e., the line where substrate, film, and environment (e.g., air) meet (Brochard-Wyart, & de Gennes, 2003). For

$S > 0$, a liquid spreads on the (solid) substrate. When $S < 0$, the liquid wets the surface only partially as characterized by a finite contact angle, θ . Using Young’s equation

($\gamma_S = \gamma_{LS} + \gamma_L \cdot \cos(\theta_{eq})$) (Brochard-Wyart et al., 1994, 1997; McGraw et al., 2017) equation

(2.18) leads to $S = \gamma_L (\cos\theta - 1)$. The contact angle is a quantitative measure of the partial wettability of a substrate by a liquid. In general, if a film is forced to cover a non-wettable

substrate, it is at best metastable, also due to residual stresses (Bäumchen, & Jacobs, 2010; Brochard-Wyart et al., 1997).

Dewetting experiments have previously been used to probe velocity-dependent information from a polymer film such as friction (Reiter, 1993, 1994, 2013). In dewetting, the polymer film tries to minimize the contact with the substrate due to balance of driving forces (residual and capillary forces) and dissipative forces (linear frictional forces between fluid and the substrate) leading to a retraction of the film from the substrate at a solid substrate – polymer interface once the film is annealed at a temperature higher than the glass transition temperature ($T_{\text{dew}} > T_g$) (Christensen, & Freund, 2010). Such annealing results in the growth of circular holes exposing the substrate (Fig. 2.2(a)).

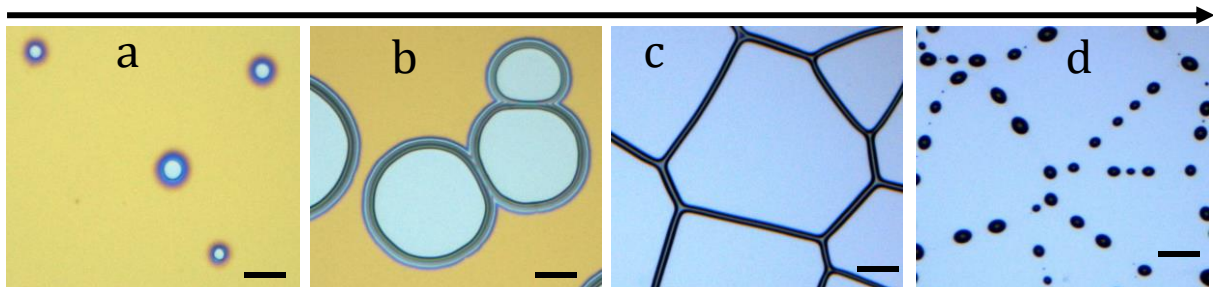


Fig. 2.2: Optical micrographs ($200 \times 200 \mu\text{m}^2$) of typical dewetting patterns developing in a 200 nm isotactic poly(*para*-methylstyrene) (iPpMS) film, showing (a) nucleation and growth of dewetting holes, (b) coalescence of dewetting holes, (c) straight lines of materials formed between the coalesced holes and (d) formation of droplets.

Since we are dealing with films of very small thicknesses and whose dewetting velocities are comparatively small, gravity and inertia are assumed to play minimal role in the dewetting process (de Gennes, Brochard-Wyart, & Quéré, 2004). Wetting is an important process for many applications including adhesion, lubrication, painting, printing, and protective coatings. However, for most applications, dewetting is an unwanted process, because it destroys the applied film (Blossey, 2012).

During the process of retraction of fluid from a substrate there is relative movement of molecules past each other giving rise to viscous dissipation within the fluid. Interfacial friction between the substrate and the fluid leads to accumulation of removed material from the growing hole around the hole (rim formation-[Fig. 2.3\(a\)](#)) characterized by two contact angles θ_{dyn} and ϕ ([Fig. 2.3\(b\)](#)).

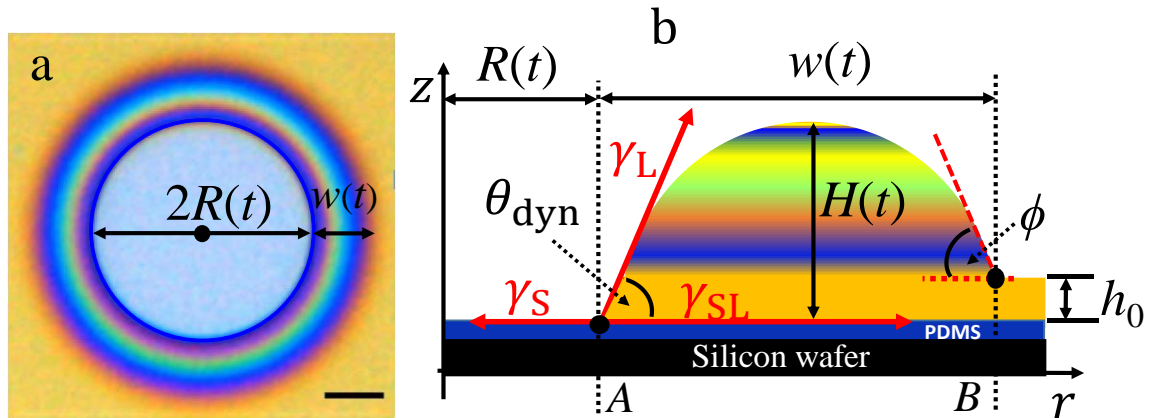


Fig. 2.3: (a) Optical micrograph ($100 \times 100 \mu\text{m}^2$) of a typical dewetting hole developing in a 200 nm isotactic poly(*para*-methylstyrene) (iPpMS) film, showing the dewetted distance ($2R(t)$) and the rim width ($w(t)$). The different interference colours represent the differences in thickness (height). (b) Schematic cross-sectional profile of the rim surrounding a dewetting hole. θ_{dyn} is the dynamic contact angle at the front A and ϕ is the contact angle at the rear position B ; h_0 , $w(t)$, $R(t)$ and $H(t)$ are the film thickness, rim width, radius of the dewetting hole and height of the rim plus the film thickness, respectively: $H(t) = H_{\text{max}}(t) + h_0$; $H_{\text{max}}(t)$ is the maximum height of the rim with respect to the film surface (Vilmin et al., 2006).

The rims form due to mismatch between the rates at which the polymer gets dislodged from the substrate and the rates (which are slower) at which the dislodged polymer gets redistributed to other intact parts of the film. This is a signature of localized accumulation (Marquant, 2013; Reiter, 1993, 1994, 2005, 2013). The morphological details of the rim and its temporal evolution can provide much insight into the slip boundary conditions. For instance, during rim build up, surface tension is only effective on a small part of the rim, thus allowing unusual morphologies and dynamics such as viscoelasticity. The concept of contact angle reflects the balance of cohesive forces (between the liquid molecules) and adhesive forces (between the liquid molecules and the substrate surface) (Chandran et al., 2015; Röttele et al., 2003). Polar

(hydrophilic) surfaces decorated with hydroxyl groups often involve strong adhesive forces and low contact angles. Non-polar (hydrophobic) surfaces like most polymers are characterized by strong cohesive forces and high contact angles (Brochard-Wyart et al., 1994, 1997). Therefore, measurements of the contact angle represent a quick and simple way of obtaining qualitative information about the chemical nature of surfaces.

In dewetting of a viscous fluid, the height profile of the rim is mainly governed by capillary forces acting at the contact line, Laplace pressure and energy dissipation inside the rim, reflected in part by the dynamic contact angle, θ_{dyn} (Brochard-Wyart & de Gennes, 2003). In addition, the changes in size (width and height) of the rim reflect mass conservation, i.e., the dewetted material is collected in the rim (Chandran, & Reiter, 2016, 2019; Reiter, 1993, 1994, 2013). During dewetting, $\theta_{\text{dyn}} \neq \theta_{\text{equ}}$, with θ_{equ} being the contact angle at equilibrium, i.e., for the case where the dewetting velocity is zero. Thus, there exists a net force per unit length of the contact line (uncompensated Young's force) such that $F_{\text{Young}} = -\gamma_S + \gamma_{LS} + \gamma_L \cdot \cos \theta_{\text{dyn}}$ (Brochard-Wyart, & de Gennes, 2003). At equilibrium, we find that $\gamma_S = \gamma_{LS} + \gamma_L \cdot \cos \theta_{\text{equ}}$. Hence, $F_{\text{Young}} = \gamma_L \cdot (\cos \theta_{\text{dyn}} - \cos \theta_{\text{equ}})$. For small values of θ_{dyn} , we can approximate $\cos \theta_{\text{dyn}} \approx 1 - (\theta_{\text{dyn}}^2/2)$ (de Gennes, Brochard-Wyart, & Quéré, 2004). Thus:

$$F_{\text{Young}} = (1/2) \cdot \gamma_L \cdot (\theta_{\text{equ}}^2 - \theta_{\text{dyn}}^2) \quad (2.19)$$

If v is the mean velocity of the contact line and η the viscosity of the liquid, assuming that the shape of the rim is governed by Laplace pressure and that viscous forces inside the rim are sufficiently low to allow for rapid equilibration of possible pressure fluctuations, we can approximate the shape of the cross-section of the liquid rim by a circular segment. Here, the Laplace pressure is given by $P_L = 2 \cdot \gamma_L \cdot \kappa$ (γ_L is the surface tension of the liquid and κ is the curvature of the circular segment). Further, in the case of a no slip boundary condition, the total

viscous force per unit length of the contact line during dewetting is given by (Al Akhrass et al., 2008; de Gennes, Brochard-Wyart, & Quéré, 2004).

$$F_{\text{visc}} = 3\eta v \cdot \theta_{\text{dyn}}^{-1} \cdot \ln(h_{\text{max}}/h_{\text{min}}) \quad (2.20)$$

with h_{min} and h_{max} being the minimum and maximum thicknesses of the rim with respect to the contact line, respectively. At the moving contact line (dewetting front) we have a balance of the driving Young's force and the viscous force F_{visc} such that $F_{\text{Young}} = F_{\text{visc}}$ (Peshcka et al., 2019):

$$(1/2) \cdot \gamma_L \cdot (\theta_{\text{equ}}^2 - \theta_{\text{dyn}}^2) = 3\eta v \cdot \theta_{\text{dyn}}^{-1} \cdot \ln(h_{\text{max}}/h_{\text{min}}) \quad (2.21)$$

If dissipation is due to viscous flow generated in the core of the dewetting rim, then the total dissipated energy per unit time and unit length of the contact line (D_{diss}) during dewetting is given by (Brochard-Wyart, & de Gennes, 2003; Reiter, 1993, 2013);

$$D_{\text{diss}} = 3\eta v^2 \cdot \theta_{\text{dyn}}^{-1} \cdot \ln(h_{\text{max}}/h_{\text{min}}) = F_{\text{visc}} \cdot v \quad (2.22)$$

If we suppose that the Laplace pressure is the same everywhere within the rim, we obtain for large rims $\theta_{\text{dyn}} \cong \phi$. In addition, for $R \gg w$, both boundaries of the rim (indicated by the positions A and B in Fig. 2.3(b)) advance at approximately the same dewetting velocity v .

Using $L_A = \ln(h_{\text{max}}/h_{\text{min}})$ at point A of Fig. 2.3(b) then we obtain for the force balance at position A (with a dewetting velocity v):

$$\gamma_L \cdot (\theta_{\text{equ}}^2 - \theta_{\text{dyn}}^2) \cdot \theta_{\text{dyn}} = -L_A \cdot \eta \cdot v \quad (2.23)$$

Further, the equilibrium value of the contact angle at point B is zero since the rim is in contact with the film of the same liquid and hence with $L_B = \ln(h_{\max}/h_{\min})$ at point B (de Gennes, & Deutsch, 1991)

$$\gamma_L \cdot \phi^3 = -L_B \cdot \eta \cdot v \quad (2.24)$$

The minimum length-scale h_{\min} for position A is proportional to the size of the molecules and for position B proportional to the thickness of the film. The maximum length-scale h_{\max} is always related to the maximum height of the rim. For very thin films (nanometer range), L_A and L_B are similar. As a result, a relationship between dynamic and equilibrium contact angles exist for the case of viscous dewetting such that (Brochard-Wyart et al., 1994, 1997):

$$\gamma_L \cdot (\theta_{\text{equ}}^2 - \theta_{\text{dyn}}^2) \cdot \theta_{\text{dyn}} = \gamma_L \cdot \phi^3 \quad (2.25)$$

and with $\phi \cong \theta_{\text{dyn}}$, we obtain;

$$\theta_{\text{dyn}} = \theta_{\text{equ}}/\sqrt{2} \quad (2.26)$$

After nucleation of a hole at time $t = 0$, i.e., the formation of a circular contact line, the growth of the hole proceeds at a velocity $v \sim dR(t)/dt$, with the retracted liquid collected in the surrounding rim. According to Redon et al. (1991) for non-slipping fluids, the holes open at a constant velocity of:

$$v \sim v^* \cdot \theta_{\text{equ}}^3 \quad (2.27)$$

with $v^* = \gamma_L/\eta$.

For $R \gg w$, a constant dewetting velocity (eqn. (2.27)) is observed as long as the assumption of a non-slip boundary condition applies. However, for the slip case, the velocity is given by (de Gennes, Brochard-Wyart, & Quéré, 2004):

$$v_s = |S|.b/3\eta.w \quad (2.28)$$

where v_s is the slip velocity, $b = \eta/\xi$ is the slip length, ξ is the coefficient of interfacial friction between the substrate and the fluid and is related to the linear interfacial force $f = \xi v_s$, $w = \phi_s \sqrt{hR}$ is the rim width (by volume conservation and self-similarity), ϕ_s is a constant, h is film thickness and R is the radius of the hole. The characteristic growth law for the radius of a dewetting hole with time for the no slip and slip cases are: $R \propto t$ (no-slip) and $R \propto t^{2/3}$ (slip) (Brochard-Wyart et al. 1997; Chandran, & Reiter, 2016; Reiter, Castelein, & Sommer, 2003; Sawamura et al., 1998).

Recent experiments and simulations of liquid flow at the microscopic scale have revealed conditions for slip (non-zero velocity) at the interface between a solid wall and a flowing liquid (Brochard-Wyart et al., 1994; Damman et al., 2007; Hamieh et al., 2007). In the case of slippage, as it occurs for polymer melts on “ideal” substrates (Reiter, 2013; Reiter et al., 2005), energy is dissipated over the whole moving interface which is proportional to the width of the rim. Thus, for slippery interfaces, the viscous force depends on the slip length, b , which is defined as the distance below the plane of the substrate, at which the dewetting velocity linearly extrapolates to zero (Fig. 2.4).

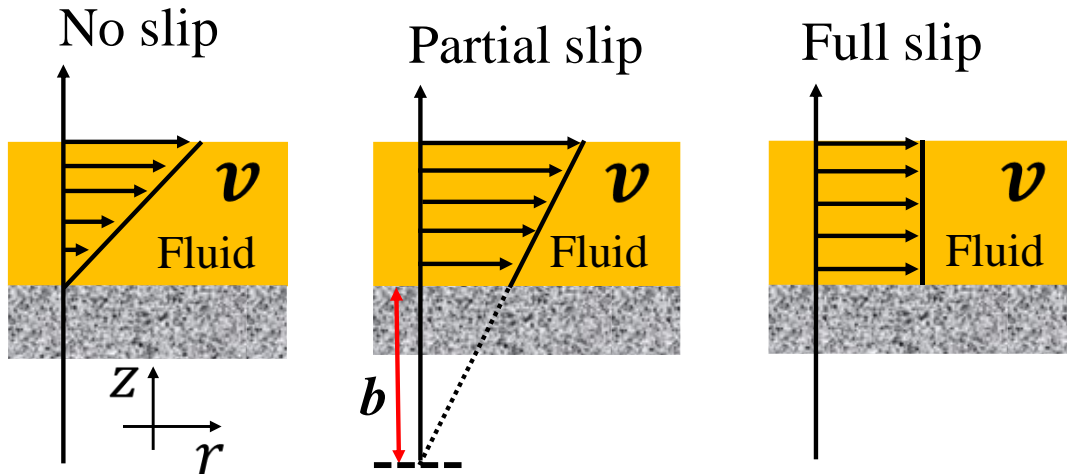


Fig. 2.4: Boundary conditions for a fluid moving over a surface showing no slip (Poiseuille flow), partial slip (slip length, $b = \eta/\xi$, η is the viscosity of the fluid, ξ is the coefficient of interfacial friction between the substrate and the fluid) and full slip (plug flow) (slip length, $b = \infty$) conditions (Brochard-Wyart et al., 1994).

Accordingly, as the size of the rim increases in time, dissipation increases also. Therefore, for a constant capillary driving force, the dewetting velocity is decreasing in time. When there is no interfacial frictional dissipation, a film will rupture without formation of a rim i.e. the material will be distributed throughout the liquid film resulting in enhancement of the mean film thickness (Brochard-Wyart et al., 1997). In case of polymers (entangled chains), their energy of cohesion is higher than the energy of adhesion and therefore, polymers when they move over an unfavorable surface, experience slippage (boundary condition) (Brochard et al., 1994, 1997; Reiter, 2005). Boundary conditions play an important role in characterizing fluid flow profile. Presence of slip is a revelation of the complex interaction of molecules and atoms at small length scales. Several factors that affect the slip characteristics include the strength of the interatomic bonds between a solid and the fluid, the surface roughness and the flow rate. The slip length, $b = \eta/\xi$ is the distance inside the substrate at which the velocity extrapolates to zero for slipping films (Bäumchen, & Jacobs, 2010; Bäumchen et al., 2012; Blossey et al., 2006).

For the slipping films, the frictional dissipation (F_{diss}) at the interface between polymer melt and substrate is proportional to the velocity (slip velocity) such that:

$$F_{\text{diss}} = \xi \cdot v_{\text{slip}} \quad (2.29)$$

According to de Gennes, $\xi = \eta/b$ (η is the viscosity) (de Gennes, Brochard-Wyart, & Quéré, 2004; Vilmin, & Raphaël, 2006; Ziebert, & Raphaël, 2009). Theoretically, $b = a \cdot (N^3/N_e^2)$ (a is monomer size, N is the polymerization index and N_e is the number of segments between entanglements). For $b \gg h_0$ (film thickness), energy dissipation takes place at the polymer-substrate interface where the highest velocity gradient exist. Consequently, velocity scales as $\sim t^{-1/3}$ (de Gennes, Brochard-Wyart, & Quéré, 2004; Reiter, 2013).

2.5 Previous studies: Rheological properties of thin polymer films via dewetting

In the following sub-sections, we discuss some of the previous studies specifically on effect of preparation parameters, dewetting temperature and blending dynamics in thin polymer films.

2.5.1 Effect of preparation parameters and dewetting temperature

Previous studies on dewetting dynamics in thin polymer films have shown how a simple technique like dewetting can be used as a rheological probe to reveal the rich dynamic behaviour of polymers confined in thin films (Reiter, 1993, 1994, 2013). Though segments at the top of a film on a substrate have enhanced mobility, it is not clear how the excess mobility propagates deeper into the film (Al Akhrass et al., 2008; Chowdhury et al., 2012; Reiter, 2013). As a result, preparation conditions such as the spin-coating speed, solvent evaporation rate, evaporation time, solution concentration, molecular weight are important in analyzing the rheological properties in thin polymer films. Even though studies have been done on the effect

of preparation conditions on rheological properties of thin polymer films via dewetting (Chandran et al, 2017; Makhoulf, 2014; Reiter, 2013), the relationship between preparation conditions and viscoelastic properties is still unclear. In particular, when film thickness decreases below the diameter of Gaussian polymer coils in bulk samples, the relationship between film thickness and polymer properties (such as viscosity, interdiffusion rate, mechanical properties and changes in glass transition temperature (T_g)) is complex.

Chandran et al. (2017) in their work on preparation-induced non-equilibrium behaviour of polymer films observed that the preparation pathway (appropriate preparation time normalized by the characteristic relaxation time of the polymer) contributes to non-equilibrium nature of polymer films. In particular, they revealed scaling relations between preparation pathway and the amount of preparation-induced residual stresses, the corresponding relaxation time and probability of film rupture in which films of different thicknesses (obtained by varying solution concentration and spin-coating speed) exhibited different hole nucleation densities and subsequent dewetting kinetics. This is an indication that it is possible to tune the properties of polymer films by preparing films in a specific way (Chandran et al., 2015, 2019, Chandran, & Reiter, 2016, 2019). Even though the scaled relations give a clear description of dewetting dynamics in thin polystyrene films, its application in dewetting behaviour in crystallizable polymer materials is not yet available.

According to Damman et al. (2007), existence of residual stress in thin polystyrene (PS) films is due to chain conformations and reduced entanglement density resulting from preparation conditions as confirmed by Reiter (2013). The authors observed a large increase of strain (ε) with chain length which they attributed to large residual stresses (σ) or smaller elastic modulus (E) (since $\varepsilon = \sigma/E$) in line with what was obtained by Vilmin, & Raphaël (2006). However, they ruled out effects of chain confinements since the observed high strains was uniform for

all the films considered. Interestingly, the strain was observed to saturate for high molecular weights ($M_w > 300$ kg/mol) which was alluded to changes in elastic modulus and residual stress. It is clear from the foregoing that evolution of strain with molecular weight in equilibrated PS films is a complex undertaking.

Besides being able to characterize the rheological properties of thin polymer films, dewetting experiments are sensitive tools for determination of relaxation processes, contact angle and frictional properties of polymer-substrate interface as a function of temperature and molecular weight (Chandran, & Reiter, 2016; Chandran et al., 2017). High molecular weight polymer films at temperatures close to T_g exhibit an asymmetric shape of the rim for long times due to elastic deformation resulting from interfacial friction (Sharma, 2001; Sharma, & Reiter, 1996). In dewetting thin polystyrene films at temperatures slightly above glass transition temperature, it is found that for long chain polymers, relaxation rates of residual stresses are faster than the longest bulk relaxation processes but independent of molecular weight and dewetting temperature (Chandran et al., 2017; Chowdhury et al., 2012; Reiter, 2013).

2.5.2 Blending dynamics in polymer materials

Blending in polymer materials refers to the physical mixtures of two or more polymers with no covalent bond connecting the individual component polymers (Utracki, 2003; Utracki, Leszek, & Wilkie, 2014). Polymer blends exhibit superior properties to those of component homopolymers and offer opportunities for reuse and recycling of polymer wastes. When two or more polymers are mixed, the phase structure of the resulting material can be either miscible (homogeneous) or immiscible (heterogeneous) (Plans, MacKnight, & Karasz, 1984; Utracki, 2003). Due to their high molar mass, the entropy of mixing of polymers is relatively low and consequently establishing a thermodynamically stable film of a blend of two polymers is often

a challenge (Flory, 1942). Immiscible systems exhibit polymer segregation due to incompatibility between the individual homopolymers (Nies, & Stroeks, 1990; Yamaguchi, Suzuki, & Maeda, 2002). There are three different types of blends depending on the miscibility: Completely miscible blends exhibiting one glass transition temperature (T_g) such as polystyrene/poly(phenylene oxide) (PS/PPO) blend; partially miscible blends in which a small part of the blend is dissolved into the other part characterized with a fine phase morphology but different T_g like polycarbonate/acrylonitrile butadiene styrene (PC/ABS) blend; fully immiscible blends characterized by coarse morphology, sharp interface and poor adhesion between the blend phases such as poly(methylmethacrylate)/poly(butadiene) (PMMA/PB) blend (Stroeks, & Nies, 1990; Utracki, 2003)

Most of the previous studies on polymer blends were of heterogeneous type (immiscible) with a few homogeneous ones (miscible) (Kojio et al., 2019; Li, & Woo, 2006; Müller-Buschbaum, Gutmann, & Stamm, 2000; Müller-Buschbaum et al., 1998; Runt, 1981; Taguchi, Miyamoto, & Toda, 2019; Tanaka, Imai, & Yamakawa, 1970). As observed by Müller-Buschbaum et al. (1998) the blend between deuterated polystyrene (dPS) and atactic poly(*para*-methylstyrene) (aPpMS) was miscible at high aPpMS content with an observed faster dewetting. High concentration of dPS led to immiscibility characterized by rough surfaces. The authors observed that one component (dPS) had an affinity for the substrate interface and the other (aPpMS) for the air interface, favoring phase separation into two layers. In addition, it was noted that an aPpMS layer dewetted faster than a dPS layer. They also explored if the dewetting process had to compete with phase separation which is a challenge in any high-tech applications requiring a stable, homogeneous and uniform films. At the same time, investigation of miscibility behaviour in aPS and aPpMS blend by Stroeks, Paquaij, & Nies (1991) observed that the blend was free from interactions with moderate polydispersity effects.

The authors did not detect any phase separation and their explanation was based on the fact that aPS and aPpMS are similar in physical and chemical characteristics, the only difference being the end group (methyl) in aPpMS. Based on the minimization conditions of Holes-Huggins (HH) theory (Nies, & Stroeks, 1990), experimentally, there was no observation of lower critical solution temperature (LCST) in the aPS/aPpMS blend, though, it can occur when free-volume difference of the pure components exceed a certain value. Shu, & Woo (2006) found the blend between aPS and syndiotactic PS (sPS) to be miscible through examination of the interaction parameter from measurement of the equilibrium melting point from thermodynamic point of view. In addition, Chang, & Woo (2003a, 2003b) in their examination of miscibility behaviour between isotactic PS, aPpMS and aPS showed that the binary system iPS/aPpMS was miscible with the rare upper critical solution temperature (UCST).

According to Callaghan, & Paul (1993), properties of blend films are dependent on the thermodynamic interaction between the component polymers. The authors observed that at low molecular weight of the constituent polymers, the blend between aPS and atactic poly(*alpha*-methylstyrene) (aP α MS) was miscible with an interaction energy density between 0.011 – 0.050 cal/cm³ according to Flory-Huggins theory (Nies, & Stroeks, 1990). The blends exhibited a UCST. However, the blend of aPS and atactic poly(methyl methacrylate) (aPMMA) was observed to exhibit high interaction energy. For the ternary system of aPS/aP α MS/aPpMS, Chang, Woo, & Liu (2004), noted that the 10/80/10 and 5/90/5 compositions were miscible. However, it was puzzling to note that the same ternary system showed ultra-small domains in the homogeneous blend which may have exhibited a phase-in-phase morphology. In other words, the thermodynamic nature of the system involved a miscibility/immiscibility loop and a UCST behaviour. Though the authors did not pursue the studies further, it would have been interesting to find out how the additional polymer, miscibility and the observed loop affect the

activation energy and rheological properties of any of the aPS/aP α MS and aPS/aP p MS binary systems. This is because, the addition of the third polymer to any of the binary system would have led to a decrease in interfacial tension between the two phases and this, to some extent, improves their penetration according to Macosko et al. (1996).

Except for the blend between dPS and aP p MS that investigated dewetting dynamics on the rheological properties of the blend, the rest of the blends put more emphasis on miscibility and glass transition temperature among the blends (Malhotra et al., 1980; Manfredi et al., 1995; Mitov, & Kumacheva, 1998; Müller-Buschbaum, Gutmann, & Stamm, 2000). At the moment, understanding of rheological properties of non-equilibrated crystallizable polymers in thin films is far from complete. Furthermore, it is not clear what kind of role tacticity plays in miscibility of polymers and how tacticity affects the resulting rheological properties (Huang et al., 2011; Negash, Tatek, & Tsige, 2018). In a previous dewetting study (Chandran, & Reiter, 2016), it has been shown that tacticity may have a strong impact on polymer properties in spin coated thin polymer films, in particular with respect to the magnitude of the generated residual stresses and their corresponding relaxation time. When subjected to large forces and deformations, in particular, crystallizable polymers like isotactic polystyrene (iPS) develop a multi-level hierarchical structure involving multistage relaxation processes (Chandran et al, 2015; Chandran, & Reiter, 2016; Reiter et al., 2009) which strongly depend on deformation and flow history (Poudel et al., 2018b). Unfortunately, the properties of blends of iPS and isotactic P p MS (iP p MS) have not been investigated yet, neither in thin films nor in the bulk.

Thus, it is indispensable to probe how the resulting (rheological) properties of an as-prepared film of a polymer blend change as a function of annealing time. Here, we examined the mechanical properties of spin coated thin films of a blend of two isotactic polymers, iPS and iP p MS, which have been investigated individually by previous dewetting experiments. The

miscibility, crystallization, thermal and structural dynamics of iPS and blends of iPS with other polymers have widely been investigated (Chowdhury et al., 2012; Chandran, & Reiter, 2016, 2019; Kanaya, 2013; Karasz, Bair & O'Reilly, 1965; Reiter, 1993, 1994, 2005; Sommer, & Reiter, 2005; Sutton et al., 1997; Thomas et al., 2011; Yeh, & Lambert, 1972) but only a few studies have focused on iPpMS. Although iPpMS can crystallize, its melting temperature has not been clearly identified (Gunesin, & Gustafson, 1989; Li et al., 2012; Wu et al., 2019). Previous dewetting experiments on iPpMS films and related works have revealed an activation energy of molecular relaxation processes that is somewhat lower than the ones observed for both atactic and isotactic PS (Okada, 1979; Şenocak, Alkan, & Karadağ, 2016).

It is within this context that the study explored how blending iPS with iPpMS at various ratios affects rheological properties of spin coated thin polymer films. What could be the effect of mixing two isotactic homopolymers on their rheological properties and the resulting activation energies? Can transient cooperative processes as observed for iPS (Chandran, & Reiter, 2016) also be found in iPpMS – iPS blend? To find answers to these questions, we probed the properties of iPpMS – iPS blend films through dewetting experiments and focused on changes in relaxation times of residual stresses, activation energy and rheological properties as a function of time for a systematic variation of dewetting temperatures.

2.6 Nanophotonics in thin polymer films

Industrial applications of advanced nanophotonic structures (e.g. sensors, photovoltaics and nonlinear optics) require substantial improvement in the fabrication and characterization processes (Makhlouf, 2014). Nanophotonic devices have a great potential for optical technologies and are promising replacements for existing microscale devices with precise control over their size and position (Atwater, & Polman, 2010). Usually, nanophotonic systems

consist of resonant nanoparticles enabling effective manipulation of light at the nanoscale (Gentili et al., 2012; Ye, Zuev, & Makarov, 2018). Although, nanophotonics has emerged as a novel tool for light processing, its production using natural materials with conventional approaches (e.g. direct focused ion beam milling, nanoimprint lithographies) is unsuitable for large scale and mass production (Koenderink, Alù, & Polman, 2015; McGraw et al, 2014, 2017; Müller-Buschbaum, 2003). Based on previous studies, dewetting has been used as a feasible process (due to its simplicity) for improving the scalability and productivity of thin polymer films for advanced nanostructures (Atwater, & Polman, 2010). The formation of the surface structures in thin polymer films can be attributed to the Marangoni effect and the film thicknesses (McGraw et al., 2010). As a result, it is possible to modify a surface at the nano, micro and the macro scales to produce unique physical characteristics and chemical functionality (Koenderink, Alù, & Polman, 2015; Müller-Buschbaum, 2003).

Here, we review the dewetting strategies for production of well-aligned arrays of submicron- and nanostructures with great control over their size, shape and arrangement to realise the industrial-level fabrication of various practical advanced photonic systems (Yang et al., 2011). According to Gupta et al. (2019), annealing thin films of varied thicknesses leads to formation of well-dispersed and self-ordered nano-structures. Further, the authors observed that changes in the substrate surface energy, film texture, film thicknesses and intermolecular forces between the substrate and the film can lead to different dewetting patterns. At the same time Ye, Zuev, & Makarov (2018), in their study of dewetting mechanisms and fabrication of advanced nanophotonic systems, emphasized the importance of fundamental understanding of the dewetting mechanisms and kinetics which are critical aspects in guiding optimisation of substrate choice, film thickness and dewetting process conditions. In spite of this, there is

limited information on the connection between different dewetting mechanisms and the advanced nanophotonics.

Although most of the previous studies emphasized that film thickness and viscosity plays an important role in the formation of dewetting structures (Atwater, & Polman, 2010; Koenderink, Alù, & Polman, 2015; Makhlouf, 2014; Ye, Zuev, & Makarov, 2018), the resulting effect on the dewetting patterns did not come out clearly. In addition, it was not clear what role molecular weight of the films involved plays during the formation of final surface morphologies. While most of the authors have suggested template dewetting as an option to production of well-structured patterns, the process leads to complexity in the architectures that can be designed (Mitov, & Kumacheva, 1998). To overcome this challenge, there is need to consider thin films at nanometre scale which could lead to formation of flexible fine structures. Further, though it is important to understand the rheological properties of the materials used to produce the films, this did not come out clearly from the literature.

In summary, the experimental and theoretical dewetting studies of thin polymer films that have been reported to date have successfully led to significant understanding of the effect of preparation-induced residual stresses, deviations in polymer mobility and changes in relaxation processes based mainly on polystyrene (PS) on non-wettable substrates, (Chandran & Reiter, 2016, 2019; Reiter, 1994, 2013). However, this has also led to a number of important issues and questions. For instance, the role of capillary forces in dewetting of purely Newtonian liquid films is well-defined, but not for viscoelastic polymer films which are always out-of-equilibrium. The constructive relationship between preparation parameters and dewetting dynamics is inconclusive. Further, there is a clear molecular weight dependence on viscoelastic properties for high molecular weight films (indicative of chain confinement effects) but it is unclear for low molecular weight films. At the same time, it is difficult to describe dewetting

dynamics for the shortest dewetting time in very thin films (< 100 nm) at very high dewetting temperatures ($T_{\text{dew}} \gg T_g$). As a consequence, there is need for further study of dewetting dynamics in thin PS films and related blends to understand both their fundamental and the application characteristics.

In this study, we explored the rheological properties of isotactic poly(*para*-methylstyrene) (i*p*MS) films and its blends via dewetting. The i*p*MS system differs from PS by a nonpolar methyl group introduced at the *para*-position (position 4) of the phenyl ring of styrene monomers (Wu et al., 2019). We lay emphasis on i*p*MS film preparation from a dilute polymer solution to the glassy state by varying solution concentration and spin-coating speed. The preparation-induced residual stresses (arising from out-of-equilibrium chain conformations due to rapid solvent loss), depending on thermal history and ageing time, will lead to changes in viscoelastic dewetting properties of the i*p*MS films deposited on slippery silicon substrates. Further, we investigate the influence of dewetting temperature, relaxation time, residual stresses and temporal changes in the stability of non-equilibrated i*p*MS films on the rheological properties as they progress towards equilibrium state allowing to tune their properties for desired performance in various applications.

CHAPTER THREE

MATERIALS AND EXPERIMENTAL TECHNIQUES

3.1 Introduction

In this chapter, we describe the polymer materials, solvents and substrates used and the experimental techniques we adopted to understand dewetting dynamics in semi-crystalline polymers (isotactic poly(*para*-methylstyrene) and isotactic polystyrene). Thereafter, we describe the preparation of thin polymer films using spin-coating technique for our dewetting experiments. Finally, we discuss how optical microscopy, differential scanning calorimetry, X-ray diffraction spectroscopy, and atomic force microscopy are used to characterize our samples.

3.2 Materials

In this study, we used the isotactic poly(*para*-methylstyrene) (iPpMS) [weight average molecular weight, $M_w = 608$ kg/mol, with polydispersity index, PDI = 2.19, a glass transition temperature, $T_g \approx 110$ °C, and a nominal melting temperature T_m around (220 – 240 °C)] (Wu et al., 2019) and isotactic polystyrene (iPS) [$M_w = 400$ kg/mol, PDI = 2.8, $T_g \approx 95$ °C, $T_m = 220$ °C] (Chandran, & Reiter, 2019). The PDI is used as a measure of the broadness of a molecular weight in a given polymer. All throughout the study we shall use iPpMS608K to stand for iPpMS of $M_w = 608\ 000$ g/mol and iPS400K to stand for iPS of $M_w = 400\ 000$ g/mol.

Our experiments were performed on silicon (Si) wafers which were covered by a native oxide layer with a typical thickness of about 3 nm. Silicon IV oxide (SiO₂) (Sigma-Aldrich, Germany) wafers were preferred substrates due to their very low roughness and controllable

oxide layer thickness. In addition, silanol terminated polydimethylsiloxane (PDMS) ($M_w = 80 \text{ kg/mol}$, $T_g \approx -125 \text{ }^\circ\text{C}$) was used as a brush on the silicon wafer because of its high viscosity, low surface tension, elastic deformation ability, versatility and the polymer films do not adsorb to it (Reiter, 1993, 2013). Toluene was used as a solvent because it is highly reactive and hydrophobic due to the presence of methyl group in its structure.

3.3 Silicon wafer preparation and properties

The silicon wafers used were disk-shaped, oriented $\langle 100 \rangle$ of thickness $520 \pm \mu\text{m}$, p-doped with boron, with a specific resistance of $10 - 20 \Omega \cdot \text{cm}$ and covered with $\sim 3 \text{ nm}$ thick native oxide layer (Sigma-Aldrich, Germany). To favor a defect free monolayers, and to remove major contaminations, the silicon wafers were sonicated in succession for 45 minutes into two baths of ethanol and toluene. The samples were quickly dried by blowing the samples with gaseous nitrogen of purity 5.0 at the end of each sonication procedure. This process allowed to remove all superficial dust impinged in the solvent (Marquant, 2013; Schäffer, 2001). The roughness result measured with atomic force microscopy (AFM) technique showed that the silicon wafers were atomically smooth.

In order to generate hydroxyl-groups on the surface, the silicon wafers were put for one hour in an ultraviolet-ozone (UV-O₃) cleaner in the presence of distilled water (H₂O). The high-energy UV photons broke hydrocarbon bonds of organic contaminants on the wafer surface. In addition, UV light helped to oxidize the Si-SiO₂ surface, prior to hydroxylation in presence of H₂O, which resulted in formation of dangling Si-OH on the treated surface. Immediately after the UV-O₃ cleaning, the silicon wafers were spin-coated at 2000 revolutions per minute (rpm) for 2 minutes with pure heptane and subsequently heptane solution (10 mg/ml) of silanol terminated polydimethylsiloxane (PDMS). Immediately after spin-coating, the PDMS-coated

wafers were annealed in an oven for 6 hours at 170 °C at a pressure of ca. 50 mbar to increase adsorption of siloxane groups to the silicon surface. This creates an irreversibly adsorbed PDMS layer. After annealing, the wafers were immersed for one hour in a Petri dish half-filled with heptane to remove any loosely attached or non-adsorbed PDMS molecules and later rinsed in heptane via spin-coating. The slippery silicon wafers were subsequently stored in a dry place (covered in aluminum wafer dish) (Chandran, & Reiter, 2016, 2019; Reiter, 2005). Figure 3.1 shows the procedure used in substrate preparation.

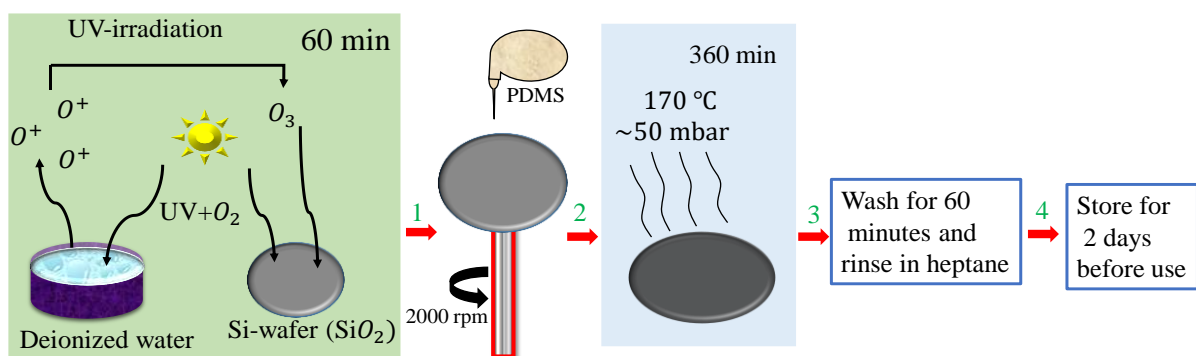


Fig. 3.1: Substrate preparation procedure: (1) spin-coating PDMS solution on silicon wafers, (2) annealing PDMS coated substrates in vacuum, (3) washing the PDMS coated substrates and rinsing in heptane, (4) substrate storage.

3.4 Solution preparation

3.4.1 Concentration variation of isotactic poly(*para*-methylstyrene) (iPpMS)

The dewetting dynamics change when polymer concentration changes. This is because, polymer concentration is related to film thickness. The higher the polymer concentration the thicker the film becomes. The solutions (after several trials) were prepared by changing the polymer concentration (6, 8, 10, 12, 13, 14, 16, 20 and 25 mg/ml) of iPpMS608K in toluene. Solution concentrations below 6 mg/ml led to very thin films (< 70 nm) characterized by faster dewetting and above 25 mg/ml, the films produced were very thick (> 330 nm) characterized by very slow dewetting dynamics. The solutions were then heated to 60 °C with

stirring for 60 minutes to ensure complete dissolution. The solutions were then filtered by a 0.22 μm polytetrafluoroethylene (PTFE) filter due to its hydrophobic properties (Chandran, & Reiter, 2016, 2019; Reiter, 2005).

3.4.2 Isotactic poly(*para*-methylstyrene) (iPpMS) blend solution preparation

Polymer mixtures in most cases are immiscible. As a result, their phase structures are not at equilibrium and depend on the preparation process. There are different methods used to prepare polymer blends such as melt mixing, solution blending, latex mixing, and graft copolymerization (Utracki, 2003). Among the methods, though melt mixing (blend components are mixed in the molten state in extruders or batch mixers) is the most widespread method of polymer blend preparation for large scale applications, its infrastructure is expensive. Latex mixing and graft copolymerization follow a long tedious procedure. On a laboratory scale, solution blending is often used for preparation of polymer blends. Here, the blend components are dissolved in a common solvent and intensively stirred. The blend is then separated by evaporation of the solvent. In this study, solution blending was used because it is cheap, leads to rapid mixing and avoids unfavourable chemical reactions (Wang, Shyong, & Porter, 1995)

Two polymer solutions in toluene with a concentration of 14 mg/ml were prepared. The one of iPpMS608K was prepared at 60 °C for 60 minutes and the one of iPS400K was prepared at 170 °C for 120 minutes with stirring. To obtain a polymer blend solution, two solutions at different ratios (100: 0, 95: 5, 90: 10, 85: 15, 80: 20, 75: 25, 50: 50, 0: 100 of iPpMS608K : iPS400K) were mixed at room temperature. To ensure complete homogeneous mixing, we stirred the polymer solution at an interval of 30 minutes overnight. Afterwards, the blend solution was filtered using a 0.22 μm polytetrafluoroethylene (PTFE) filter. The blend solution

did not exhibit any signs of phase separation, indicating that toluene was a common good solvent for the blend (Müller -Buschbaum, Gutmann, & Stamm, 2000).

3.5 Thin film formation by spin-coating technique

Spin-coating technique was used to deposit thin polymer films on cleaned silicon wafer substrates (Reiter, 1993). In this method, it is possible to control the dynamics of film formation through changes in spin speed, concentration of solution, polymer ratio, which are intrinsically linked to the final structure of the film. Further, rapid solvent evaporation in spin-coating introduces deviations in chain conformations, yielding residual stresses useful for the current study compared to other deposition methods. The spin-coater (WS-650MZ-23NPP, SPS-Europe POLOS™) in Fig. 3.2 with a range of spin-coating speed between 100 – 12000 revolutions per minute (rpm) was used.

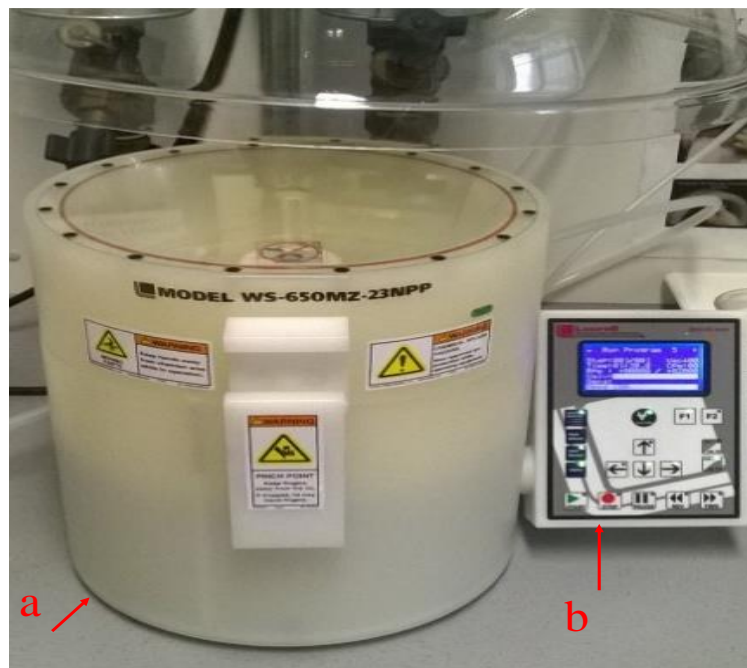


Fig. 3.2: The image of the spin-coater used to prepare all the polymer films under investigation: (a) the body of the spin-coater, (b) the operating system part of the spin-coater.

To start the spin-coating process, the spin-coater vacuum system is first switched on and the working pressure chosen (~15 mbar). On the operating system of the spin-coater, the operation mode is chosen where the spin-coating speed, acceleration and spin-coating time are selected.

The slippery silicon wafers were cut into pieces of about 1.5 cm by 1.0 cm to fit on the chuck in the spin-coater. Next, the substrate was placed on the chuck in the spin-coater and fixed in position by the vacuum underneath. First the substrates were rinsed with toluene by spin-coating at 2000 rpm for about 30 seconds. Next, thin polymer films were prepared in ambient conditions by spin-coating (at a speed of 500 rpm) different concentrations of iPpMS608K solutions (6, 8, 10, 12, 13, 14, 16, 20 and 25 mg/ml) onto slippery silicon substrates for 2 minutes. Instead of changing the polymer concentration, the iPpMS608K concentration was maintained at 14 mg/ml but changed the spin-coating speed (500, 2000, 4000, 6000, 8000 and 12000 rpm). A small change in the spin-coating speed or on the concentration of the solution leads to large changes in the final thickness which leads to different dewetting characteristics. Finally, the blend mixtures were spin-coated (same concentration of 14 mg/ml) at 500 rpm. About 1 – 2 ml of solution was enough to cover the substrate completely before spin-coating.

When a polymer solution is placed on a substrate in a spin-coater, the solution spreads out due to centrifugal force and covers the substrate (varying thickness), increasing from centre to the edge of the substrate. During the spin-off stage (early dewetting phase), some solution flows off the substrate, resulting in a uniform film thickness throughout the substrate. Finally, the solvent evaporates rapidly (late dewetting phase) solidifying the film (Fig. 3.3).

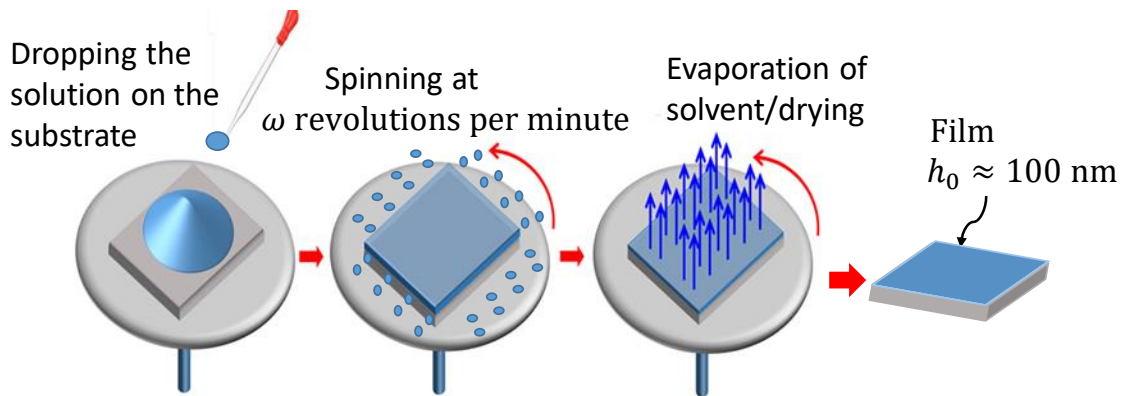


Fig. 3.3: A typical set up for spin-coating process showing how isotactic poly(*para*-methylstyrene) (iPpMS) film of uniform thickness was formed.

The thickness of the prepared films can be obtained from the light interference patterns (with uncertainty of ≈ 10 nm) observed in optical microscope (Fig. 3.4) or measured by atomic force microscopy (AFM).



Fig. 3.4: Interference colors as a function of film thickness for a polystyrene film on a ~ 15 nm thin PDMS layer over silicon wafer which are exactly similar to that of iPpMS films. The film thicknesses changes from left to right (not drawn to scale): 20 nm (light brown), 70 nm (dark brown), 100 nm (dark blue), 140 nm (light blue), 200 nm (yellow), 250 nm (yellow-orange), 260 – 280 nm (purple), 290 nm (blue), 310 nm (turquoise), 330 nm (green), 350 nm (dark yellow), 400 nm (light purple), 420 nm (dark green), 460 nm (yellow), 520 nm (pink), ... alternating light green and pink up to approximately $1.5 \mu\text{m}$ until it changes to a transparent gray (Schäffer, 2001).

3.6 Experimental methods

To characterize the dewetting dynamics in thin isotactic poly(*para*-methylstyrene) (iPpMS) films, optical microscopy (OM), differential scanning calorimetry (DSC), atomic force microscopy (AFM) and X-ray diffractometer (XRD) were employed. In the following subsections, the description of the techniques is given.

3.6.1 Thin film dewetting by optical microscopy (OM)

To capture dewetting dynamics in different films (prepared by varying solution concentration and spin-coating speed), the dewetting temperature varied from 120 °C to 280 °C above the glass transition temperature of the isotactic poly(*para*-methylstyrene) (iPpMS) polymer. Dewetting process was induced by heating the samples on a nitrogen-purged hot stage (Linkam) and the process was monitored through the Zeiss optical microscope (Zeiss Axio-A1). Spin-coated thin films were cut into pieces of about 0.5 cm by 0.3 cm for use with the Zeiss optical microscope. The Zeiss optical microscope is connected to charge-coupled device (CCD) Axio camera so that the images can be taken and the dewetting process monitored closely (AxioView Program) (Fig. 3.5). The colour balance and exposure time of the CCD Axio camera were optimized to produce good quality of real time images during the experiment. Once the substrate stage was heated to the required temperature, the polymer film was placed on the hot stage and the camera was started simultaneously. The whole sample was uniformly heated to a controlled dewetting temperature since a relatively large amount of energy is required to induce dewetting especially for very thick films.

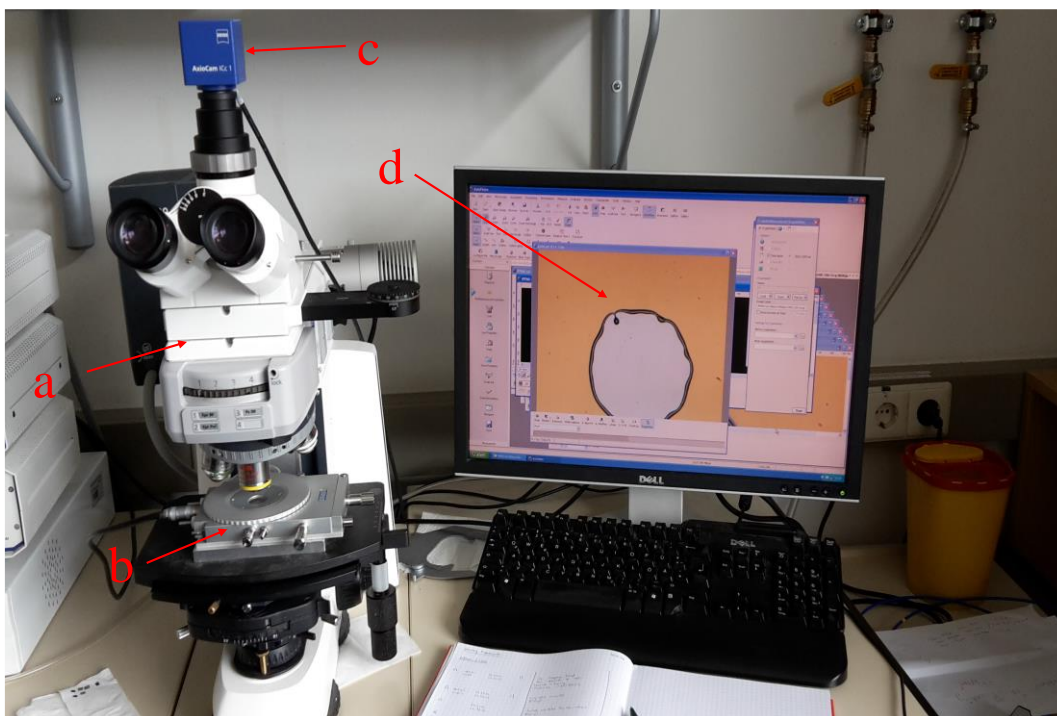


Fig. 3.5: A set up showing dewetting process in a 200 nm isotactic poly(*para*-methylstyrene) (iPpMS) film: (a) Zeiss optical microscope, (b) Linkam (holds the sample under nitrogen flow) connected to a heating system, (c) CCD Axio digital camera connected to Zeiss optical microscope, (d) A window on the desktop showing how images are captured as the dewetting process continues.

3.6.2 Differential scanning calorimeter (DSC) measurements

To find out how a material's heat capacity (or heat of transformation) is changed by change in temperature, a differential scanning calorimeter (DSC) is often used. A given sample (of known mass) is heated or cooled and the changes in its heat capacity are tracked as changes in the heat flow. As a result, detection of transitions such as melts, glass transitions, phase changes, and curing are observed. The choice of DSC system has to do with its advantages of simplicity and speed with which it can be used to see transitions in polymeric materials.

For our studies, the melting and glass transition temperature for the powder samples were studied using a Perkin-Elmer differential scanning calorimeter (Perkin-Elmer DSC600)

operated under a nitrogen atmosphere. The specimens (7.5 mg each) were sealed in aluminium pans and heated from 0.0 to 300.0 °C at a heating rate of 10.0 °C/min.

3.6.3 Atomic force microscopy (AFM) technique

To measure surface properties such as topography and structure in thin polymer films, atomic force microscopy (AFM) is used. It is also used to determine the film thickness obtained through scratches cross the films or in the course of measurement of the height of the rim of a dewetted hole (for dewetted samples). The AFM (AFM, JPK Nanowizard) system used in this study consisted of a silicon cantilever with a sharp tip (with a tip radius of curvature on the order of nanometres) at its end that was used to scan the sample surface. The AFM characterizes the surface of a sample through three main modes: The tip is in direct contact with the surface of the sample (contact mode), the tip is never in direct contact with the surface of the sample (non-contact mode) and the tip oscillates near to its resonance frequency (by a small piezoelectric element mounted in the AFM tip holder) sometimes getting in contact (taps the sample and lifts off) with the surface of the sample (intermittent contact mode). In our study, we set the AFM system in the intermittent contact mode (or tapping mode) since the first two modes have severe drawbacks. For instance, while in contact mode, the surface of the sample is likely to be damaged or the tip fails to effectively measure the surface features in non-contact mode. The tapping mode avoids mechanical deformation of the soft material and minimizes the inelastic deformation of the sample resulting in high resolution images (Ye, & Makarov, 2018).

The important parameters of an AFM cantilever are the material, the spring constant and the resonance frequency. For our measurements, AFM cantilevers were made of silicon provided from Nano-sensors. The silicon resistivity was about 0.01 – 0.02 Wcm. The properties of the

cantilevers used were given by thickness (7 ± 1 mm), length (225 ± 10 mm), width (38 ± 7.5 mm), height ($10 - 15$ mm), resonance frequency ($146 - 236$ kHz) and force constant ($21 - 98$ N/m). The cantilevers and tips were not coated. We used contact intermittent mode imaging (driving frequency: 153.93 kHz, phase shift -380 , amplitude: 0.28 V, set point: 570 mV, P gain: 0.003, I gain: 50 Hz, Z range: 15 μm). The AFM image scans were saved in a JPK file format (*.jpk) and it was possible to post process the images to create common graphic files like JPEG (*.jpg). Further analysis of the images like creation of different cross-sections and 3-dimensional (3D) views was done using a JPK data processing software. In Fig. 3.6, we show (as an example) how the AFM technique is used to measure film thickness ($h_0 \approx 200$ nm), maximum height of the rim ($H_{\text{max}}(t)$) and contact angle (θ) in iPpMS608K (solution concentration: 14 mg/ml, spin-coating speed: 500 rpm).

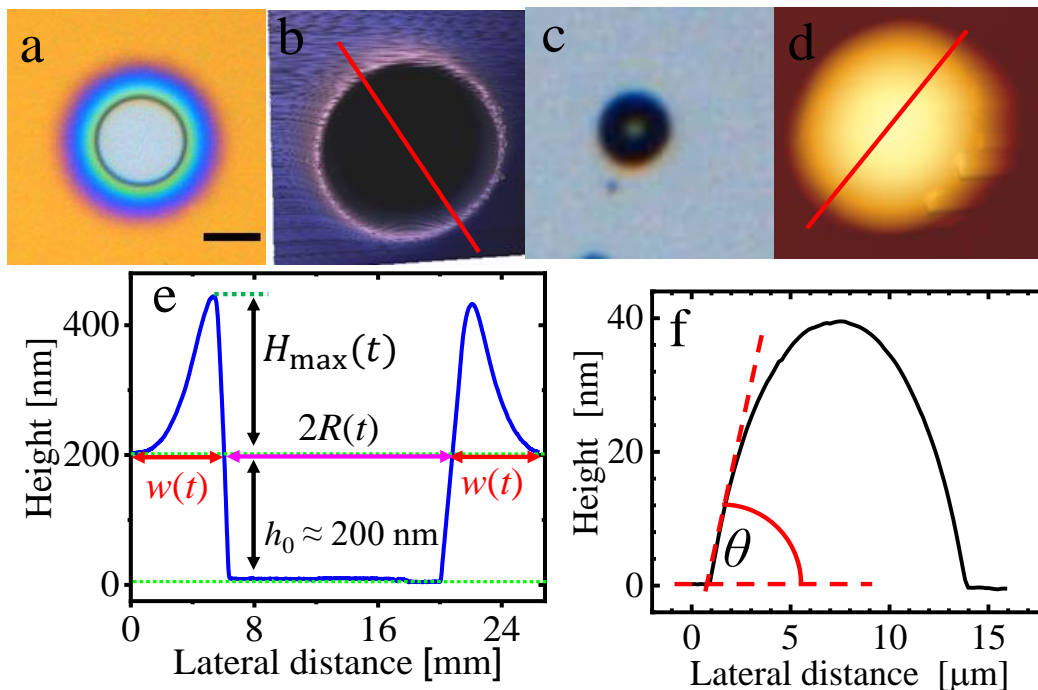


Fig. 3.6: (a) Early stage dewetted hole and (c) final stage of dewetting showing a droplet and their corresponding AFM 3D images (b) and (d), respectively. (e) is an illustration showing how the film thickness ($h_0 \approx 200$ nm) is measured from image (b) (along the indicated red straight line) by AFM technique. Similarly, (f) shows how the contact angle (θ) is measured from image (d) (along the indicated red straight line) by AFM technique in iPpMS608K (solution concentration: 14 mg/ml, spin-coating speed: 500 rpm). The size of images (a)-(d) is $50 \times 50 \mu\text{m}^2$.

The film thickness (h_0) (measured from the base of the exposed substrate) in iPpMS608K (solution concentration: 14 mg/ml, spin-coating speed: 500 rpm) was measured by an AFM technique as shown in Fig. 3.6. To obtain the maximum height ($H_{max}(t)$) of the rim, we measured the height ($H(t)$) and subtracted the film thickness (h_0) as shown in equation (3.1).

$$H_{max}(t) = H(t) - h_0 \quad (3.1)$$

3.6.4 X-ray diffraction (XRD) spectroscopy technique

We used X-ray diffraction (XRD) spectroscopy (Siemens D500, Germany) to identify possible crystal structure of the isotactic poly(*para*-methylstyrene) (iPpMS) samples. The $\theta - 2\theta$ parallel beam geometry of the scan machine was taken from a film prepared on a silicon wafer in reflection mode. The range was from 5° to 70° with detector type of continuous scan at a scan step of 0.5 s and step size of 0.025° . Irradiated length was 12 mm and the specimen length was 10 mm with a receiving slit size of 0.1 mm. The anode material was Copper (Cu) and the incident radiation source was CuK_{α_1} ($\lambda = 1.542 \text{ \AA}$). The intensity of the radiation was provided by the wavelength $\lambda = 1.542 \text{ \AA}$. The generator settings were 30 mA and 40 kV. The XRD measurements were done at room temperature of 25°C .

3.7 Measurement of hole radius, rim width and corresponding velocity

In order to correctly measure the dewetted hole radius ($R(t)$), the resulting rim width ($w(t)$) and the corresponding dewetting velocity ($v(t)$) in the dewetting process of iPpMS films, we first define the time scales that characterize the dewetting process. (i) The time for which the sample was kept on the hot stage, measured from the placement of the film on the hot stage, is called the annealing time (t_{ann}). (ii) The time, which passes from the placement of the film on the hot stage until a given dewetting hole was nucleated, is called the incubation time (t_{inc}).

(iii) The duration of dewetting, measured from the moment a given hole was nucleated, is referred to as dewetting time (t_{dew}). Equation (3.2) shows how t_{dew} is derived from t_{ann} and t_{inc} (Chandran, & Reiter, 2016, 2019; Reiter, 2013)

$$t_{\text{dew}} = t_{\text{ann}} - t_{\text{inc}} \quad (3.2)$$

The collected images from optical microscope were later analyzed manually with the help of analysis software ImageJ. It is possible to convert the pixels of an image taken from optical microscope into the actual size of the sample by using the resolution of the scope used to capture images during *in-situ* dewetting experiment (see the supporting information in the appendix C). The radius and rim width of dewetted holes nucleated at different incubation times were measured directly using ImageJ program (Schneider, Rasband & Eliceiri, 2012) and the graphical analysis done by Origin program (version 2018). Figure 3.7 shows how the hole radius and rim width were measured using ImageJ program.

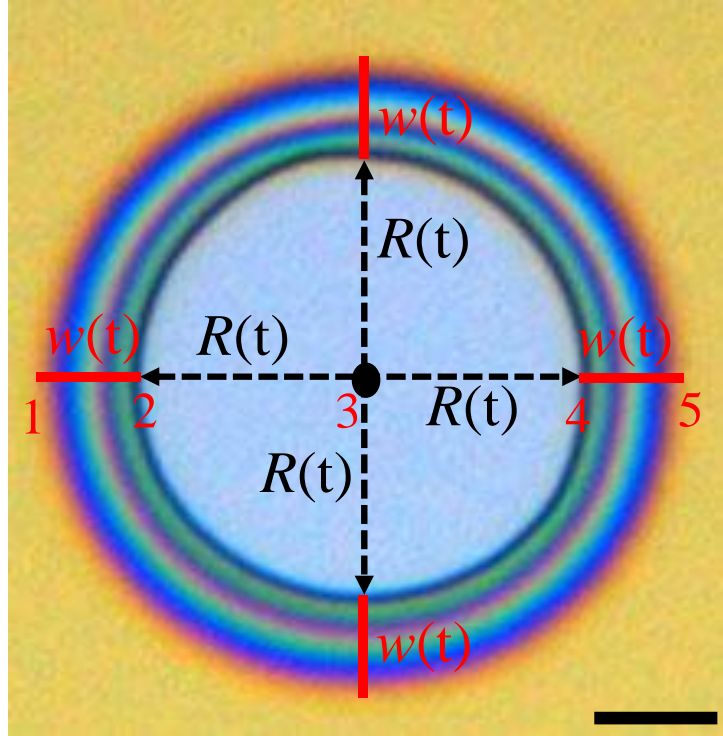


Fig. 3.7: A $100 \times 100 \mu\text{m}^2$ dewetted hole in a 200 nm isotactic poly(*para*-methylstyrene) (iPpMS) film showing how the hole radius ($R(t)$) and rim width ($w(t)$) are measured in ImageJ. The dewetting temperature, $T_{\text{dew}} = 170 \text{ }^\circ\text{C}$, the incubation time, $t_{\text{inc}} = 60 \text{ s}$, and the dewetting time, $t_{\text{dew}} = 1400 \text{ s}$. The numbers 1 to 5 is a guide to the eye on how the measurements were done. The width of the rim is represented by 1 to 2 (left side) and 4 to 5, whereas the radius of the hole is represented by 2 to 3 on the left side and 3 to 4 on the right side.

The dewetting velocity $v_{\text{dew}}(t_i)$ was determined by taking differences of the radius $R(t_i)$ of a dewetting hole at dewetting times t_{i-1} and t_i according to eqn. (3.3) (Chandran, & Reiter, 2016, 2019; Reiter, 1994, 2013),

$$v_{\text{dew}}(t_i) = \frac{[R(t_i) - R(t_{i-1})]}{(t_i - t_{i-1})} \quad (3.3)$$

The rheological properties of iPpMS films are $H_{\text{max}}(t)$ -, h_0 -, $R(t)$ -, $w(t)$ - and $v_{\text{dew}}(t_i)$ - dependent and were obtained from their relationships as discussed in chapter four.

CHAPTER FOUR

RESULTS AND DISCUSSION

4.1 Introduction

The rapid evaporation of solvent in spin-coating technique results in films adopting non-equilibrium conformations. This induces residual stresses within the films (Chandran, & Reiter, 2016, 2019; Reiter, 2013). Dewetting of thin polymer films under controlled environment can provide a route to cost effective, continuous and large-scale production of functionalised materials and control of the relaxation dynamics of out-of-equilibrium isotactic poly(*para*-methylstyrene) (iPpMS) films sheared at rates higher than the reciprocal value of the intrinsic relaxation time of the molecules (Chandran, & Reiter, 2016). The process of dewetting a thin polymer film is complex as it is dependent on many interrelated variables. In the following sub-sections, we discuss the results obtained from a range of systematic dewetting experiments in thin iPpMS films with respect to variations in spin-coating speed, solution concentration (film thickness), dewetting temperature and blending dynamics. These variations in multiple preparation parameters promise a comprehensive preparation-induced residual stress analysis.

4.2 Rheological properties of isotactic poly(*para*-methylstyrene) (iPpMS) films

We first discuss the results obtained from atomic force microscopy (AFM) (film thicknesses), differential scanning calorimetry (DSC) (glass transition temperature and melting temperature) and X-ray diffraction (XRD) (to check presence of crystal structures) in thin isotactic poly(*para*-methylstyrene) (iPpMS) films. In Fig. 4.1, we plotted the results of heat flow as a function of temperature, intensity of X-ray diffraction (XRD) as a function of 2θ , and film thickness as a function of solution concentration and spin-coating speed in iPpMS films. On

heating the sample, a weak step at the glass transition temperature ($T_g = 110\text{ }^\circ\text{C}$) and a weak peak around $230\text{ }^\circ\text{C}$ which we attributed to the melting temperature (T_m) of the *iPpMS* material were observed (Fig. 4.1(a)). The observation is in agreement with what has already been observed by Wu and co-workers (Wu et al., 2019).

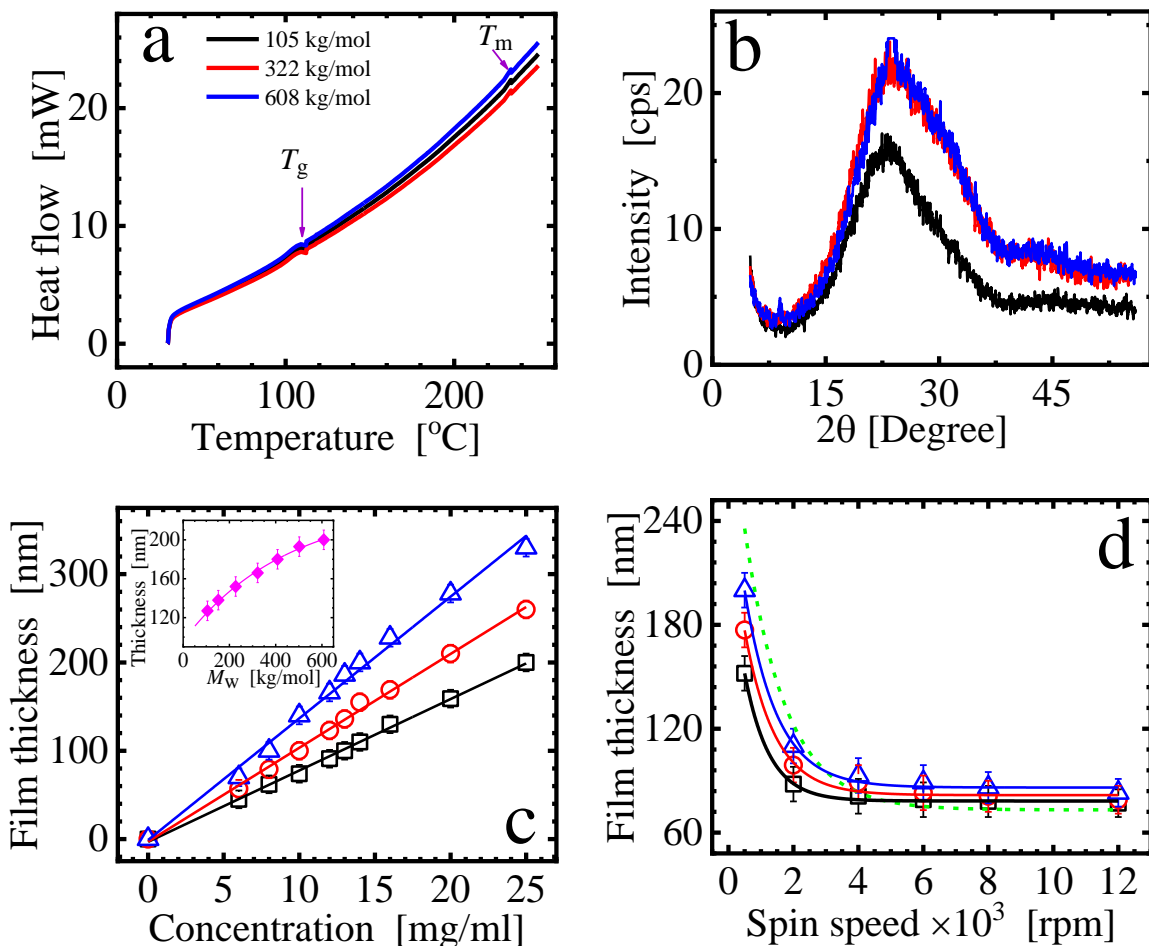


Fig. 4.1: Linear plots of (a) heat flow as a function of temperature, (b) XRD intensity as a function of 2θ , and film thickness as a function of (c) solution concentration, (d) spin-coating speed in *iPpMS*. Different colours indicate different molecular weight as shown in (a). The spin-coating speed was maintained at 500 rpm in (c) and in (d), the solution concentration was maintained at 14 mg/ml. The dashed green line in (d) is the theoretical film thickness-spin-coating speed dependence for polystyrene for comparison (Schubert, 1997).

In addition, we used XRD to obtain the patterns in Fig. 4.1(b) for the *iPpMS* powder sample. Absence of characteristic diffraction peaks implied that the *iPpMS* polymer is dominated mainly by amorphous properties. However, according to already published work, the emerging

weak peak indicates a certain degree of one-dimensional order due to polymer chain-chain distance or distance between phenyl groups (Wu et al., 2019). As shown in Fig. 4.1(c), varying the solution concentration of iPpMS (at constant spin-coating speed) led to production of films of different thicknesses, increasing with increase in solution concentration. Higher solution concentration simply means more polymer material to be deposited. Further, film thickness was found to increase with increase in molecular weight of iPpMS. From Fig. 4.1(d), we observed that film thickness is dependent on spin-coating speed such that $h_0 \sim \omega^{-\alpha}$ with $\alpha = 0.59 \pm 0.1$ (Schubert, 1997). The deviation could result from the differences in viscosities and solution evaporation rates in the iPpMS films. At the same time, we observed that at lower spin-coating speed (≤ 2000 rpm), the difference between the resulting film thickness of iPpMS films is huge compared to the differences at higher spin-coating speed (> 2000 rpm) where the film thickness is almost similar. This is due to the fact that at lower spin-coating speed (at the same spin-coating time), the rate of solvent evaporation is low leading to formation of thicker films than at higher spin-coating speed.

Despite several reports on the effect of preparation parameters on the relaxation dynamics of entangled polymers in metastable state (Chandran, & Reiter, 2016, 2019; Reiter, 2013), a clear relation between preparation parameters and the rheological behaviour probed by dewetting technique in isotactic polymers in melt is lacking. Particularly for isotactic poly(*para*-methylstyrene) (iPpMS) films, limited reports are available on its non-equilibrium dynamics especially with respect to preparation-induced changes in its viscoelastic properties. Therefore, we closely discuss dewetting dynamics of iPpMS films describing the controlled relaxation of residual stresses as a function of preparation parameters. In this section, we investigate the influence of varying the spin-coating speed and solution concentration on the rheological properties of iPpMS608K films.

4.2.1 Effect of spin-coating speed and solution concentration

4.2.1.1 Variation of spin-coating speed

Although dewetting thin polymer films is fast at high dewetting/annealing temperature, it is even more rapid when the film is associated with residual stresses introduced during film formation (Reiter, 2013). We set to find out if changes in spin-coating speed result in different relaxation scenarios in *iPpMS608K* films and if the differences are systematic in any way. In Fig. 4.2, we show how varying spin-coating speed leads to different dewetting dynamics.

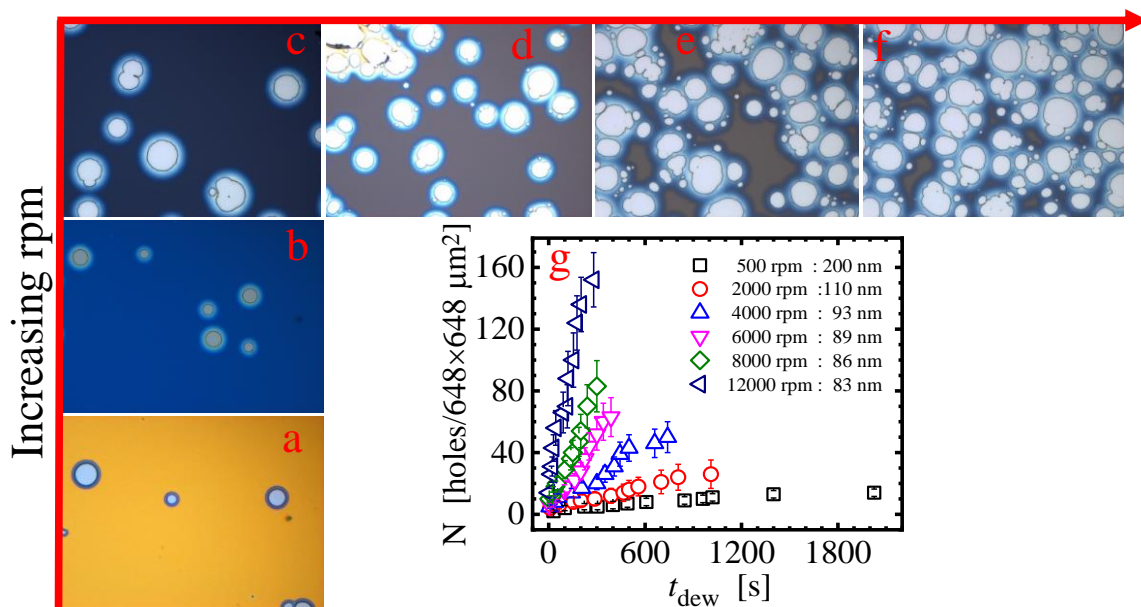


Fig. 4.2: Optical micrographs showing nucleated holes obtained from spin-coating a 14 mg/ml of solution at different spin-coating speeds dewetting at 170 °C: (a) 500 rpm, (b) 2000 rpm, (c) 4000 rpm, (d) 6000 rpm, (e) 8000 rpm and (f) 12000 rpm for the first dewetting holes (at annealing time, $t_{\text{ann}} \approx 100$ s) in *iPpMS608K* films. In (g), the number of nucleated holes are plotted as a function of dewetting time (t_{dew}). Each micrograph measures $648 \times 648 \mu\text{m}^2$. The legend in Fig. 4.2(g) shows the spin-coating speed and the corresponding film thicknesses.

In Figs. 4.2(a) – 4.2(f), hole nucleation density is shown through optical micrographs of *iPpMS608K* films dewetting at a constant temperature, 170 °C. It is clear from the micrographs that increase in spin-coating speed led to different dewetting behaviour in the films due to effect of residual stresses. At low spin-coating speeds (≤ 2000 rpm), the rate of solvent evaporation

and the spin-off of the solution from the substrate are very low leading to high film thicknesses. However, at higher spin-coating speeds (> 2000 rpm), the rate of solvent evaporation and spin-off of the solution from the substrate is very fast resulting in reduced but almost similar film thicknesses (Figs. 4.1(d) and 4.2(g)). From Fig. 4.2(g), the number of holes nucleated per an area of $648 \times 648 \mu\text{m}^2$ increases with increase in spin-coating speed, an indication that the preparation-induced residual stresses are higher in films spin-coated at 12000 rpm than those at 500 rpm.

In Fig. 4.3, we plotted dewetting hole radius ($R(t_{\text{dew}})$), corresponding dewetting velocity ($v(t_{\text{dew}})$) and rim width ($w(t_{\text{dew}})$) as a function of dewetting time (t_{dew}) for the first dewetting holes (at $t_{\text{inc}} \approx 0$ s) in iPpMS608K films at different spin-coating speeds.

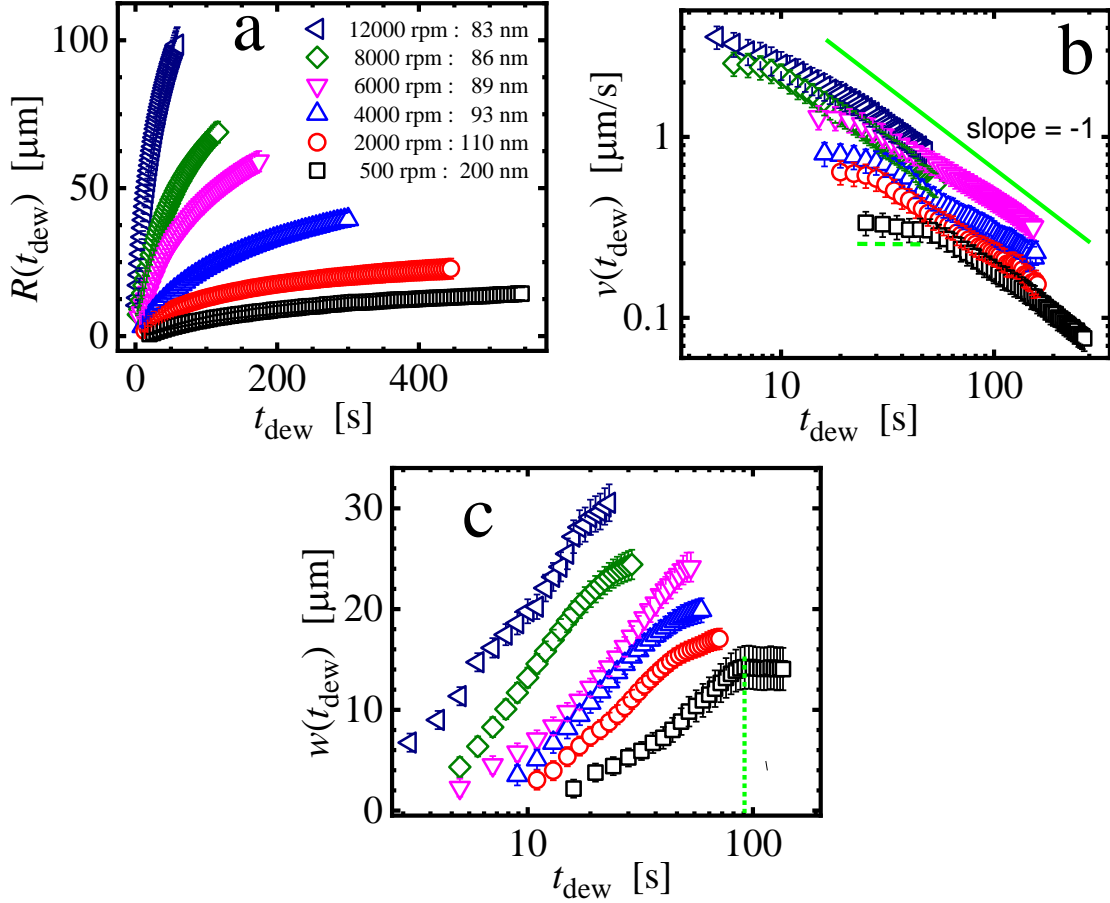


Fig. 4.3: (a) Linear plot of dewetting hole radius ($R(t_{\text{dew}})$), (b) logarithmic plot of dewetting velocity ($v(t_{\text{dew}})$) and (c) semi-logarithmic plot of rim width ($w(t_{\text{dew}})$) as functions of dewetting time (t_{dew}) for the first dewetting holes (at $t_{\text{inc}} \approx 0$ s) in iPpMS608K films at a constant concentration (14 mg/ml) and different spin-coating speeds (legend in (a)) dewetting at 170 °C.

The graphs of hole radius as a function of dewetting time were fitted with the power law relation in order to obtain the incubation time (Chandran, & Reiter, 2016):

$$R(t_{\text{dew}}) = a \cdot (t_{\text{ann}} - t_{\text{inc}})^\alpha \quad (4.1)$$

where $R(t_{\text{dew}})$ is the radius of the hole, t_{ann} is the annealing time, α is the power law exponent, t_{inc} is the incubation time and a is a constant. The radius of the hole increased with $\alpha = 0.68 \pm 0.1$ consistent with theoretical value of 2/3 (Reiter, 1994, 2013; Reiter, Khanna, & Sharma, 2003). However, at higher spin-coating speed, the growth of the hole was very fast. It is clear from Fig. 4.3(a) that the relative increase in radius decreased with decrease in spin-

coating speed, but after about 20 s of dewetting time, the hole radii were overlapping on each other. This observation is an indication that the dewetting driving forces are decreasing with time. Since the residual stresses act as an additional driving force for dewetting, the total dewetting driving force (F_{tot}) can be given by (Chandran, & Reiter, 2016, 2019),

$$F_{\text{tot}} = F_{\text{cap}} + F_{\text{res}} \quad (4.2)$$

where F_{cap} is the capillary force and F_{res} is the residual forces.

Given the spreading parameter $|S| = \gamma_S - \gamma_{LS} - \gamma_L$, where γ_S is surface tension of substrate-vapor, γ_{LS} is surface tension of substrate – liquid and γ_{LV} is surface tension of liquid – vapor, then the capillary force is given by $F_{\text{cap}} = |S|/h_0$ where h_0 is the film thickness. The capillary force depends on surface tension and the contact angle and therefore, at constant temperature, the capillary force will be constant. However, since the residual stress is a time dependent variable, it relaxes with time.

A closer examination of Fig. 4.3(b) reveals that the dewetting velocity could be described by a power law relation $v \sim t^{-\alpha}$ ($\alpha \approx -1$) (Brochard-Wyart et al., 1997; Chandran, & Reiter, 2016, 2019; Reiter, 2013). The decrease in dewetting velocity with dewetting time is an indication that the iPpMS608K films under investigation are relaxing. At low spin-coating speeds (< 4000 rpm), the dewetting velocity was at first constant ($\alpha \sim 0$) as the rim started to form. Later, the dewetting velocity decreased with dewetting time. However, at higher spin-coating speed, due to fast dewetting behaviour, observation of constant dewetting velocity was difficult. Increase in dewetting time led to increase in the rim width in the same way as the observed behaviour for the growth of hole radius with dewetting time (Fig. 4.3(c)). This is because the material retracted from the hole settled around the same hole forming a rim. The rim width was observed to follow a relation of the form $w \sim t^\alpha$ ($2/3 \leq \alpha \leq 1/3$) (Reiter, 1993,

2013) and grew in a logarithmic fashion until a maximum value (w_{\max}) was reached then became constant. This is the point at which the dewetting dynamics change with time in the *iPpMS608K* films. The value on the dewetting time axis at w_{\max} (indicated by the dotted vertical green line of Fig. 4.3(c)) can be related to a transition from a highly asymmetric rims to more symmetric ones. It also points to the fact that the residual stresses (generated during spin-coating) in the *iPpMS608K* films could be relaxing. Sometimes, at higher spin-coating speed (≥ 4000 rpm from Fig. 4.3(c)), observation of maximum rim width was tricky since rim instability started earlier compared to films prepared at lower spin-coating speed (Figs. 4.2(c) - 4.2(f)).

If we consider initial dewetting velocities from each nucleated and grown hole, we can perform an exponential fit to the data obtained as a function of incubation time. This will enable us to discuss the relaxation dynamics of the *iPpMS608K* films. This relaxation process is very important in dewetting dynamics in thin polymer films and has already been reported on dewetting dynamics in atactic polystyrene (aPS) and isotactic PS (iPS) films (Damman et al., 2007; Chandran, & Reiter, 2016, 2019; Reiter, 2013). Consider a plot of initial dewetting velocity ($v_i(t_{\text{inc}})$) as a function of incubation time (t_{inc}) as shown in Fig. 4.4(a) for the first dewetting holes (at $t_{\text{inc}} \approx 0$ s) in *iPpMS608K* films at different spin-coating speeds.

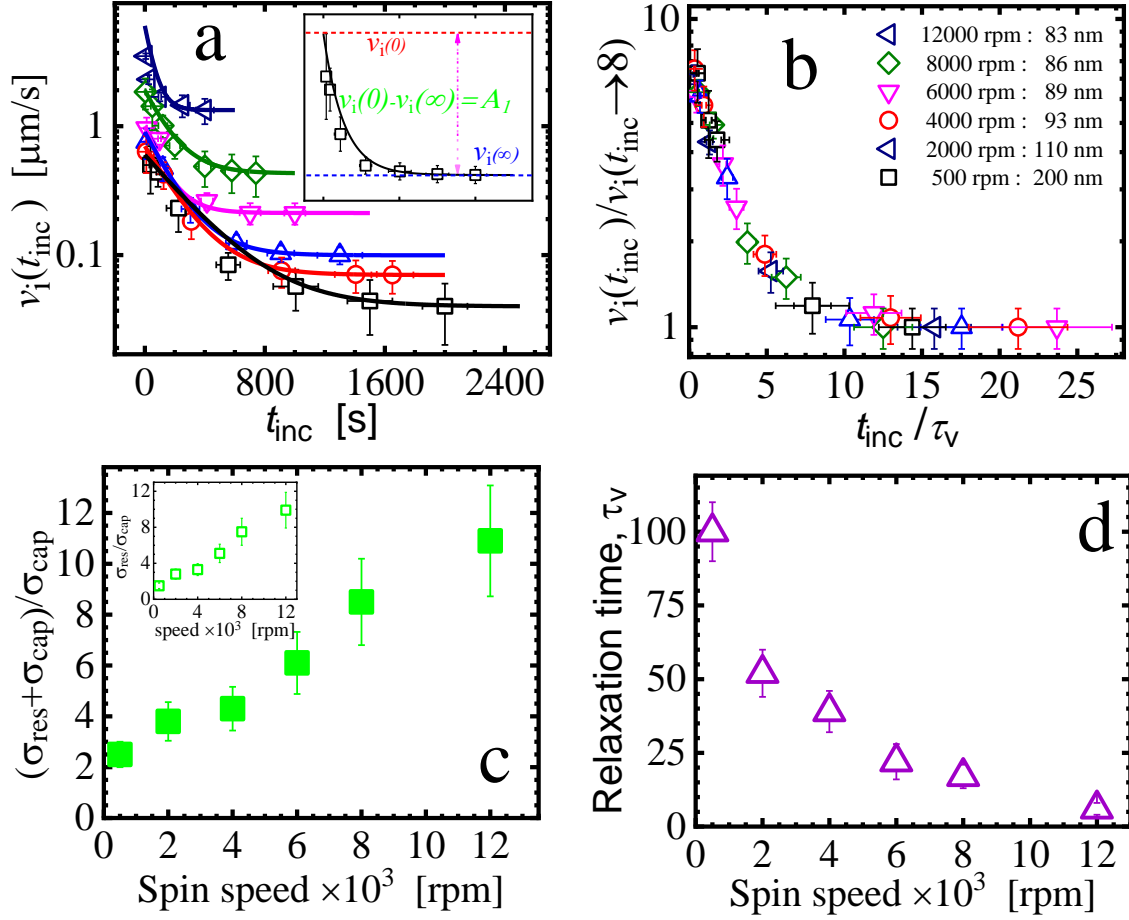


Fig. 4.4: Semi-logarithmic plot of (a) initial dewetting velocity ($v_i(t_{\text{inc}})$) as a function of incubation time (t_{inc}) and (b) normalized dewetting velocity ($v_i(t_{\text{inc}})/v_i(t_{\text{inc}} \rightarrow \infty)$) as a function of reduced time (t_{inc}/τ_v). The symbols represent spin-coating speed and corresponding film thickness as shown in (b). The inset in (a) shows how extreme velocities at $t_{\text{inc}} = 0$ ($v_i(0)$), $t_{\text{inc}} \rightarrow \infty$ ($v_i(\infty)$) and their differences represented by $A_i \in \{A_v, A_w\}$ are extracted from (a). In (c), the ratio of total stress to capillary stress ($(\sigma_{\text{res}} + \sigma_{\text{cap}})/\sigma_{\text{cap}}$) is plotted as a function of spin-coating speed, and in (d) the relaxation time is plotted as a function of spin-coating speed for the first dewetting holes (at $t_{\text{inc}} \approx 0$ s) in iPpMS608K films at a constant concentration (14 mg/ml) and different spin-coating speeds dewetting at 170 °C. The inset in (c) show how the ratio $\sigma_{\text{res}}/\sigma_{\text{cap}}$ changes with spin-coating speed.

The data from the graph of Fig. 4.4(a) was fitted to the following exponential function:

$$v_i(t_{\text{inc}}) = A_v \cdot \exp(-t_{\text{inc}}/\tau_v) + v_i(\infty) \quad (4.3)$$

where $A_v = v_i(0) - v_i(\infty)$, $v_i(0) = v_i(t_{\text{inc}} \rightarrow 0)$, $v_i(\infty) = v_i(t_{\text{inc}} \rightarrow \infty)$, τ_v is the relaxation time with respect to dewetting velocity. How $v_i(0)$, $v_i(\infty)$ and A_i are obtained is

illustrated in Fig. 4.4(a) for the data at a spin-coating speed of 500 rpm. Equation (4.3) can be re-written as:

$$v_i(t_{\text{inc}})/v_i(\infty) = 1 + A \cdot \exp(-t_{\text{inc}}/\tau_v) \quad (4.4a)$$

$$\text{with } A = A_v/v_i(\infty) = \{[v_i(0)/v_i(\infty)] - 1\} = \{B_v - 1\}, B_v = v_i(0)/v_i(\infty) \quad (4.4b)$$

By plotting normalized dewetting velocity ($v_i(t_{\text{inc}})/v_i(\infty)$) as a function of reduced time (t_{inc}/τ_v) (Fig. 4.4(b)) for the first dewetting holes (at $t_{\text{inc}} \approx 0$ s) in *iPpMS608K* films at different spin-coating speeds, we noticed that all the data collapsed into a one master curve. This is an indication that the dewetting behaviour in *iPpMS608K* films is characterized by the same relaxation of residual stress dynamics irrespective of the spin-coating speed at which the films were deposited. The normalized velocity decays (relaxing of residual stresses with time) until it reaches the point where $v_i(t_{\text{inc}})/v_i(\infty) = 1$. This constant point signifies that from now onwards, all the holes that will nucleate in the given film will evolve with similar velocity or growth rate, suggesting that the dewetting driving force is constant (only capillary forces are now responsible for dewetting process) (Müller-Buschbaum, 2003). Further, this is an indication that despite preparing *iPpMS608K* films at different spin-coating speed, after relaxation of internal stresses, they showed similar dewetting velocity. The time at which $v_i(t_{\text{inc}})/v_i(\infty) = 1$ is reached is taken to be the relaxation time (τ_v) of the films.

The extreme velocities (on the inset of Fig. 4.4(a)) are very important in understanding the relaxation dynamics in thin polymer films. For instance, the total driving stresses in *iPpMS608K* films is governed by:

$$v_i(0) / v_i(\infty) = (\sigma_{\text{res}} + \sigma_{\text{cap}}) / \sigma_{\text{cap}} = [\sigma_{\text{res}} / \sigma_{\text{cap}} + 1] = B_v \quad (4.5)$$

where σ_{res} is the residual stress, σ_{cap} is the capillary stress, $v_i(0)$ is the initial dewetting velocity of the growing hole at a constant $t_{\text{inc}} = 0$ and $t_{\text{dew}} = \text{constant}$, $v_i(\infty)$ is a constant dewetting velocity at $t_{\text{inc}} \rightarrow \infty$ and $t_{\text{dew}} = \text{constant}$. By comparing equations (4.4b) and (4.5), we obtained $A = \sigma_{\text{res}} / \sigma_{\text{cap}}$, which represents the relative contribution of residual stresses in the polymer films (Chandran et al., 2017). In Fig. 4.4(c), we observed an increase in the ratio of $(\sigma_{\text{res}} + \sigma_{\text{cap}}) / \sigma_{\text{cap}}$ with increase in spin-coating speed. In particular, an interesting observation from the inset of Fig. 4.4(c) is that the magnitude of obtained $A = \sigma_{\text{res}} / \sigma_{\text{cap}}$ is highest for the films deposited at the highest spin-coating speed than for those prepared at lower spin-coating speed. This is an indication that the presence of residual stress in the iPpMS608K films under investigation is highly dependent on spin-coating speed and increases as the spin-coating speed increases. As a consequence, it is clear from Fig. 4.4(d) that stress relaxation in the films prepared at high spin-coating speed (≥ 4000 rpm) is faster compared to those films prepared at lower spin-coating speed (< 4000 rpm). The relaxation times plotted in Fig. 4.4(d) were obtained from fitting equation (4.3) to the data of Fig. 4.4(a). Accordingly, films spin-coated at lower spin-coating speed allows one to be able to fully understand their dewetting dynamics than at higher spin-coating speed.

4.2.1.2 Influence of solution concentration

If we change the solution concentration of iPpMS608K and prepare thin films (at constant spin-coating speed), will there be any appreciable change in relaxation dynamics in iPpMS films? Will there be any systematic relations between fast relaxing and slowly relaxing perturbations? What information about the activation energy do we obtain? In an attempt to find answers to these questions, we prepared iPpMS608K films of different thicknesses (by changing solution

concentration) and discussed their effect on the viscoelastic properties of *iPpMS608K* films. In Fig. 4.5 we have presented optical micrographs together with a graphical representation showing the number of nucleated holes per an area of $648 \times 648 \mu\text{m}^2$ in *iPpMS608K* films (prepared at different solution concentration but constant spin-coating speed) as a function of dewetting time.

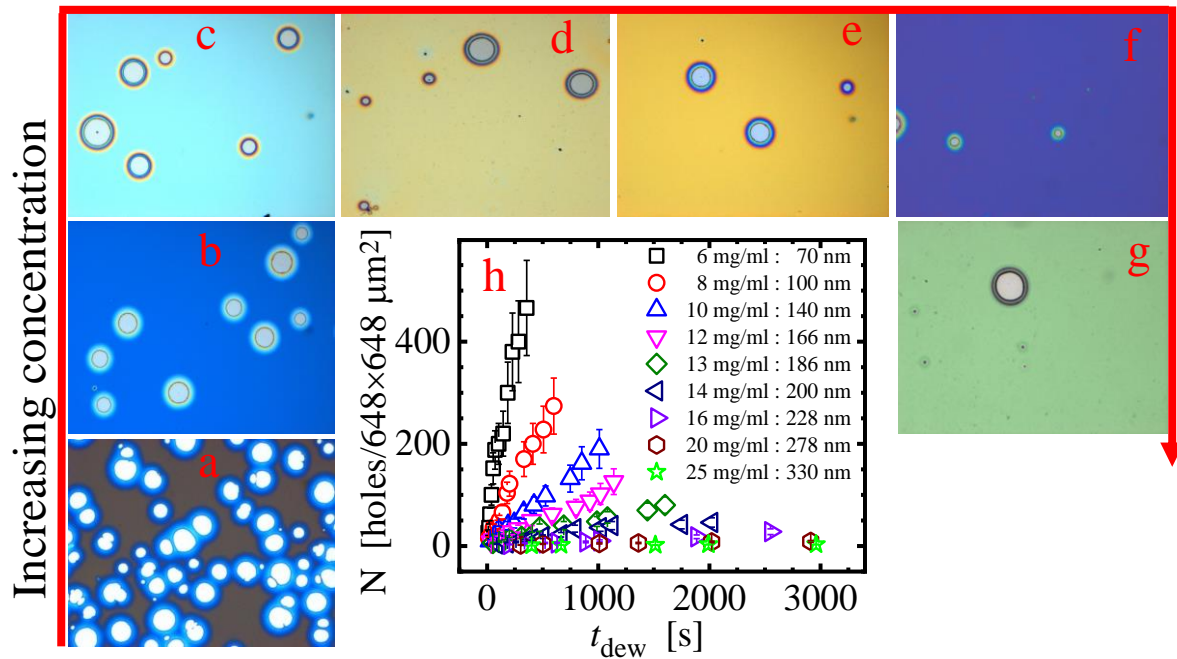


Fig. 4.5: Optical micrographs showing nucleated holes obtained from spin-coating different solution concentrations at 500 rpm dewetting at 170°C : (a) 6 mg/ml, (b) 8 mg/ml, (c) 10 mg/ml, (d) 13 mg/ml, (e) 14 mg/ml, (f) 20 mg/ml, (g) 25 mg/ml for the first dewetting holes (at annealing time, $t_{\text{ann}} \approx 200$ s) in *iPpMS608K* films. In (h), we plotted the number of nucleated holes as a function of dewetting time (t_{dew}). Each micrograph measures $648 \times 648 \mu\text{m}^2$. The legend in (h) shows the solution concentration and the corresponding film thicknesses.

In Figs. 4.5(a) – 4.5(g), we observed differences in the rate of rupture of the *iPpMS608K* films prepared at the same spin-coating speed but different solution concentration and dewetting at the same temperature. The number of holes decreases with increase in solution concentration (film thickness). Here, increase in the *iPpMS608K* solution concentration leads to formation of thick films, otherwise thin films are formed. The number of holes per an area of $648 \times 648 \mu\text{m}^2$ was highest in films prepared from a 6 mg/ml solution (70 nm) and lowest in films

prepared from a 25 mg/ml solution (330 nm) at constant spin-coating speed. This was clearly visible from Fig. 4.5(h) depicting the maximum number of holes at a given time ($t_{\text{ann}} \approx 200$ s) for a particular film thickness. This is a clear indication that the preparation-induced residual stresses are higher in films prepared from low solution concentration than those prepared from higher solution concentration at the same spin-coating speed. To understand the dewetting dynamics with respect to film thickness, we followed an evolution of a hole from the moment it was nucleated until it reached the maturity stage and analyzed its growth dynamics as shown in Fig. 4.6.

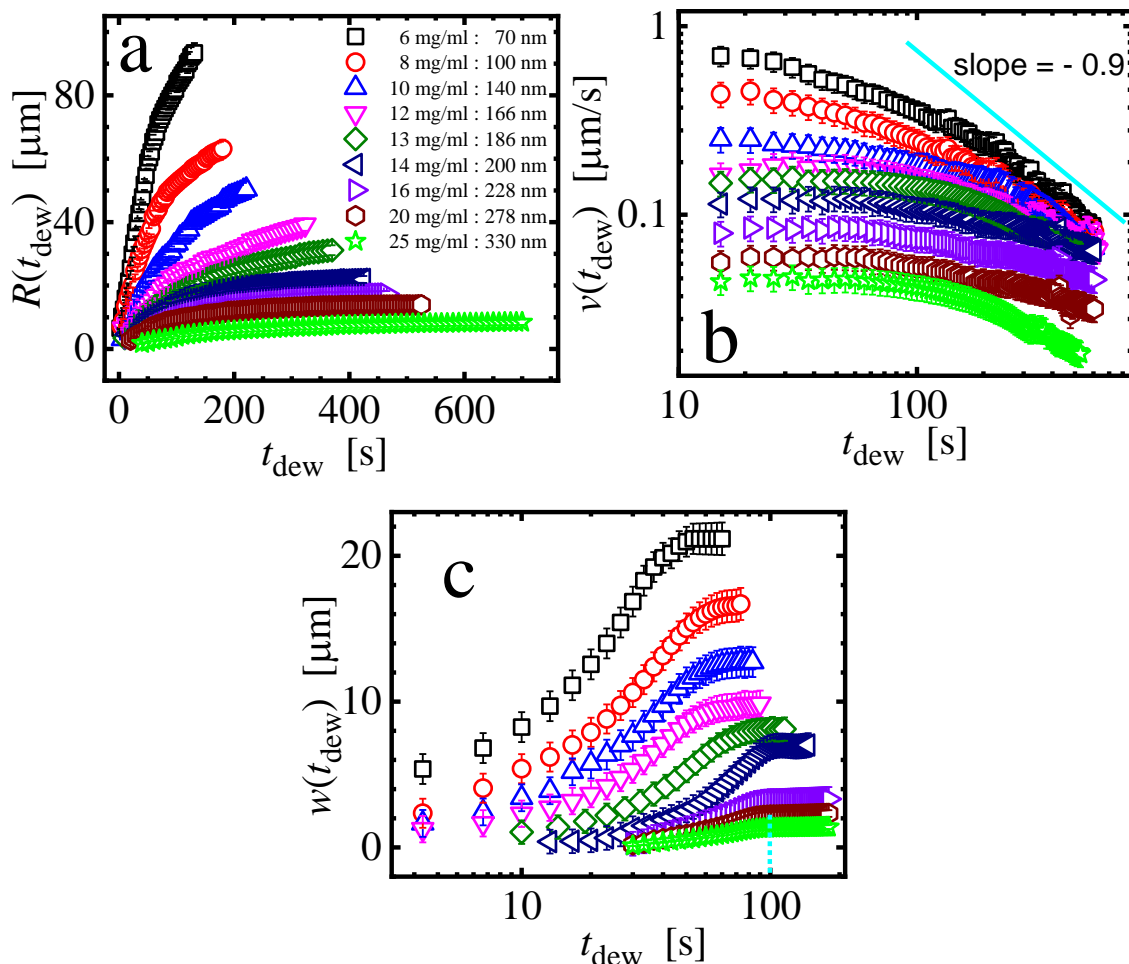


Fig. 4.6: (a) Linear plot of dewetting hole radius ($R(t_{\text{dew}})$), (b) logarithmic plot of dewetting velocity ($v(t_{\text{dew}})$) and (c) semi-logarithmic plot of rim width ($w(t_{\text{dew}})$) as functions of dewetting time (t_{dew}) for the first dewetting holes (at $t_{\text{inc}} \approx 0$ s) in iPpMS608K films prepared from different solution concentrations but at constant spin-coating speed (500 rpm) dewetting at 170 °C. The legend in (a) shows the solution concentration and the corresponding film thicknesses.

The dewetting hole radii (Fig. 4.6(a)) followed the already discussed power law of equation (4.1) with $\alpha = 0.66 \pm 0.1$. It was observed that hole growth decreased with increase in film thickness which is expected because the thicker the film gets the more material is there to push hence slower hole growth. Correspondingly, the dewetting velocity decreased with increase in film thickness (Fig. 4.6(b)). The dewetting velocity was first constant as the rim started to build up (highly asymmetric), an indication that the films were not slipping. During the transition of rim shape from asymmetric to symmetric, the dewetting velocity started to follow the already observed power law decay with exponent values $(0.35 \pm 0.1) \leq \alpha \leq (1 \pm 0.1)$. A general decrease in dewetting velocity was observed, a signature of slippage in the iPpMS608K films under study. The decrease in the dewetting velocity with time is also an indication that the residual stresses in iPpMS608K films under investigation are undergoing relaxation.

Further, the rim width surrounding the circular hole was also observed to decrease with increasing film thickness (Fig. 4.6(c)). From Figs. 4.7(a) - 4.7(b), we show how plots of initial dewetting velocity and maximum rim width as a function of incubation time can be used to extract the total driving stresses in iPpMS608K films prepared from different solution concentrations (different film thicknesses).

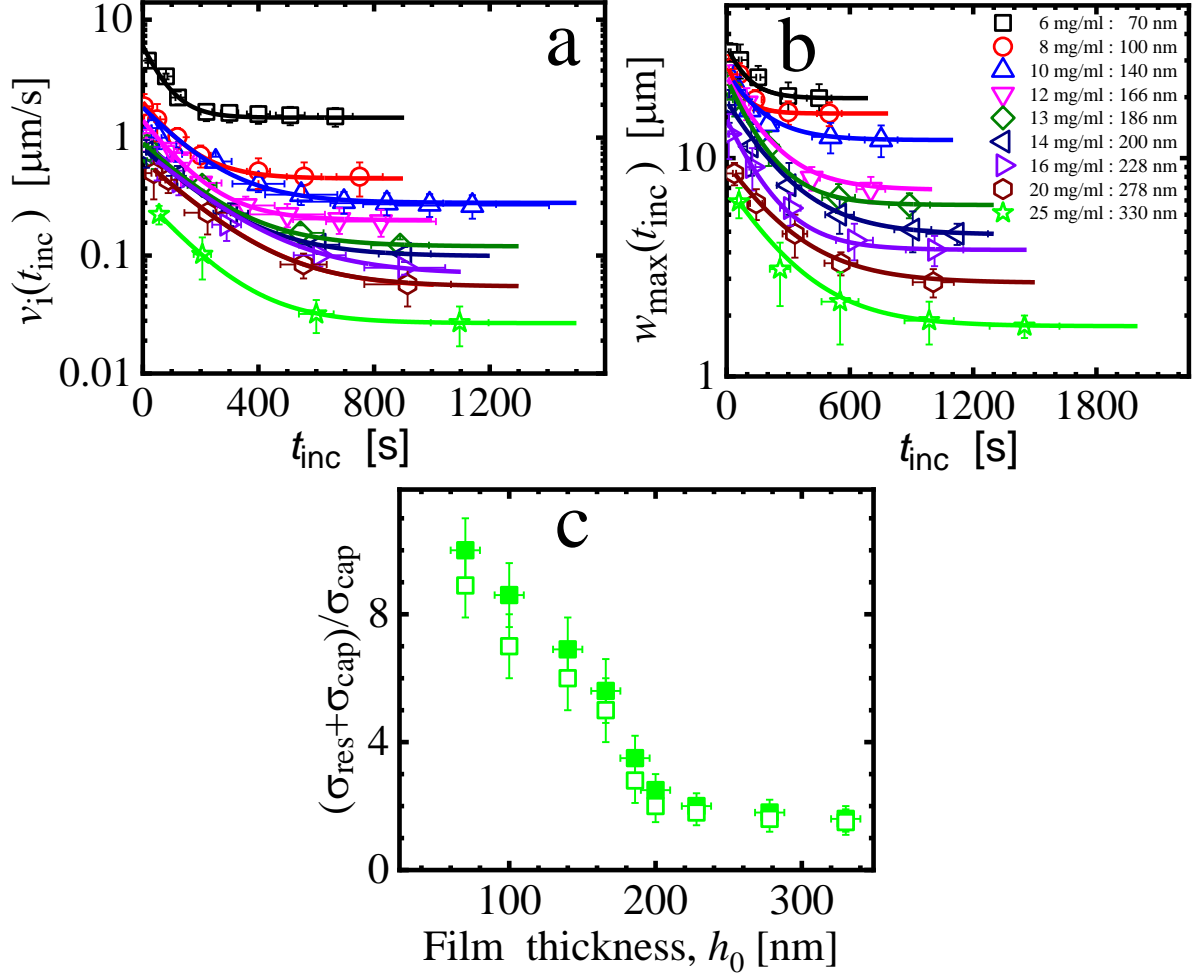


Fig. 4.7: Semi-logarithmic plots of (a) initial dewetting velocity ($v_i(t_{inc})$), (b) maximum rim width ($w_{max}(t_{inc})$) as a function of incubation time (t_{inc}). The symbols represent different solution concentration and corresponding film thickness as shown in (b). In (c), the ratio of total stress to capillary stress ($(\sigma_{res} + \sigma_{cap})/\sigma_{cap}$) is plotted as a function of film thickness for the first dewetting holes (at $t_{inc} \approx 0$ s) in *iPpMS608K* films at a constant spin-coating speed, prepared from different solution concentrations dewetting at 170 °C. Closed symbols in (c) represent $v_i(0)/v_i(\infty)$ and open symbols represent $w_{max}(0)/w_{max}(\infty)$.

In Figs. 4.7(a) - 4.7(b), we observe that the initial dewetting velocity and maximum rim width decreased with increasing solution concentration (film thickness). In addition, a general decay of initial dewetting velocity and maximum rim width with incubation time was observed. It is a clear indication that stress relaxation in *iPpMS608K* films is fast in films prepared from dilute solutions compared to concentrated solutions. This observation supports the presumption of possibility of out-of-equilibrium chain conformations in *iPpMS608K* films already observed

in atactic polystyrene (aPS) (Al Akhrass et al., 2008; Chandran, & Reiter, 2016, 2019; Chowdhury et al., 2012; Reiter, 2013). This is because increasing the iPpMS608K solution concentration leads to an increase in the number of chains, which comes closer to each other increasing packing density.

To extract relaxation time, τ_v from Fig. 4.7(a), we fitted the data to equation (4.3). However, to extract relaxation time, τ_w from Fig. 4.7(b), we fitted the data to the equation (4.6) below:

$$w_{\max}(t_{\text{inc}}) = A_w \cdot \exp(-t_{\text{inc}}/\tau_w) + w_{\max}(\infty) \quad (4.6)$$

where $A_w = w_{\max}(0) - w_{\max}(\infty)$, $w_{\max}(0) = w_{\max}(t_{\text{inc}} \rightarrow 0)$,

$w_{\max}(\infty) = w_{\max}(t_{\text{inc}} \rightarrow \infty)$, τ_w is the relaxation time with respect to maximum rim width.

How $w_{\max}(0)$, $w_{\max}(\infty)$ and A_w are obtained is similar to what has already been illustrated in Fig. 4.4(a) for the $v_1(t_{\text{inc}})$ data at a spin-coating speed of 500 rpm. Equation (4.6) can be re-written as:

$$w_{\max}(t_{\text{inc}})/w_{\max}(\infty) = 1 + A \cdot \exp(-t_{\text{inc}}/\tau_w) \quad (4.7a)$$

$$\text{with } A = A_w/w_{\max}(\infty) = [B_w - 1], \quad B_w = w_{\max}(0)/w_{\max}(\infty) \quad (4.7b)$$

Applying equation (4.5) on both the data from Figs. 4.7(a) - 4.7(b), we obtained the total amount of driving stresses whose ratio with respect to capillary stress we plot as a function of film thickness as shown in Fig. 4.7(c). It is clear from Fig. 4.7(c) that the ratio $(\sigma_{\text{res}} + \sigma_{\text{cap}})/\sigma_{\text{cap}}$ decreased with increase in film thickness to almost a constant value for $h_0 \geq 200$ nm (contribution of residual stresses varies by a factor of about 8). Therefore, on the premise of our observation, we can say that iPpMS608K films associated with large amount of residual stresses will relax 8 times faster than iPpMS608K films with less number of internal stresses. It simply means that the preparation-induced residual stresses are significantly higher

in thin films (prepared from low solution concentration) than in thick films (prepared from high solution concentration). Consequently, dewetting behaviour in thin *iPpMS608K* films for which $h_0 < 200$ nm is faster in comparison to those for which $h_0 \geq 200$ nm. It also alludes to the fact that thick *iPpMS608K* films are stable while thin ones tend to be unstable leading to increased hole nucleation as evidenced from Fig. 4.5(h). Therefore, it is not the thickness that decides the relaxation dynamics of internal stresses that gets associated with the film but it is the pathway of sample preparation that matters in line with the work of Chandran, & Reiter (2019). Generally, this observation leads to further understanding of *iPpMS* polymers under non-equilibrium conditions.

From the foregoing discussion, we may ask ourselves the question: What happens to the activation energy of *iPpMS608K* films when we vary solution concentration (or film thickness)? To answer this question, in Fig. 4.8, we demonstrate the effect of changing solution concentration on the relaxation times, $\tau_r \in \{\tau_v, \tau_w\}$ of *iPpMS608K* films at different dewetting temperatures ($T_{\text{dew}} \geq 120$ °C).

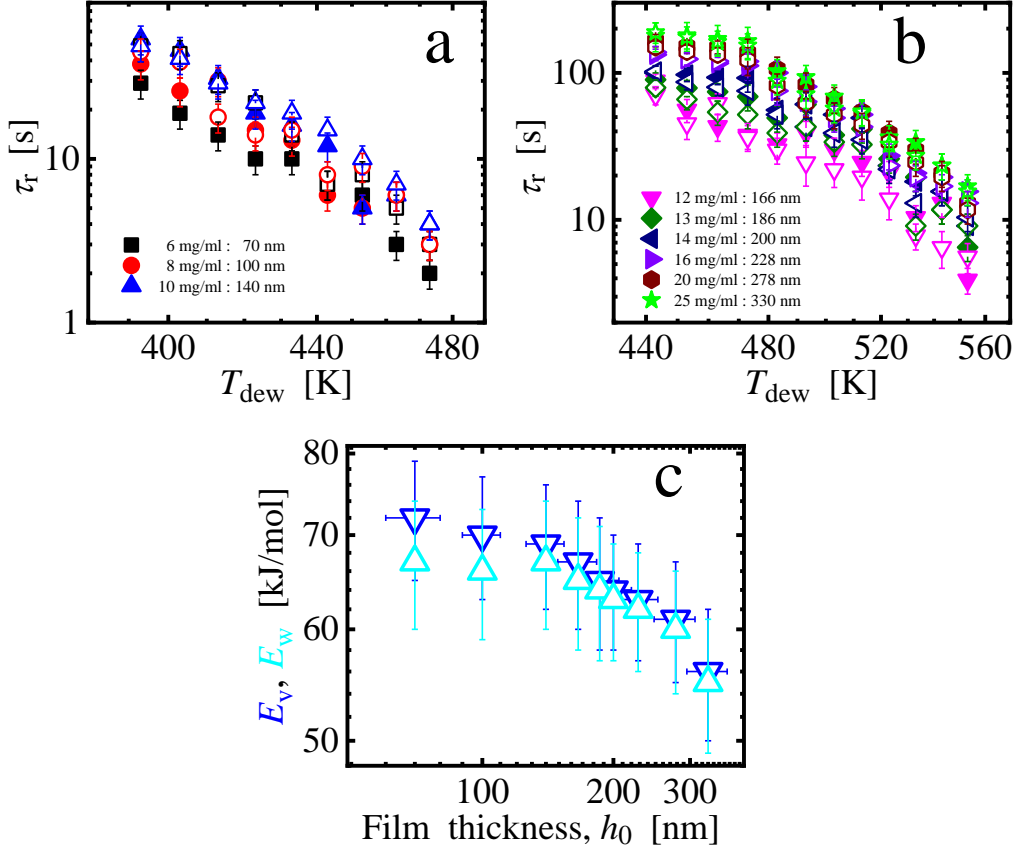


Fig. 4.8: Logarithmic plots of relaxation times, $\tau_r \in \{\tau_v, \tau_w\}$ as functions of T_{dew} : (a) for very thin films, $h_0 \leq 140$ nm ($T_{dew} = 120 - 200$ °C) and (b) for very thick films, $h_0 > 140$ nm ($T_{dew} = 170 - 280$ °C) in thin iPpMS608K films prepared from different solution concentrations but at constant spin-coating speed (500 rpm). The dewetting temperature was $T_{dew} \geq 120$ °C (393 K). Closed symbols represent τ_v while the open symbols represent τ_w . In (c) we plotted the activation energies as a function of film thickness in iPpMS608K films.

In Fig. 4.8(a) we plotted the variation of relaxation times with dewetting temperature. Dewetting in thin iPpMS608K films was characterized by two regimes: for $T_{dew} \geq 200$ °C (very thin films, $h_0 \leq 140$ nm) dewetting was very fast and exhibited many rim instabilities (Fig. 4.8(a)) whereas for $T_{dew} \leq 200$ °C (very thick films, $h_0 > 140$ nm) dewetting was very slow (Fig. 4.8(b)). We notice from Figs. 4.8(a) and 4.8(b) that the relaxation time of dewetting iPpMS608K films decreased with increase in dewetting temperature but increased with increase in solution concentration (or film thickness). At high dewetting temperatures (above melting temperature of iPpMS608K) the chain mobility in the iPpMS608K films increases and

the interface becomes more unfavorable leading to fast dewetting behaviour. This means residual stress relaxation is fast both at high dewetting temperature and low solution concentration (very thin films). Basically, rapid evaporation of highly concentrated solution during spin-coating iPpMS608K films does not cause enough quench depth which elongates main chains. Consequently, only few chains get frozen in out-of equilibrium conformations making very thick films to take longer time to relax as they are closer to equilibrium.

The characteristic activation energy, E_r ($r \in \{v, w\}$) (obtained from the plots of the relaxation times as functions of $1000/T_{\text{dew}}$) followed an Arrhenius-type behaviour (Chowdhury et al., 2016) with respect to equation (4.8);

$$\tau_r = \tau_0 \cdot \exp(E_r/k_B T_{\text{dew}}) \quad (4.8)$$

where $\tau_r \in \{\tau_v, \tau_w\}$, τ_0 is the proportionality factor, k_B is Boltzmann's constant.

In logarithmic form equation (4.8) can be written as:

$$\ln \tau_r = \ln \tau_0 + (-E_r/k_B T) \quad (4.9)$$

A slight decrease in the activation energy with increase in film thickness was observed (Fig. 4.8(c)).

In Fig. 4.9(a), we plotted the dewetting velocities as a function of dewetting time at longer incubation times ($t_{\text{inc}} \approx 1000$ s) for different solution concentration (film thickness) spin-coated at 500 rpm and in Fig. 4.9(b), we have a graph of maximum dewetting velocity (illustrated in Fig. 4.9(a)) as a function of film thickness in iPpMS608K films exhibiting a general decay possibly due to relaxation of residual stress within the films. Figure 4.9(c) illustrates how slip length can be estimated from a combined plot of hole radius, $R(t_{\text{dew}})$ and dewetting velocity, $v(t_{\text{dew}})$ as a function of dewetting time, (t_{dew}) especially for the holes

that nucleated at longer incubation time in comparison with the relaxation time, $t_{\text{inc}} \gg \tau_{\text{rel}}$

such that $R(t_{\text{dew}}) \sim t_{\text{dew}}^{-0.67 \pm 0.02}$ and $v(t_{\text{dew}}) \sim t_{\text{dew}}^{-0.35 \pm 0.02}$.

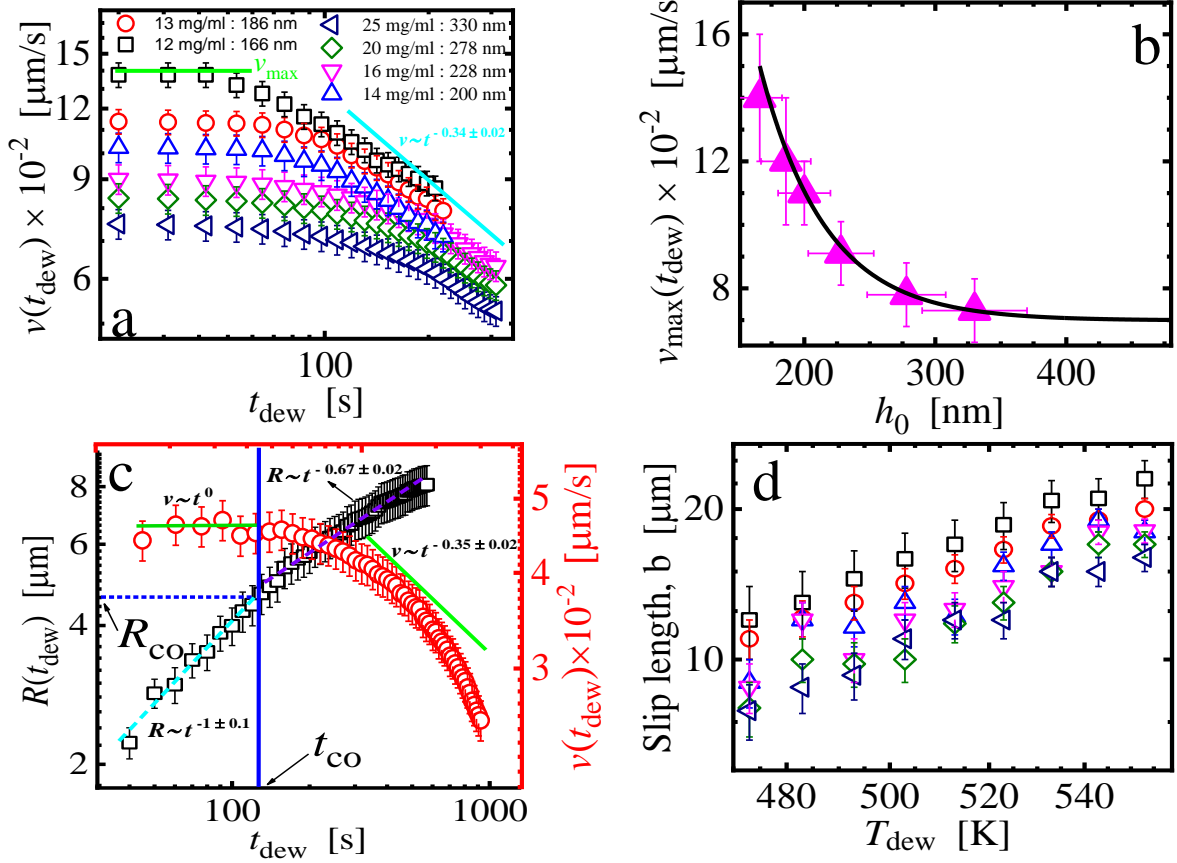


Fig. 4.9: (a) dewetting velocity, $v(t_{\text{dew}})$ as a function of dewetting time, t_{dew} for holes nucleated at $t_{\text{inc}} \approx 1000$ s for different solution concentration spin-coated at 500 rpm and dewetting at 200 °C in iPpMS608K films. (b) maximum dewetting velocity, $v_{\text{max}}(t_{\text{dew}})$ (from (a)) as a function of film thickness. (c) a combined logarithmic plot of hole radius ($R(t_{\text{dew}})$) and velocity ($v(t_{\text{dew}})$) as a function of dewetting time (t_{dew}) for the holes that nucleated at longer incubation time in comparison with the relaxation time, $t_{\text{inc}} \gg \tau_{\text{rel}}$ in iPpMS608K films prepared from 13 mg/ml at 500 rpm dewetting at 200 °C showing how a crossover radius (R_{co}) and crossover time (t_{co}) are estimated in iPpMS608K films. In (d), we plotted the estimated slip length based on (c) as a function of dewetting temperature, $T_{\text{dew}} \geq 200$ °C for the indicated thicknesses.

As a result of topological constraints (entanglements) between the iPpMS608K chains, the lower chains in contact with the slippery silicon substrates can experience slippage (Bäumchen et al., 2012; McGraw et al., 2014; Peschka et al., 2019; Reiter, 2013). Slippage is the hydrodynamic extrapolation length into the substrate where the dewetting velocity extrapolates to zero and can be determined by the ratio of the viscosity to the friction coefficient, $b =$

η/ξ as discussed in chapter two. The slip length can be determined at the point where the shape of the rim changes from asymmetric to symmetric and where the dewetting velocity changes from $v(t_{\text{dew}}) \sim t_{\text{dew}}^0$ to $v(t_{\text{dew}}) \sim t_{\text{dew}}^{-0.35 \pm 0.02}$ (Fig. 4.9(c)). In terms of crossover radius (R_{co}) and dynamic contact angle (θ_{dyn}) of the dewetting iPpMS608K films ($\theta_{\text{dyn}} \approx 0.42 \pm 0.03$ rad), the slip length is given by:

$$b = \eta/\xi = R_{\text{co}}/\theta_{\text{dyn}} \quad (4.10)$$

It is clear from Fig. 4.9(c) that in the regime of $v(t_{\text{dew}}) \sim t_{\text{dew}}^0$, the hole radius initially increased linearly such that $R(t_{\text{dew}}) \sim t_{\text{dew}}^{-1 \pm 0.1}$. Calculated values of the slip length, b were plotted as a function of dewetting temperature, $T_{\text{dew}} \geq 200$ °C for films prepared from different solution concentrations. We observed that the slip length increased with increase in dewetting temperature but a slight decrease with increase in solution concentration (film thickness). Increase in b with increasing temperature which is in conformity with already published work on aPS and iPS (Chandran et al., 2017; Chandran, & Reiter, 2016, 2019) may tentatively mean a decrease in time scale of cooperative dynamics or relaxation of cooperative clusters during dewetting process in iPpMS films. A decrease in slip length with increase in film thickness is an indication that the dissipation in the iPpMS608K films is also decreasing with increasing film thickness. In addition, the slip length was found to be much higher than the film thickness ($b \gg h_0$), an indication that all the investigated iPpMS608K films experienced a plug flow (full slip). It actually meant that the dewetting velocity gradient in the vertical direction was small compared to the horizontal profiles. Consequently, the energy dissipation happened only at the iPpMS608K - substrate interface (slippage) according to Reiter (2013).

For a polymer dewetting over a slippery substrate, the energy is dissipated throughout the whole moving part of the polymer film. In stress-free films, driving force and opposing force balances each other out such that (Boyd, & Smith, 2007; Reiter, 2013);

$$F_{\text{visc}} = (3\eta \cdot v_{\text{dew}} \cdot w)/b = 0.5 \cdot \gamma \cdot \theta^2 = F_c \quad (4.11)$$

where F_c is the capillary force (uncompensated Young's force), F_{visc} is the viscous force, w is the rim width, η is the viscosity of the polymer melt, b is the slip length, γ is the interfacial surface tension between solid-polymer, and θ is the contact angle the polymer melt makes with the substrate surface. From dewetting experiments, w (measured), v_{dew} (differentiation of hole radius), θ (measured), and b (obtained as in eqn. (4.10)) in the equation (4.12) are known and we use the surface tension of atactic poly(*para*-methylstyrene) (Kempf, Barroso, & Wilhelm, 2010; Kempf et al., 2013) to calculate viscosity in the form:

$$\eta = (\gamma \cdot \theta^2 \cdot b)/6(v_{\text{dew}} \cdot w) \quad (4.12)$$

Viscosities of iPPMS films of different solution concentration were obtained using equation (4.12) and the plots of viscosity as a function of inverse dewetting temperature is given in Fig. 4.10.

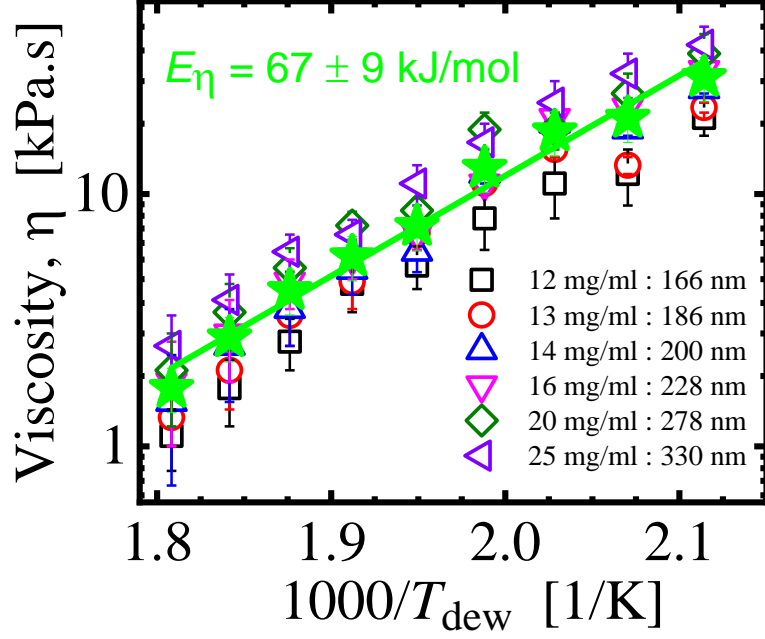


Fig. 4.10: Calculated viscosity, $\eta(T_{\text{dew}})$ as a function of inverse dewetting temperature for holes nucleated at $t_{\text{inc}} \approx 1000$ s for different solution concentration spin-coated at 500 rpm in iPpMS608K films.

All the viscosity data of Fig. 4.10 followed an Arrhenius-type equation of the form (Chandran, & Reiter, 2016; Chowdhury et al., 2012):

$$\eta = \eta_0 \cdot \exp(-E_\eta/k_B T) \quad (4.13)$$

where η is the viscosity, η_0 is a constant (zero viscosity), E_η is the activation energy, k_B is Boltzmann's constant and T is absolute temperature. Averagely, an activation energy of

67 ± 9 kJ/mol, was deduced.

4.2.2 Dynamics of dewetting temperature

In this section we discuss at length the effect of dewetting temperature on the viscoelastic properties in thin isotactic poly(*para*-methylstyrene) (iPpMS) films. Here, we chose a film thickness of 200 nm and iPpMS608K since we would like to observe dewetting behaviour for

longer periods of time. For thicknesses below 200 nm, the dewetting behaviour in iPpMS608K films at elevated temperatures was so fast that it was possible to miss some important dewetting steps. In addition, for thicknesses above 200 nm, the dewetting behaviour was too slow to allow a statistical description of what is taking place. Further, since dewetting behaviour in 200 nm iPpMS608K films below 170 °C was very slow and above 280 °C the dewetting process was very fast (could have led to chemical degradation in the iPpMS608K films under investigation), we chose a dewetting temperature range between 170 °C – 280 °C. Consider the random distribution of heterogeneously nucleated holes in a 200 nm iPpMS film shown in Fig. 4. 11.

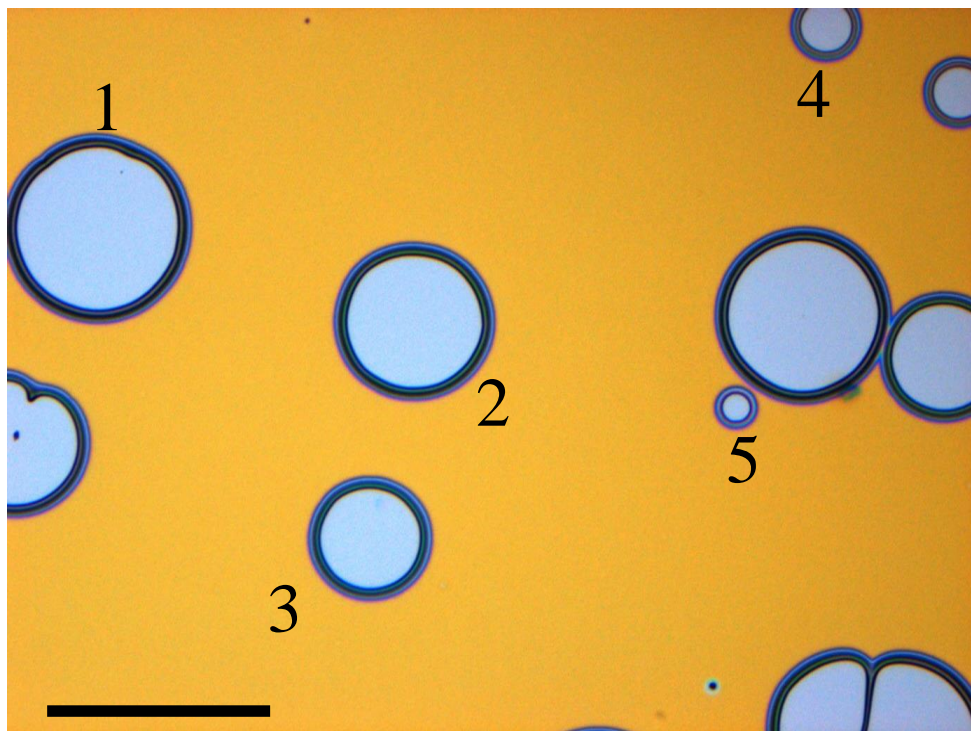


Fig. 4.11: Random nucleation of dewetting holes at different incubation times (t_{inc}) in a 200 nm iPpMS608K film at a dewetting temperature of $T_{dew} = 220$ °C (Size: $250 \times 250 \mu m^2$). Holes numbered 1, 2, 3, 4 and 5 were nucleated at $t_{inc} = 3$ s, 6 s, 12 s, 18 s and 34 s, respectively.

From Fig. 4.11, we observed randomly nucleated holes at different incubation times having different sizes. The differences in the growth of the holes at different incubation times, allowed

us to probe possible changes in viscoelastic properties of the iPPMS608K films within the same experiment as a function of t_{inc} . As time goes by, the holes increased in sizes and formed rims (accumulation of retracted polymer material around the formed holes) at the three-phase contact line due to volume conservation and interfacial friction. The rims appeared to be relatively wide with some color bands, indicating an expansion in the width and height of the rim during dewetting. The rim formation is attributed to a mismatch in the rate at which polymer is dislodged from the surface during hole opening and the rate at which it is diffused to other intact parts of the film (Bäumchen, & Jacobs, 2010). In Fig. 4.12, we show temporal evolution of a given dewetting hole. At late stages of dewetting at $T_{dew} > 220$ °C, the onset of rim instability (similar to Rayleigh-Plateau-type instability) (McGraw et al., 2010) was observed (Fig. 4.12(f)). The rim instability could also be due to dynamics of the moving front during the dewetting process and could be accelerated when there is slippage effect and increase in dewetting temperature (Peschka et al., 2019)). Formation of rim instability is due to the fact that the rim is not stationary but continuously expands in width and height as the dewetting hole grows. In this case, the rim would have broken to form isolated droplets as a way of minimizing the system's energy but it was constrained by the undewetted film surrounding the rim.

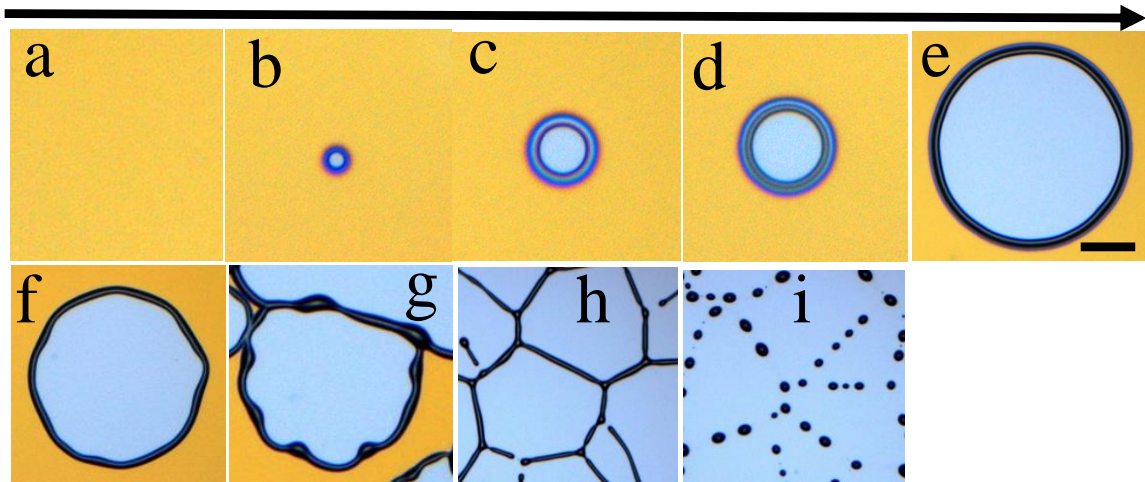


Fig. 4.12: Temporal evolution of a dewetting hole in a 200 nm iPpMS608K film at a dewetting temperature, $T_{\text{dew}} = 220 \text{ }^\circ\text{C}$ (Size: $100 \times 100 \text{ } \mu\text{m}^2$) from the nucleation stage until the rim becomes mature: (a) hole nucleation stage, (b) early rim formation stage, (c) increase in size of the rim (evidenced by different interference colours of the rim), (d) several layers (of different interference colours) of the growing rim and (e) mature rim (characterized by constant rim width), (f) – (i) show the onset of rim instability, coalescence, ribbons and droplets formation.

In the final dewetting stage, the ribbons formed in Figs. 4.12(g) – 4.12(h) break into polygonal droplet patterns after quite a long dewetting time, leading to an equilibrium configuration of liquid droplets (Brochard-Wyart et al., 1994; Brochard-Wyart, Martin, & Redon, 1993).

We present in Fig. 4.13 typical graphs for the radius, $R(t_{\text{dew}})$ of a dewetting hole, the dewetting velocity, $v_{\text{dew}}(t_{\text{dew}})$ and the width of the rim, $w(t_{\text{dew}})$ as functions of dewetting time, t_{dew} at different dewetting temperature, T_{dew} and various values of incubation time, t_{inc} .

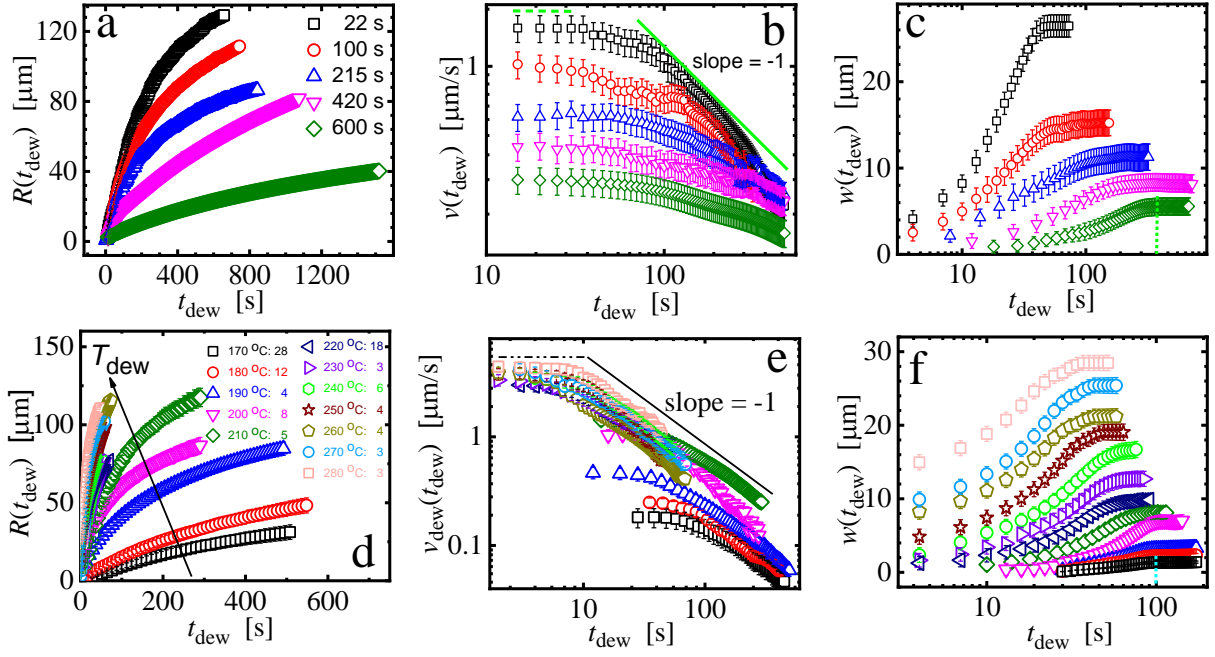


Fig. 4.13: (a) Radius, $R(t_{\text{dew}})$ of dewetting holes on linear scales, (b) corresponding dewetting velocity, $v_{\text{dew}}(t_{\text{dew}})$ on logarithmic scales and (c) width of the rim, $w(t_{\text{dew}})$ on semi-logarithmic scales as functions of dewetting time, t_{dew} for different incubation times, t_{inc} at a dewetting temperature of $T_{\text{dew}} = 220$ °C. (d) $R(t_{\text{dew}})$, (e) $v_{\text{dew}}(t_{\text{dew}})$ and (f) $w(t_{\text{dew}})$ at different $T_{\text{dew}} = 170 - 280$ °C for the first appearing holes at very short incubation times ($t_{\text{inc}} \approx 0$) on a 200 nm iPpMS608K films. The vertical broken lines in (c) and (f) indicate the time ($\tau_{w(\text{max})}$) at which the width of the rim reached a maximum value.

Increase in incubation time led to a decrease in hole radius, corresponding dewetting velocity and rim width (Figs. 4.13(a) - 4.13(c)). The rim width followed a logarithmic function of dewetting time and suddenly reached a maximum value (w_{max} (corresponds to maximum height of the rim) and then stayed constant. The rim width was observed to follow previously observed relation of the form $w \sim t^\alpha$ ($1/3 \leq \alpha \leq 2/3$). This scenario reflects presence of residual stresses at the start of dewetting in the iPpMS608K films. The time at which the rim width reaches a maximum value ($t_{\text{dew}} = \tau_{w(\text{max})}$) is important in the investigation of dewetting dynamics of iPpMS608K films as it indicates significant decay of the residual stresses (Reiter, 2013). Since we used thick films (ca. 200 nm) which contained only a moderate amount of residual stresses, we observed a constant rim width at times longer than

the relaxation time of residual stresses, which is in accordance with published reports (Chandran, & Reiter, 2016, 2019; Reiter, 2013; Vilmin, & Raphaël, 2005)

To understand the relaxation dynamics taking place in iPpMS608K films, initial dewetting velocity, $v_i(t_{\text{inc}})$ and maximum rim width, $w_{\text{max}}(t_{\text{inc}})$ (first holes) as a function of the incubation time, t_{inc} were plotted (Figs.4.14 (a) - 4.14(b)). Here, an exponential decay of the initial dewetting velocity and maximum rim width with incubation time was observed allowing us to be able to estimate the amount of total stress in the iPpMS608K films. We fitted an exponential decay function (equations (4.4) and (4.6)) to the measured values of $v_i(t_{\text{inc}})$ and $w_{\text{max}}(t_{\text{inc}})$ (Chandran, & Reiter, 2016, 2019; Reiter, 2013). Figure 4.4(a) has already illustrated how to extract initial dewetting velocity and by extension maximum rim width at both zero incubation time and longer incubation time $\{v_i(t_{\text{inc}} = 0), w_{\text{max}}(t_{\text{inc}} = 0); v_i(t_{\text{inc}} \rightarrow \infty), w_{\text{max}}(t_{\text{inc}} \rightarrow \infty)\}$ in the course of dewetting in addition to determination of the relaxation time. In Figs. 4.14(c) - 4.14(d), we have plotted normalized initial dewetting velocity and maximum rim width as a function of normalized incubation time. It shows how the graphs collapse into a one master curve to show the distribution of relaxation spectrum.

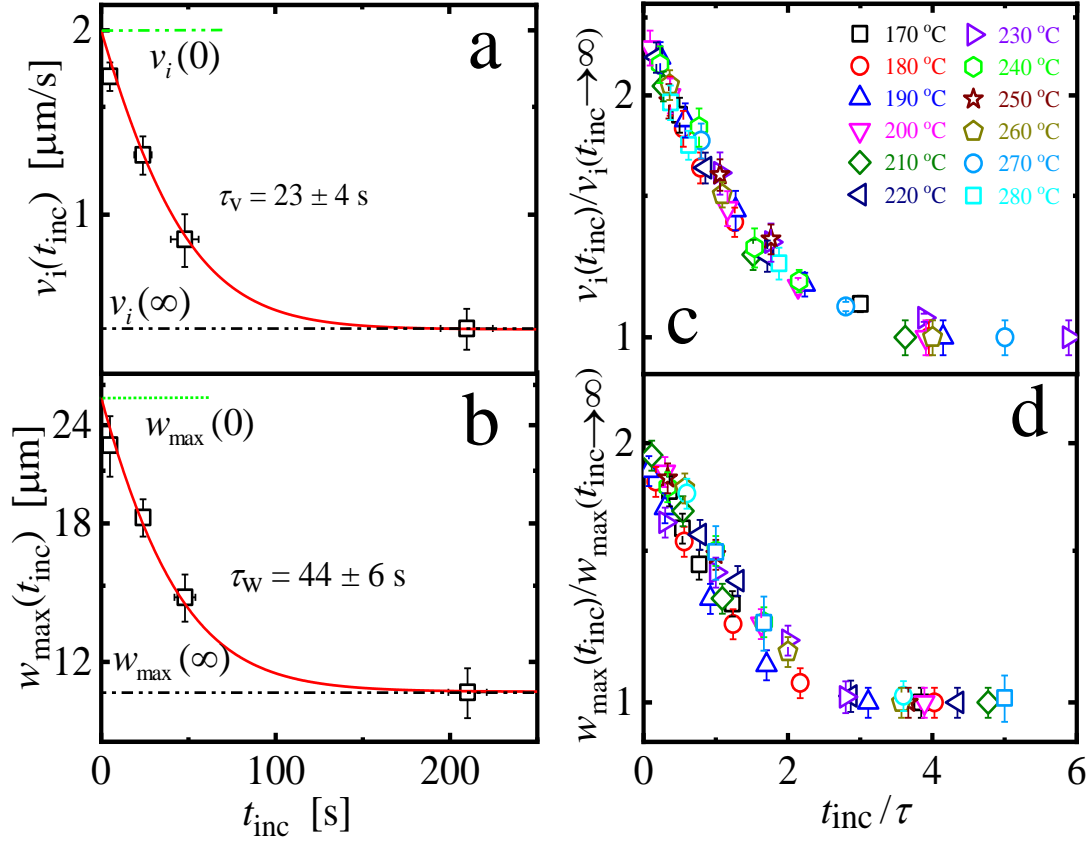


Fig. 4.14: Semi-logarithmic representation of (a) the initial dewetting velocity (v_i) and (b) the maximum width of the rim (w_{\max}) as a function of incubation time (t_{inc}) for holes nucleated progressively in a 200 nm spin-coated iPpMS608K film dewetting at 210 °C. The red lines represent the result of a fit of eqns. (4.4(a)) and (4.6) to the measured data points, yielding characteristic values. (c) and (d) represent the corresponding values of $v_i(t_{\text{inc}})/v_i(t_{\text{inc}} \rightarrow \infty)$ and $w_{\max}(t_{\text{inc}})/w_{\max}(t_{\text{inc}} \rightarrow \infty)$ measured at various temperatures as a function of t_{inc}/τ_r , $\tau_r \in \{\tau_v, \tau_w\}$.

The collapse of all data points of Figs. 4.14(c) - 4.14(d) indicated that we observed the same process at all T_{dew} . The characteristic relaxation times $\tau_{w(\max)}$, τ_v and τ_w for all measured dewetting temperatures, T_{dew} were plotted in Fig. 4.15 and compared with the published reptation times ($\tau_{\text{rep}}(M_w)$) at the corresponding temperatures. To obtain reptation times, the molecular weight of iPpMS (608 kg/mol) was rescaled based on published atactic PpMS (aPpMS) results such that (Kempf et al., 2013; Schluz, Handge, & Abetz, 2017);

$$\tau_{\text{rep}}(M_w) = \tau_{\text{rep}}(M_i^{\text{ref}}) \cdot \left(\frac{M_w}{M_i^{\text{ref}}} \right)^{3.4} \quad (4.14)$$

where $M_i^{\text{ref}} = 195 \text{ kg/mol}$ or $M_i^{\text{ref}} = 77 \text{ kg/mol}$. The corresponding reptation times were extrapolated to the dewetting temperature range (170 – 280 °C) by using the appropriate Williams – Landel - Ferry (WLF) equation (Kempf, Barroso, & Wilhelm, 2010; Kempf et al., 2013).

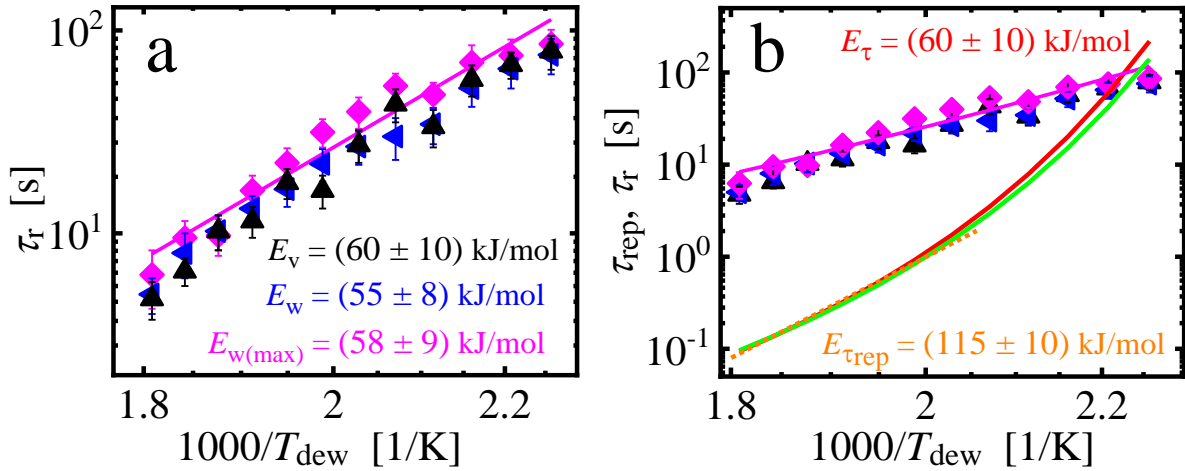


Fig. 4.15: A plot of characteristic relaxation times $\tau_r \in \{\tau_v, \tau_w, \tau_{w(\text{max})}\}$ and (b) $\tau_{\text{rep}}, \tau_r$ as a function of T_{dew}^{-1} for 200 nm spin-coated iPpMS608K thin films. The black, blue, and pink symbols represent τ_v, τ_w , and $\tau_{w(\text{max})}$, respectively. The pink line illustrates how an Arrhenius-type fitting to the data (pink symbols) is done yielding a single activation energy as indicated. The reptation times in (b) were obtained by employing the WLF equation to our experimental data with respect to published results in (Kempf, Barroso, & Wilhelm, 2010; Kempf et al., 2013) (red line) and (Schluze, Handge, & Abetz, 2017) (green line) as a function of T_{dew}^{-1} . The broken orange line at the highest temperatures represents an approximation of an Arrhenius-type behaviour with a single activation energy.

On average, an activation energy of $E_a \approx (60 \pm 10) \text{ kJ/mol}$ was obtained for the 200 nm iPpMS608K thin films under investigation. In contrast to the temperature dependence of the reptation times, which follows a WLF-type behaviour, the observed temperature dependence of the stress relaxation times rather followed an Arrhenius behaviour. At the highest temperatures, similar to the temperature range covered by our experiments, we could approximate the temperature dependence of the reptation times by an Arrhenius-type

characteristic with a single activation energy (Fig. 4.15(b)). Interestingly, this activation energy (*ca.* 115 kJ/mol) was approximately a factor of two higher than the values that we obtained from the Arrhenius-type behaviour of the stress relaxation times, an indication that the process of stress relaxation occurs on a shorter length scale than the reptation process (Chandran, & Reiter, 2016, 2019). Intriguingly, increasing temperatures to $T_{\text{dew}} \geq 200$ °C, the reptation time became shorter than our observed stress relaxation times. This is in accordance with previous observations on polystyrene films (Chandran, & Reiter, 2016, 2019; Reiter, 2013). Given the similarity of the here observed results on iPpMS608K with that of polystyrene, we conclude that preparation-induced residual stresses within spin-coated iPpMS608K films may relax also via concerted rearrangements of segments of non-equilibrated chains.

In Fig. 4.16, we plotted $B_v = \frac{v_i(t_{\text{inc}}=0)}{v_i(t_{\text{inc}} \rightarrow \infty)}$ and $B_w = \frac{w_{\text{max}}(t_{\text{inc}}=0)}{w_{\text{max}}(t_{\text{inc}} \rightarrow \infty)}$ as a function of dewetting temperature, T_{dew} . Here, $B_i (i = v, w) \equiv (\sigma_{\text{res}} + \sigma_{\text{cap}}) / \sigma_{\text{cap}}$. Interestingly, the ratio of B_i was independent of dewetting temperature, in accordance with the expectation that at the onset of dewetting (both incubation and dewetting times are zero) the amount of residual stresses is independent of dewetting temperature and only determined by how the films were prepared or aged.

We noted that B_v was somewhat larger than B_w because the maximum width of the rim was reached at a later dewetting time ($t_{\text{dew}} = \tau_{w(\text{max})} > 0$) than the initial dewetting velocity (determined at $t_{\text{dew}} \approx 0$). From Fig. 4.16, averagely,

$$\overline{B_v} = (\sigma_{\text{res}} + \sigma_{\text{cap}}) / \sigma_{\text{cap}} = 2.6 \pm 0.1 \text{ and } \overline{B_w} = 2.4 \pm 0.1, \text{ from which we obtained}$$

$$\sigma_{\text{res}} = (1.6 \pm 0.1)\sigma_{\text{cap}} \text{ and } \sigma_{\text{res}} = (1.4 \pm 0.1)\sigma_{\text{cap}}, \text{ respectively.}$$

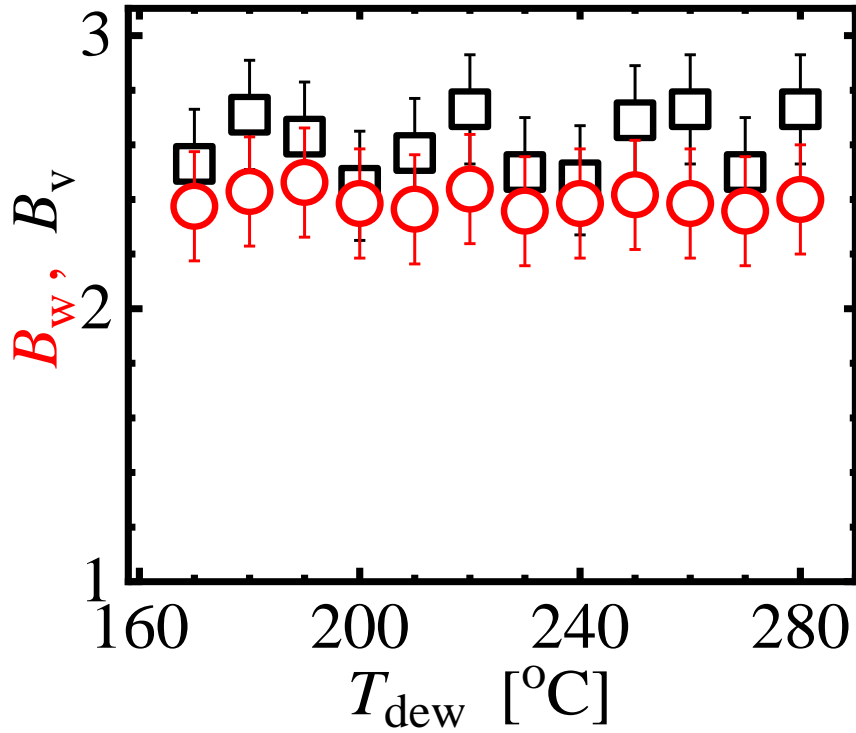


Fig. 4.16: Representation of the ratios $B_v = v_i(t_{\text{inc}} = 0)/v_i(t_{\text{inc}} \rightarrow \infty)$ and $B_w = w_{\text{max}}(t_{\text{inc}} = 0)/w_{\text{max}}(t_{\text{inc}} \rightarrow \infty)$ as a function of dewetting temperature (T_{dew}) for the earliest appearing dewetting holes in 200 nm iPpMS608K films. Black and red symbols represent B_v and B_w , respectively.

In Fig. 4.17, we present initial dewetting velocity, v_i as a function of T_{dew}^{-1} for holes nucleated at increasing incubation times (t_{inc}) including both $v_i(t_{\text{inc}} = 0)$ and $v_i(t_{\text{inc}} \rightarrow \infty)$. We observed that all values of v_i increased with increasing T_{dew} . Intriguingly, at $T_{\text{dew}} = 220 \text{ }^\circ\text{C}$ the slope ($dv_i(t_{\text{inc}} = 0)/dT_{\text{dew}}$) changed from a high value to a much smaller value. As $v_i(t_{\text{inc}} \rightarrow \infty)$ is proportional to the ratio of surface tension of iPpMS and the corresponding viscosity but also to the driving force represented by the contact angle and the slippage length, we only may speculate which parameter is responsible for such a change in behaviour as a function of temperature.

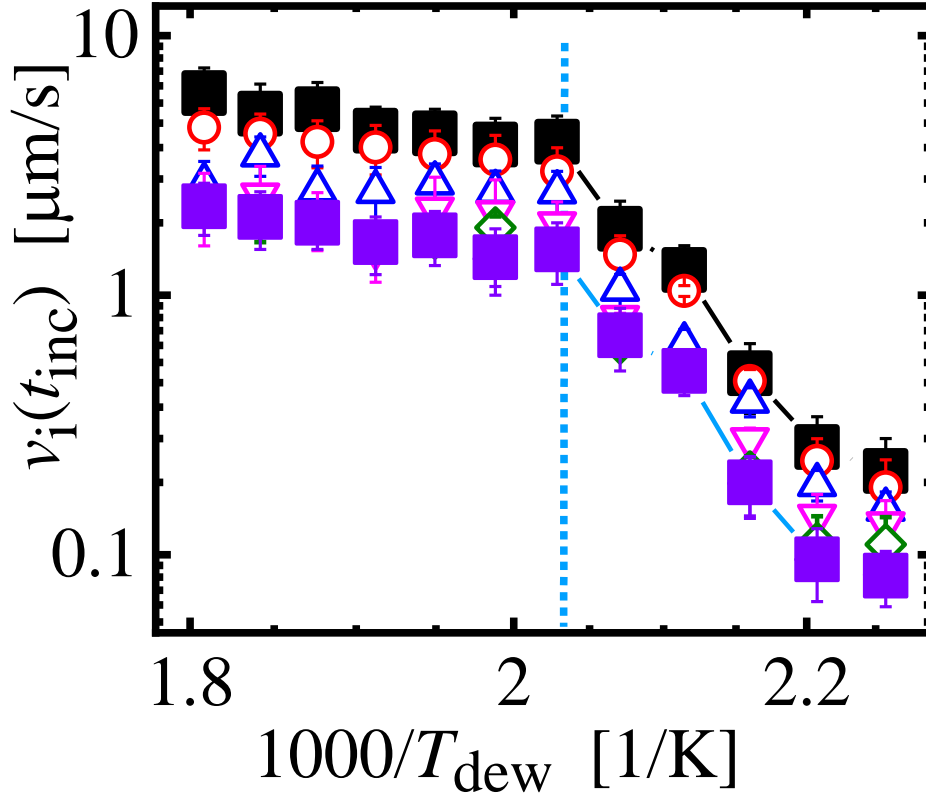


Fig. 4.17: Initial dewetting velocity ($v_i(t_{\text{inc}})$) as a function of T_{dew}^{-1} for dewetting holes nucleated at increasing t_{inc} . Open symbols represent measured values for different values of t_{inc} , closed symbols represent the limiting values at $t_{\text{inc}} = 0$ (black squares) and $t_{\text{inc}} \rightarrow \infty$ (purple squares), respectively, in 200 nm iPpMS608K films.

We may expect that preparation-induced residual stresses affect the viscoelastic properties of polymer films (Bodiguel, & Fretigny, 2006; Damman et al., 2007; Vilmin et al., 2006). To quantify these possible preparation-induced deviations in material properties (elastic modulus and viscosity), we examined how the height of the rim surrounding the dewetting front, a parameter related to the elastic behaviour of the polymer film, changed with σ_{res} . For dewetting of a purely elastic film, the height of the rim will reach a maximum value (H_{max}), which is determined by the value of the driving forces and the shear modulus (G) of the film (Vilmin, & Raphaël, 2005, 2006; Vilmin et al., 2006). Assuming that dewetting is driven only by

capillary stress $\sigma_{\text{cap}} = |S|/h_0$ (S is the spreading coefficient and h_0 is the initial film thickness) acting at the contact line of the dewetting hole, we obtain the following relation:

$$H_{\text{max}} = (H(\tau_{w(\text{max})}) - h_0) = |S|/G \quad (4.15)$$

Due to chains trapped in strongly out-of-equilibrium conformations, spin-coated thin glassy polymer films in general, and the here examined films of iPpMS608K as well, are expected to exhibit residual stresses. Thus, dewetting is driven by the combined action of capillary stress and residual stresses, i.e., H_{max} is given by $(H(\tau_{w(\text{max})}) - h_0) = \frac{|S|}{G} + \frac{\sigma_{\text{res}}}{G} h_0$. Assuming a linear response to the applied stress (Hooke's law), one can define the maximum strain ε_{max} by $\varepsilon_{\text{max}} = \frac{(\sigma_{\text{cap}} + \sigma_{\text{res}})}{G} = (H(\tau_{w(\text{max})}) - h_0)/h_0$ (Vilmin, & Raphaël, 2005, 2006; Vilmin et al., 2006; Reiter, 1993). Dewetting of purely elastic films or viscoelastic polymer films at early stages (i.e., at times shorter than a characteristic relaxation time of the system) will eventually generate a rim with a well-defined height H_{max} .

Accounting for mass conservation (assuming constant density of the fluid), we get $R(t_{\text{dew}}) \cdot h_0 = 2w(t_{\text{dew}})(H(\tau_{w(\text{max})}) - h_0)$. Thus, $\varepsilon_{\text{max}} = (H(\tau_{w(\text{max})}) - h_0)/h_0 = R_{\text{max}}/2w_{\text{max}}$, with R_{max} being the radius of the dewetting hole at the time $\tau_{w(\text{max})}$ when w_{max} is reached.

In Fig. 4.18(a), we plotted the ratio $R(t_{\text{dew}})/2w(t_{\text{dew}})$ as a function of $w(t_{\text{dew}})$, while in Fig. 4.18(b), we present the measured values at the constant point in Fig. 4.18(a) such that $R_{\text{max}}/2w_{\text{max}} = \varepsilon_{\text{max}}$ as a function of T_{dew} .

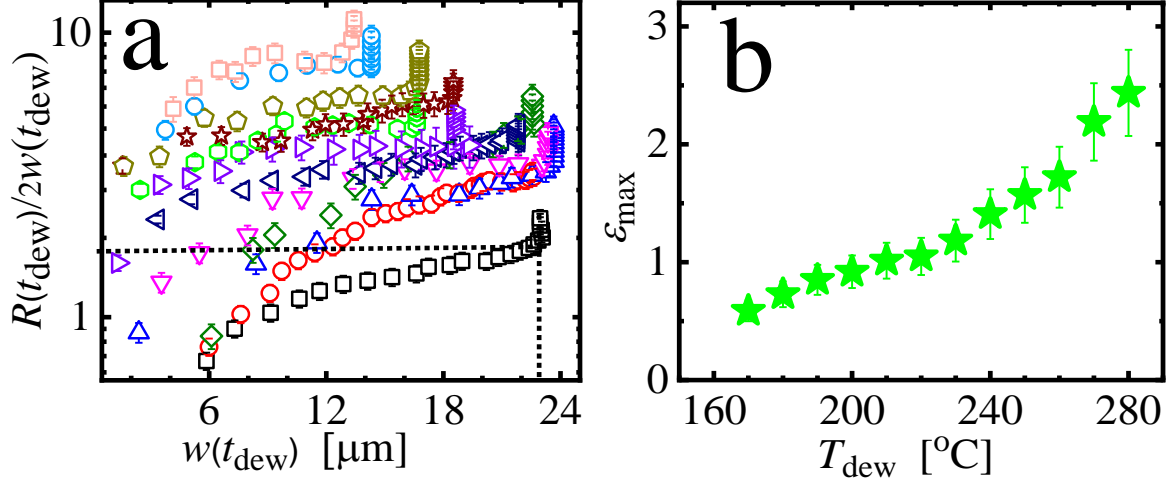


Fig. 4.18: (a) Ratio of $R(t_{\text{dew}})/2w(t_{\text{dew}})$ as a function of $w(t_{\text{dew}})$ for the earliest nucleated dewetting holes in 200 nm iPPMS608K films at various T_{dew} and (b) plot of ε_{max} as a function of T_{dew} .

The graphs in Fig. 4.18(a) exhibited a region of almost constant values of $R(t_{\text{dew}})/2w(t_{\text{dew}})$ followed by a strong increase at almost constant $w(t_{\text{dew}})$. This transition occurred at $\tau_{w(\text{max})}$ (time at maximum rim width). The value of $R(t_{\text{dew}})/2w(t_{\text{dew}})$ at this transition point, indicated by the horizontal dotted line is identified as $R_{\text{max}}/2w_{\text{max}} = \varepsilon_{\text{max}}$ (maximum strain) while the one indicated by the vertical line is the maximum rim width, $w(\text{max})$ (another way of measuring maximum rim width). We note that ε_{max} increased with increasing T_{dew} (Fig. 4.18(b)). Assuming a Hookean relation $\varepsilon = \sigma/G = \frac{\sigma_{\text{cap}} + \sigma_{\text{res}}}{G}$ and accounting for the independence of $(\sigma_{\text{cap}} + \sigma_{\text{res}})$ on T_{dew} (see Fig. 4.16) allows us to translate $\varepsilon_{\text{max}}(T_{\text{dew}})$ shown in Fig. 4.18(b) into (Bodiguel, & Fretigny, 2006; Vilmin, & Raphaël, 2005, 2006; Vilmin et al., 2006; Reiter, 1993);

$$G(T_{\text{dew}}) = \sigma_{\text{cap}} \cdot (\overline{B}_v) / \varepsilon_{\text{max}}(T_{\text{dew}}) \quad (4.16)$$

Or

$$G(T_{\text{dew}}) = \sigma_{\text{cap}} \cdot (\overline{B}_w) / \varepsilon_{\text{max}}(T_{\text{dew}}) \quad (4.17)$$

where $G(T_{\text{dew}})$ is the shear stress modulus.

The results for the values of $G(T_{\text{dew}})$ as a function of T_{dew} are shown in Fig. 4.19(a).

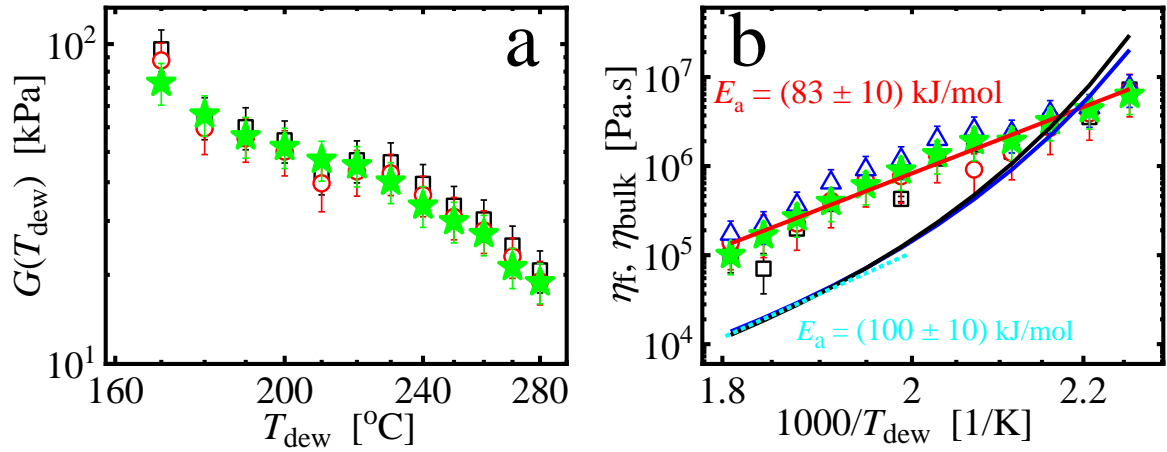


Fig. 4.19: Representation of the values of (a) $G(T_{\text{dew}})$ as a function of T_{dew} (open black and red symbols are based on B_v and B_w , respectively) and (b) $G(T_{\text{dew}}) \cdot \tau(T_{\text{dew}})$ as a function of T_{dew}^{-1} (open black, red and blue symbols are based on τ_v , τ_w and $\tau_{w(\text{max})}$, respectively) together with averaged values (green stars). The full red line in (b) represents the Arrhenius-type line fit with a single activation energy to the averaged values. Data for the bulk modulus curves were obtained from Kempf et al. (2013). Dewetting experiments were performed on 200 nm iPpMS608K films.

Based on the Maxwell model described by eqn. (2.8) (Ferry, 1980; Young, & Lovell, 1991), we can further translate $G(T_{\text{dew}})$ multiplied by the measured relaxation times $\tau(T_{\text{dew}})$ shown in Fig. 4.15 into an effective viscosity $\eta(T_{\text{dew}})$ of 200 nm iPpMS608K films:

$$\eta(T_{\text{dew}}) = G(T_{\text{dew}}) \cdot \tau(T_{\text{dew}}) \quad (4.18)$$

The corresponding results are shown in Fig. 4.19(b) in an Arrhenius-type way, yielding an activation energy of 83 ± 10 kJ/mol, which represents a value similar to the one observed for isotactic polystyrene (Chandran, & Reiter, 2016, 2019; Chowdhury et al., 2016; Reiter, 2013).

4.2.3 Analysis of dewetting dynamics in iPpMS –iPS blend system

Mixing isotactic poly(*para*-methylstyrene) (iPpMS608K) with isotactic polystyrene (iPS400K) led to different dewetting dynamics in the iPpMS – iPS400K blend system. For instance, the number of holes nucleated per given area of the substrate varied with the amount of iPS400K present in the mixture (solution concentration and spin-coating speed remained constant at 14 mg/ml and 500 rpm, respectively) as shown from the optical micrographs in Fig. 4.20.

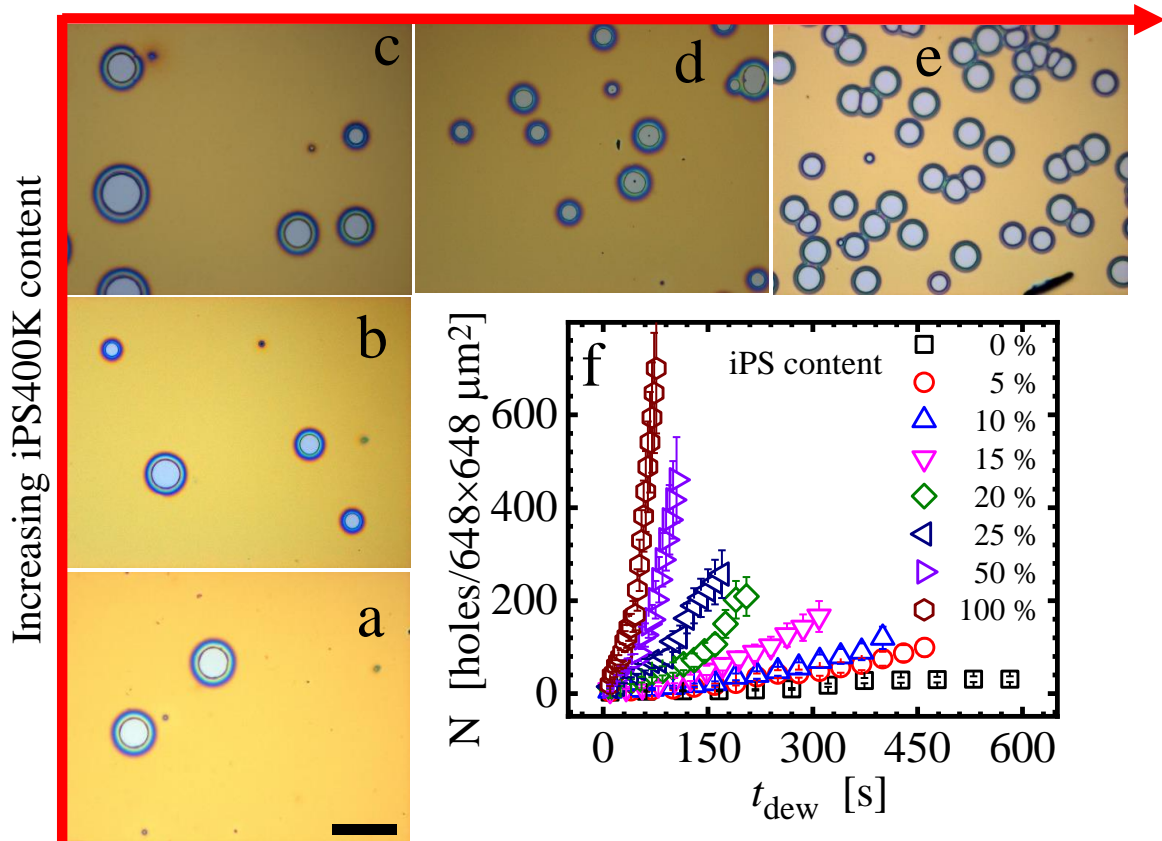


Fig. 4.20: Optical micrographs showing nucleated holes obtained from a 200 nm *iPpMS608K* – *iPS400K* films at different *iPS400K* content: (a) 0 % *iPS400K* (100 % *iPpMS608K*), (b) 5 % *iPS400K*, (c) 15 % *iPS400K*, (d) 25 % *iPS400K* and (e) 100 % *iPS400K* (0 % *iPpMS608K*) for the first dewetting holes (at annealing time, $t_{\text{ann}} \approx 90$ s) at $T_{\text{dew}} = 170$ °C. In (f), the number of nucleated holes are plotted as a function of dewetting time (t_{dew}). Each micrograph measures $648 \times 648 \mu\text{m}^2$. The legend in (f) shows *iPS400K* content.

In Figs. 4.20(a) – 4.20(e), hole nucleation density is shown through optical micrographs of *iPpMS608K* – *iPS400K* films dewetting at a constant temperature. It is clear from the micrographs that increase in *iPS400K* content leads to increased hole nucleation in the films. Consequently, we may ask: Could the increase in hole nucleation with increase in *iPS400K* content mean that the residual stresses in *iPS400K* films is greater than those of *iPpMS608K*? To find answers to the question, we followed individual hole evolution and analyzed their radii, velocities and rim width to help us to be in a position to extract residual stresses as *iPS400K* content varied. Chang, & Woo (2003a) showed that *iPS* and *aPpMS* were immiscible at all

studied compositions. Only for blends of low molecular weight iPS ($M_w \leq 20$ kg/mol) with aPpMS, they observed an UCST ≈ 270 °C (Chang, & Woo, 2003b).

According to previous studies, iPS and atactic PpMS (aPpMS) were immiscible (Müller-Buschbaum, Gutmann & Stamm, 2000; Müller-Buschbaum et al., 1998; Xenopoulos et al., 1994) but no studies on miscibility on iPS and iPpMS have been done so far. Differential scanning calorimetry did not yield any reliable result. Further, the images obtained from OM and AFM (Fig. 4.21), neither showed any evidence for the presence of two separate layers of iPpMS608K and iPS400K nor any signs of phase separation in the films.

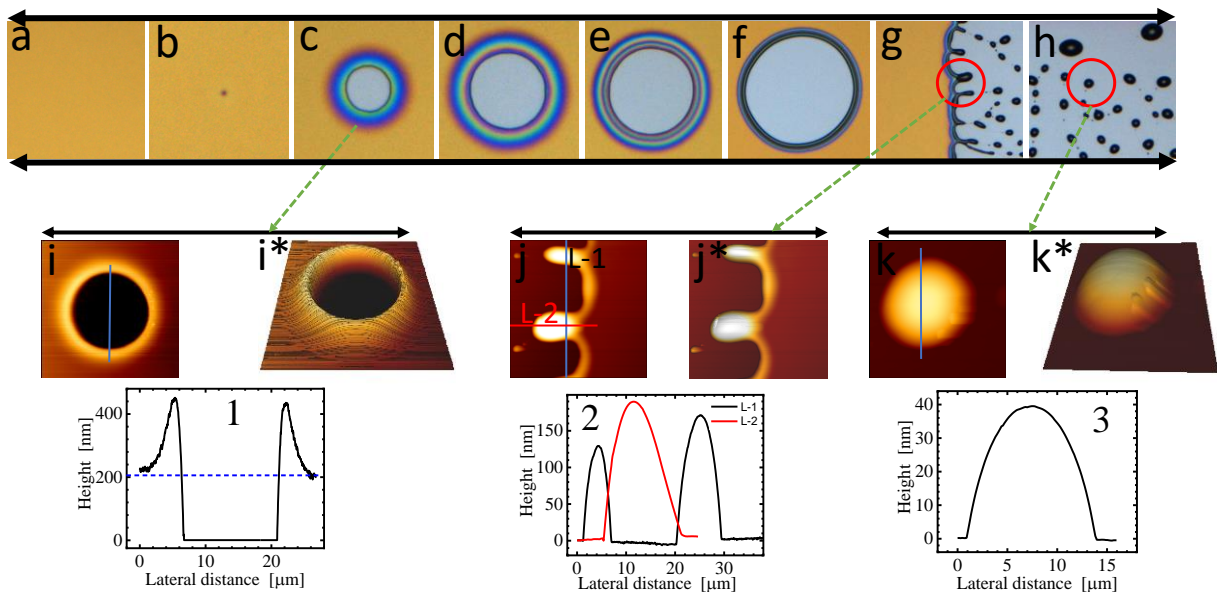


Fig. 4.21: Optical micrographs and AFM images for the 95 % iPpMS608K – 5 % iPS400K binary system dewetting at $T_{\text{dew}} = 240$ °C and at different incubation times: (a) shows a 200 nm film before dewetting experiment. (b) – (d) show dewetting process for shorter incubation times and (e) – (h) show dewetting process at longer incubation times. (i) (2D) and (i*) (3D), (j) (2D) and (j*) (3D), (k) (2D) and (k*) (3D) are the AFM images of (c), circled section in (g) and circled droplet in (h), respectively. The graphical representation of the indicated lines in (i), (j) and (k) are also given in (1), (2) and (3), respectively. The scale for (a) – (d) is $110 \times 110 \mu\text{m}^2$ whereas for (e) – (h) it is $225 \times 225 \mu\text{m}^2$.

We note that toluene was a common solvent for the two polymers which allowed to dissolve both polymers homogeneously. After spin-coating, smooth and featureless films of a constant thickness were obtained. These freshly prepared films of non-equilibrated polymers were used

for our dewetting studies. Interestingly, for films of the blend of the two polymers, we observed a qualitatively similar behaviour as for freshly prepared films of either pure iPS400K or pure iPpMS608K. However, the results showed clear quantitative differences. Typical results for the growth of the radius, $R(t_{\text{dew}})$, of dewetting holes, the corresponding dewetting velocity, $v_{\text{dew}}(t_{\text{dew}})$, and the width of the rim surrounding the dewetting holes, $w_{\text{dew}}(t_{\text{dew}})$, as a function of dewetting time, t_{dew} , are shown in Fig. 4.22.

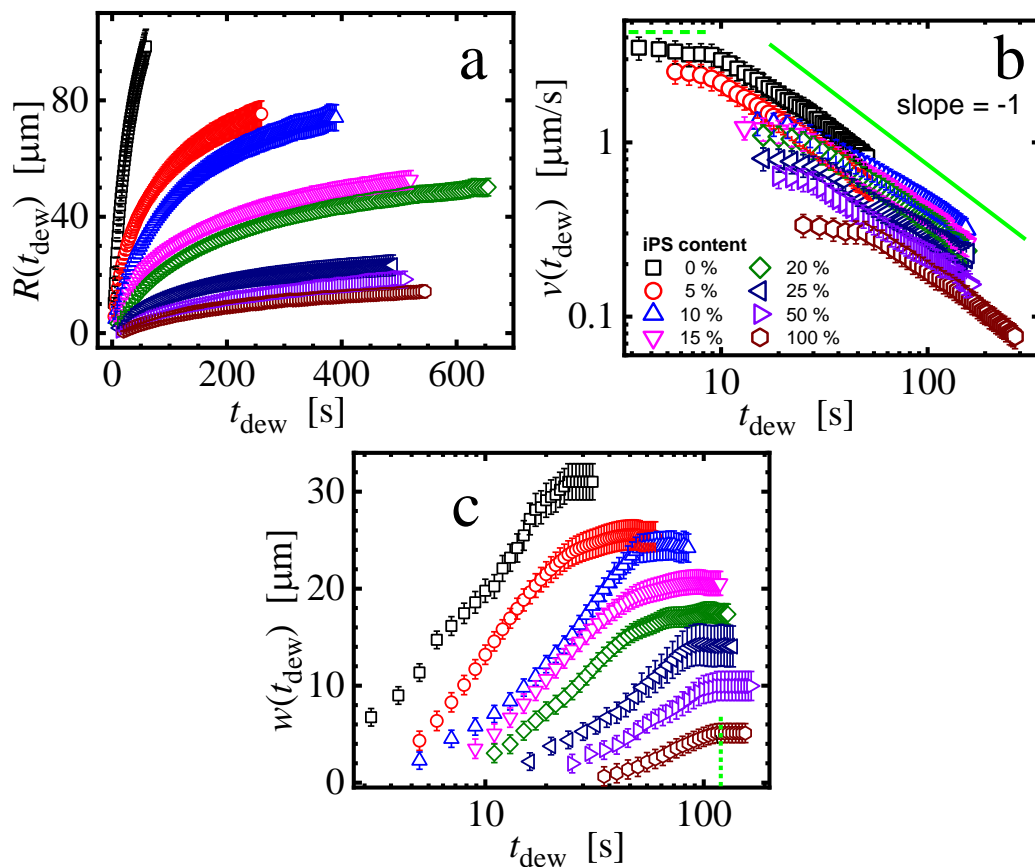


Fig. 4.22: (a) A linear plot of $R(t_{\text{dew}})$, (b) double logarithmic plot of $v_{\text{dew}}(t_{\text{dew}})$ and (c) semi-logarithmic plot of $w_{\text{dew}}(t_{\text{dew}})$ as a function of dewetting time t_{dew} in 200 nm iPpMS608K – iPS400K blend films dewetting at $T_{\text{dew}} = 240$ °C for the first observed dewetted holes starting after the shortest measured incubation time. The iPS400K content ranges from 0 to 100 %, as indicated in (b) by the different symbols and colors. The dotted straight line in the lower right corner in (c) is a guide to the eyes indicating the time when the maximum rim width $w_{\text{max}}(t_{\text{max}})$ for a pure iPS400K film was obtained.

At a constant dewetting temperature (T_{dew}), we noticed a slowing down of the dewetting process as we increased the iPS400K content in the iPpMS608K matrix, visible for $R(t_{\text{dew}})$ (Fig.4.22(a)) and for $v_{\text{dew}}(t_{\text{dew}})$ Fig.4.22(b)). At each T_{dew} and for each iPS400K content in the film, at the onset of dewetting, $v_{\text{dew}}(t_{\text{dew}})$ was approximately constant for a short period of time (~ 10 s) but decreased roughly according to a power law ($v_{\text{dew}}(t_{\text{dew}}) \sim t^{-1}$) at later times, a signature which can be related to stress relaxation in thin polymer films. While v_{dew} increased with increasing T_{dew} , with increasing iPS400K content v_{dew} decreased. In parallel, we observed a decrease in the width of the rim $w_{\text{dew}}(t_{\text{dew}})$ with the increase in iPS400K content (Fig.4.22(c)). During early stages of rim build-up, $w_{\text{dew}}(t_{\text{dew}})$ increased with time approximately logarithmically until the time $\tau_{w_{\text{max}}}$, when a maximum value (w_{max}) of the width of the rim was reached. At times longer than $\tau_{w_{\text{max}}}$, $w_{\text{dew}}(t_{\text{dew}})$ remained approximately constant at the value of w_{max} . The much faster dewetting velocity for iPpMS608K is surprising as the zero-shear viscosity of iPS400K in equilibrium has been found to be less than that of iPpMS608K, consistent with the entanglement molecular weight: iPS400K ($M_e = 28800$ g/mol) (Wu, 1989) is less entangled than iPpMS608K ($M_e \approx 20400$ g/mol) (Fetters, Lohse & Graessley, 1999).

In Fig. 4.23, we demonstrate how the initial dewetting velocity $v_i(t_{\text{inc}})$ (determined for $t_{\text{dew}} \rightarrow 0$) (Fig. 4.23a)) and the maximum rim width $w_{\text{max}}(t_{\text{inc}})$ (Fig. 4.23(b)) decreased with incubation time. A decrease of these parameters with incubation time is an indication for the relaxation of residual stresses in the films of the blend.

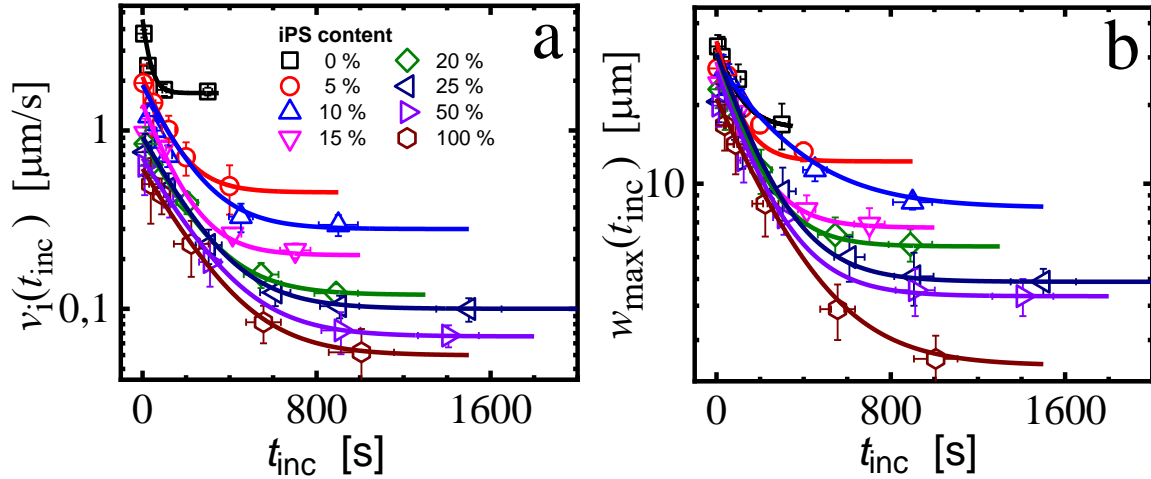


Fig. 4.23: Semi-logarithmic plot of (a) $v_i(t_{\text{inc}})$ and (b) $w_{\text{max}}(t_{\text{inc}})$ as a function of incubation time t_{inc} for 200 nm iPpMS608K – iPS400K blend films of varying iPS400K content dewetting at $T_{\text{dew}} = 240$ °C. The iPS400K content ranges from 0 to 100 %, as indicated in (a) by the different symbols and colors.

We used the equations (4.3) and (4.6) to fit the data in Fig. 4.23. In addition, $\tau_r \in \{\tau_v, \tau_w\}$ were found from the fitting and represent the characteristic time for the relaxation of residual stresses in the blend film. Figs. 4.23(a) and 4.23(b) reveal that the decrease in $v_i(t_{\text{inc}})$ and $w_{\text{max}}(t_{\text{inc}})$ with increasing iPS400K content is accompanied by an increase in τ_v and τ_w . From Fig. 4.23, we can conclude that the relaxation of residual stresses in films of a polymer blend can be characterized by the two parameters τ_r and A_i : The rate of the decay and the amount of the corresponding maximum changes in the dewetting velocity and the maximum width of the rim. Both parameters varied monotonically with the content of iPS400K.

Next, we plotted in Fig. 4.24, $v_i(t_{\text{inc}})/v_i(t_{\text{inc}} \rightarrow \infty)$ and $w_{\text{max}}(t_{\text{inc}})/w_{\text{max}}(t_{\text{inc}} \rightarrow \infty)$ as a function of reduced incubation time $t^* = t_{\text{inc}}/\tau_r$. The plot led to a collapse of all data points onto a single master curve. This observation is suggesting that at all temperatures the same type of dewetting process occurs in all the blends.

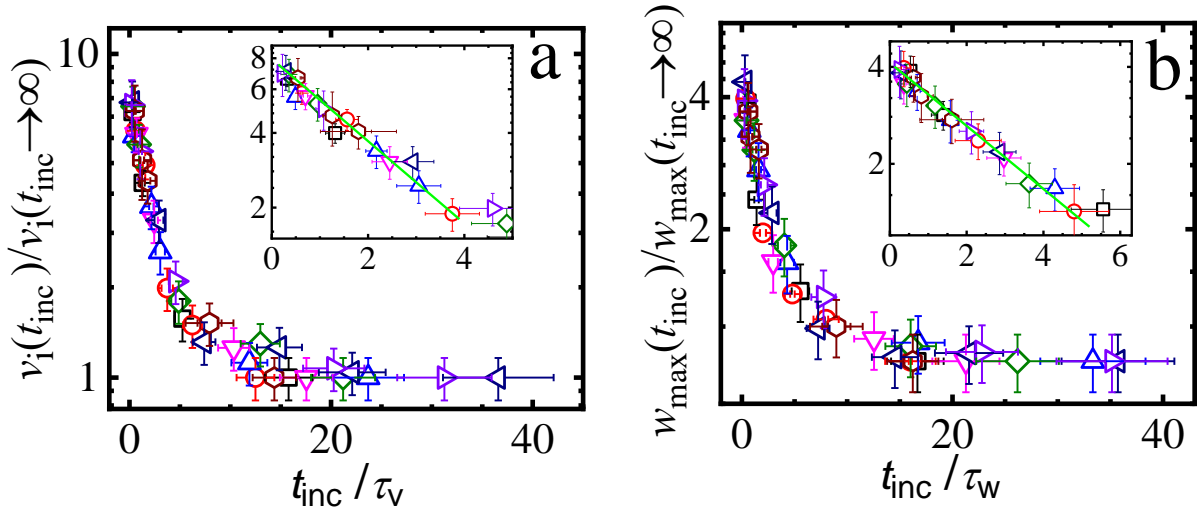


Fig. 4.24: Semi-logarithmic plot of (a) normalized initial dewetting velocity $v_i(t_{\text{inc}})/v_i(t_{\text{inc}} \rightarrow \infty)$ and (b) normalized maximum rim width $w_{\text{max}}(t_{\text{inc}})/w_{\text{max}}(t_{\text{inc}} \rightarrow \infty)$ as a function of reduced incubation time t_{inc}/τ_r , $\tau_r \in \{\tau_v, \tau_w\}$ for 200 nm iPpMS608K – iPS400K blend films of varying iPS400K content dewetting at $T_{\text{dew}} = 240$ °C. The symbols and colors have the same meaning as in Fig. 4.22. The insets show the same data at short times.

We plot $B_v = v_0/v_\infty$ and $B_w = w_0/w_\infty$ as a function of T_{dew} (Fig. 4.25). We observed from Figs. 4.25(a) - 4.25(b) that the values of B_v and B_w did not depend on T_{dew} . This observation is in accordance with previous observations for pure iPpMS608K films. As all films for each blend of a given iPS400K content have been prepared in the same way by spin-coating, we anticipated that the value of the amount of residual stresses did not depend on T_{dew} . In addition, this independence on T_{dew} may also imply that dewetting was faster than possible phase separation. All films were characterized by the same type of local and global segmental relaxation behaviour, independent of iPS400K content (Colmenero, & Arbe, 2007; Okada, 1979).

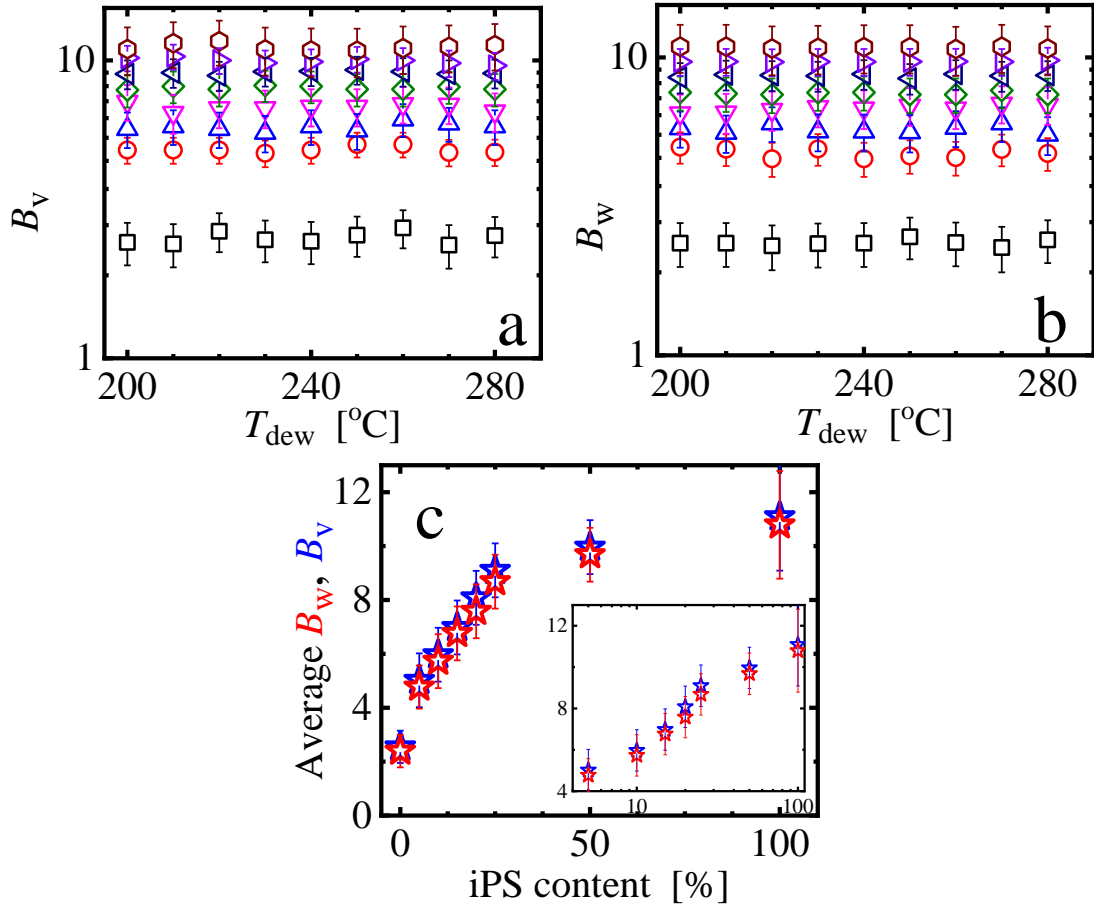


Fig. 4.25: Logarithmic plot of ratios (a) B_v , (b) B_w as a function of T_{dew} for 200 nm iPpMS608K – iPS400K blend films of varying iPS400K content. The symbols and colors have the same meaning as in Fig. 4.22. (c) Linear plot of the mean values of B_v (blue stars) and B_w (red stars) averaged over all dewetting temperatures as a function of iPS400K content. The inset shows the same data points on a logarithmic scale of the iPS400K content, suggesting that the amount of residual stresses in the blend films increased with the logarithm of the iPS400K content.

In dewetting of thin non-equilibrated polymer films, the total driving force, σ_{tot} , is given by $\sigma_{tot} = \sigma_{cap} + \sigma_{res}$ (σ_{cap} is the capillary stress and σ_{res} is the residual stress) (Chandran, & Reiter, 2016, 2019). While residual stresses relax with (incubation) time, the capillary stress remains constant for a given system at a fixed dewetting temperature. Thus, at $t_{inc} \rightarrow 0$, the initial driving force is given by $\sigma_{tot} = \sigma_{cap} + \sigma_{res}(t_{inc} \rightarrow 0)$, which is reflected in the ratios B_v and B_w .

Another observation from Figs. 4.25(a) and 4.25(b) is that the values of B_v and B_w increased monotonically by a factor of about 5 when the iPS400K content increased from 0 % to 100 %. Accordingly, we can conclude that residual stresses in pure iPS400K films were a factor of about 5 higher than in pure iPPMS films. The values for all blends were in between these two extreme values. However, the amount of residual stresses did not increase in a linear but rather a logarithmic fashion with the iPS400K content as can be clearly seen in the inset of Fig. 4.25(c) for the mean values of B_v and B_w . The mean values $\overline{B_v}$, $\overline{B_w}$ (for each iPS400K content, we added the obtained values for all 9 dewetting temperatures and divided this sum by 9) are listed in Table 4.1.

iPS400K content (%)	$\overline{B_v}$ ± 0.1	$\overline{B_w}$ ± 0.1
0	2.6	2.4
5	5.0	4.8
10	6.0	5.7
15	7.0	6.8
20	8.1	7.6
25	9.1	8.7
50	10.0	9.7
100	11.1	10.8

Table 4.1: Mean values of $\overline{B_v}$, $\overline{B_w}$ for different iPS400K content

From Fig. 4.23, we observed that the relaxation of residual stresses took more time in pure iPS400K than in pure iPPMS608K films. In order to show how relaxation times vary with increasing content of iPS400K, we present in Figs. 4.26(a) and 4.26(b), the values of τ_v and τ_w , deduced from curves like the ones shown in Fig. 4.23 or Fig. 4.24, as a function of increasing iPS400K content for all measured dewetting temperatures. We noticed that both τ_v and τ_w increased with increasing iPS400K content suggesting that relaxation of residual stresses became slower with increasing iPS400K content. Intriguingly, concomitantly with the relaxation time τ_r also the amount of residual stresses increased with increasing iPS400K content, i.e., the relaxation time increased approximately linearly with increasing amount of

residual stresses (Fig. 4.26(c)). Accordingly, for any given T_{dew} , the ratio of the relaxation times ($\tau_r \in \{\tau_v, \tau_w\}$) relative to the residual stresses ($\tau_r/\sigma_{\text{res}}$) was approximately constant but increased with decrease in T_{dew} (Fig. 4.26(d))

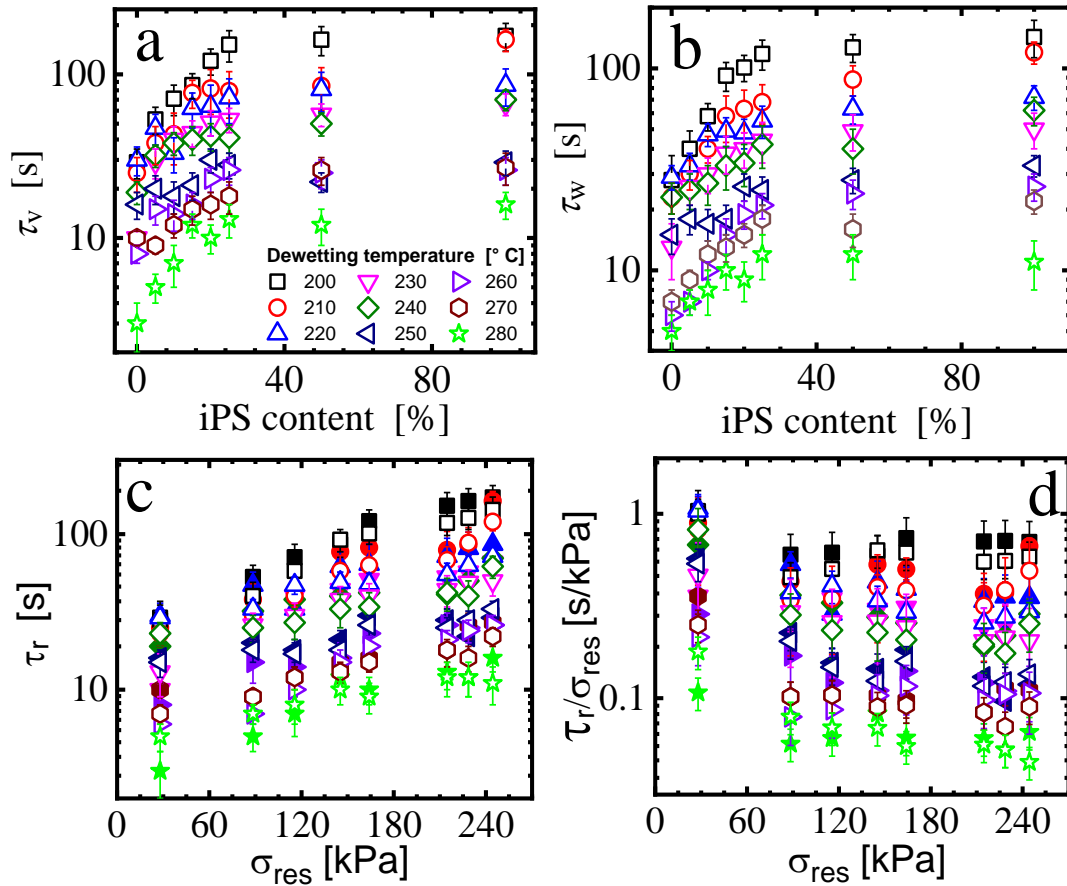


Fig. 4.26: Semi-logarithmic plot of (a) τ_v , (b) τ_w for 200 nm iPpMS608K – iPS400K blend films as a function of iPS400K content. Different symbols and colors indicate different dewetting temperatures T_{dew} (see legend in (a)). Semi-logarithmic plots of (c) relaxation time, $\tau_r \in \{\tau_v, \tau_w\}$ and (d) the ratio $\tau_r/\sigma_{\text{res}}$ as a function of residual stress for all studied dewetting temperatures. Closed symbols in (c) and (d) are for values of τ_v while the open symbols are for values of τ_w .

Next we plot in Fig. 4.27(a) relaxation times $\tau_r \in \{\tau_v, \tau_w\}$ as a function of reciprocal of dewetting temperature, T_{dew}^{-1} . The resulting activation energies are shown in Fig. 4.27(b).

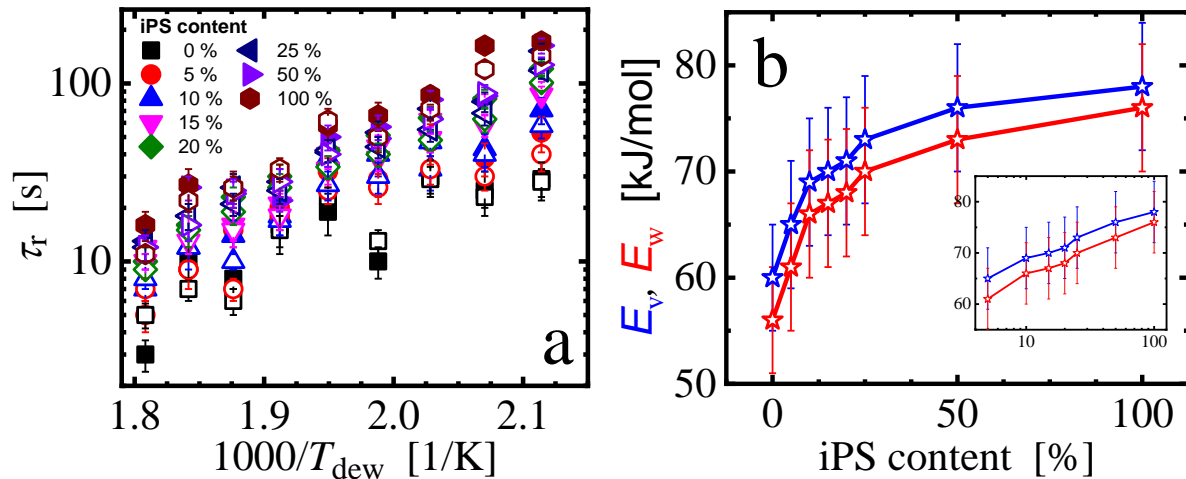


Fig. 4.27: (a) Semi-logarithmic plot of the relaxation time $\tau_r \in \{\tau_v, \tau_w\}$ as a function of $1000/T_{\text{dew}}$ for 200 nm *iPpMS608K* – *iPS400K* blend films for *iPS400K* content ranging from 0 to 100 %, as indicated by the different symbols and colors (see legend). Closed symbols are for τ_v and open symbols are for τ_w . (b) Assuming an Arrhenius-type behaviour of the data in (a), we deduced an activation energy $E_a \in \{E_v, E_w\}$ as a function of *iPS400K* content (represented as blue and red stars for the values E_v and E_w deduced from $\log \tau_v(1000/T_{\text{dew}})$ and $\log \tau_w(1000/T_{\text{dew}})$, respectively). The inset shows the same data points on a logarithmic scale of the *iPS400K* content, suggesting that E_a for the blend films increased with the logarithm of the *iPS400K* content.

In Fig. 4.27(a), on semi-logarithmic scales the relaxation times as a function of $1000/T_{\text{dew}}$ is presented. Each data set suggests an Arrhenius-type behaviour represented by a characteristic activation energy, $E_a \in \{E_v, E_w\}$. Using equation (4.8), the values of E_a were obtained, presented in Fig. 4.27(b) as a function of *iPS400K* content. An increase in activation energy with increasing *iPS400K* content was observed. At first glance, this may seem surprising as the key difference between the two polymers consists in the presence of the nonpolar methyl group on the aromatic ring in *iPpMS608K*. Furthermore, the glass transition temperature (T_g) of *iPS400K* and *iPpMS608K* are rather similar. However, it has been suggested that, due to the formation of transient clusters, flow in *iPS400K* at elevated shear rates requires cooperative movement of a higher number of segments (Chandran, & Reiter, 2016). Thus, the increase in

E_a may be related to an increased tendency for the formation of transient clusters in blends with increased iPS400K content.

As can be seen from equations (4.3) and (4.6), the initial and final velocities, $v_i(t_{\text{inc}} \rightarrow 0)$ and $v_i(t_{\text{inc}} \rightarrow \infty)$ play an important role in characterizing the dewetting dynamics in thin polymer films. For instance, by normalizing dewetting velocity with respect to the limiting dewetting velocity (at long incubation times) for films of various iPS400K content (Fig. 4.24), qualitative similar dewetting characteristics for iPS400K and iPPMS608K films as well as for films of a blend of these polymers were observed. At the same time, the change in dewetting velocity from $t_{\text{inc}} \rightarrow 0$ to $t_{\text{inc}} \rightarrow \infty$ is a manifestation of the pathway towards equilibrium, i.e., can be thought of as a transition from a non-equilibrium state to an equilibrium state reflecting the relaxation process of residual stresses. In this regard, in Fig. 4.28 as a function of $1000/T_{\text{dew}}$ the initial dewetting velocity, $v_i(t_{\text{inc}})$ of the first detected holes and the corresponding asymptotic velocities $v_i(t_{\text{inc}} \rightarrow 0)$, $v_i(t_{\text{inc}} \rightarrow \infty)$ was plotted. It was noted that pure iPPMS608K films, represented by black squares in Figs. 4.28(a) – 4.28(c), are characterized by a change in slope (generating a “kink”) at $T_{\text{dew}} = 220$ °C, already observed for pure iPPMS60K films. As the amount of iPS400K content increased from 0 % to 100 %, this kink disappeared (for iPS400K content ≥ 20 %).

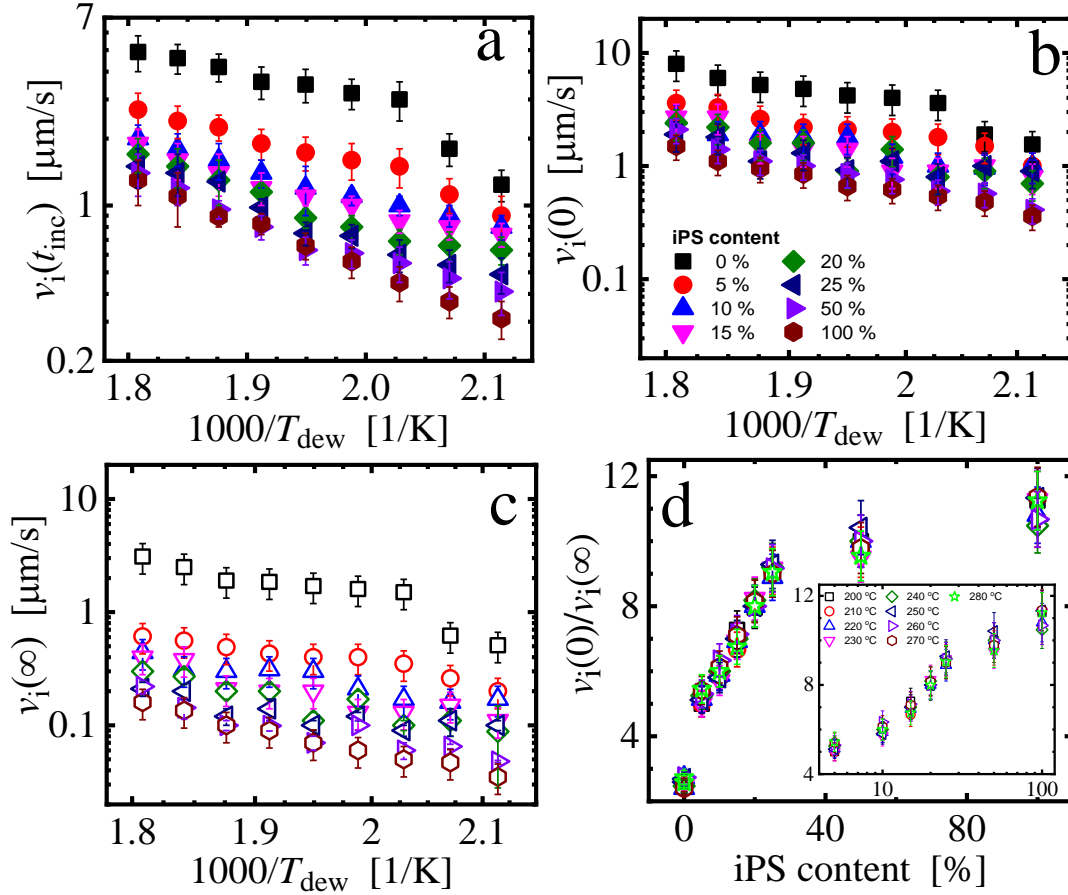


Fig. 4.28: Double logarithmic plot of (a) initial dewetting velocity ($v_i(t_{\text{inc}})$) of the earliest nucleated dewetting holes, (b) and (c) limiting values of $v_i(0)$ and $v_i(\infty)$, respectively, as a function of $1000/T_{\text{dew}}$ for dewetting holes at increasing iPS400K content. Here, $v_i(0) = v_i(t_{\text{inc}} \rightarrow 0)$ and $v_i(\infty) = v_i(t_{\text{inc}} \rightarrow \infty)$. The different symbols and colors indicate different iPS400K content as represented in the legend in (b). (d) Ratio $v_i(0)/v_i(\infty)$ as a function of the iPS400K content for the various values of T_{dew} as indicated in the legend of the inset. The inset shows the same data points on a logarithmic scale of the iPS400K content, suggesting that $v_i(0)/v_i(\infty)$ for the blend films increased with the logarithm of the iPS400K content.

In a purely elastic film, the height of the rim width reaches a maximum height, H_{max} , at the time t_{max} . Assuming linear elasticity (Hooke's law), H_{max} is related to the total driving forces, σ_{tot} , the shear modulus, $G(T_{\text{dew}})$, the maximum strain, ε_{max} , and the film thickness, h_0 , as shown in equation (4.11). As already observed earlier, the maximum strain is derived from the region where the value of $R(t_{\text{dew}})/2w(t_{\text{dew}})$ as a function of $w(t_{\text{dew}})$ became (almost) constant (Fig. 4.29(a)). The obtained values of ε_{max} for films of different iPS400K

content and for dewetting at various temperatures are plotted in Fig. 4.29(b). As a qualitative trend, a decrease in ϵ_{\max} with increasing iPS400K content was observed (Fig. 4.29(b)). With increasing T_{dew} , ϵ_{\max} increased monotonically, the increase being more pronounced for low iPS400K content.

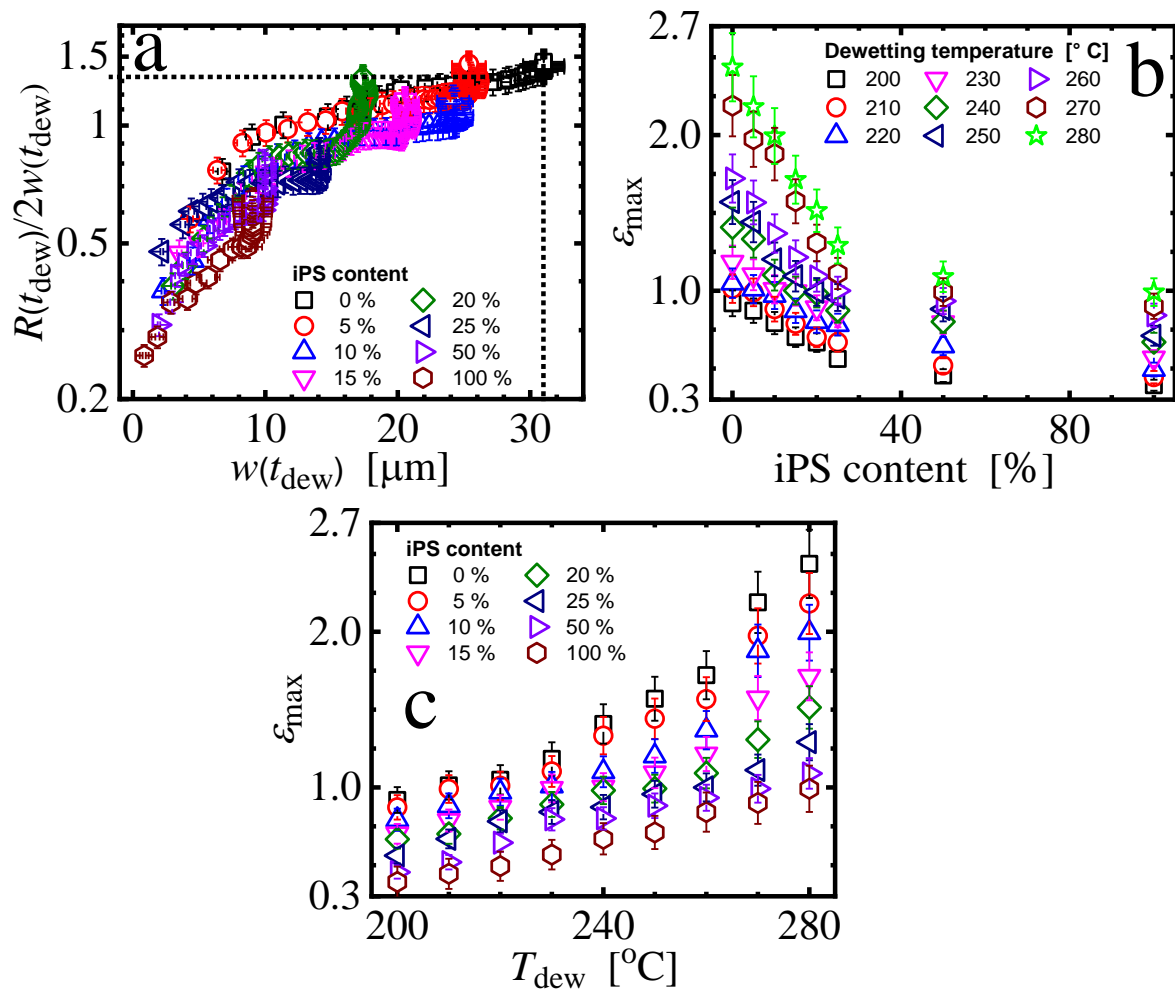


Fig. 4.29: (a) Semi-logarithmic plot of $R(t_{\text{dew}})/2w(t_{\text{dew}})$ as a function of $w(t_{\text{dew}})$ for the earliest nucleated dewetting holes in 200 nm thick spin coated iPpMS608K - iPS400K films at various iPS400K content and at $T_{\text{dew}} = 240$ °C. The black vertical dotted line in (a) is a guide to the eyes indicating the maximum rim width, $w_{\max}(t_{\max})$. The values of ϵ_{\max} are determined at the point where $R(t_{\text{dew}})/2w(t_{\text{dew}})$ becomes almost constant (indicated by the black horizontal dotted line for an iPS400K content of 0 %). In (b) and (c), linear plots of ϵ_{\max} as a function of iPS400K content and T_{dew} , respectively are presented. The meaning of the different symbols and colors is indicated in the legends.

The amounts of capillary stress, σ_{cap} , residual stresses, σ_{res} , and total stress, σ_{tot} (the way how these values were determined is described in Appendix D) are shown in Fig. 4.30(a). Notice that for all studied films, the capillary stress was always lower than the residual stresses. Intriguingly, the amount of residual stresses increased with increasing iPS400K content. Since all films were prepared in the same manner and displayed qualitatively similar dewetting characteristics (confirmed by collapse of all data points in Fig. 4.24), it follows that the increase in residual stresses is related to the amount of iPS400K introduced in the films.

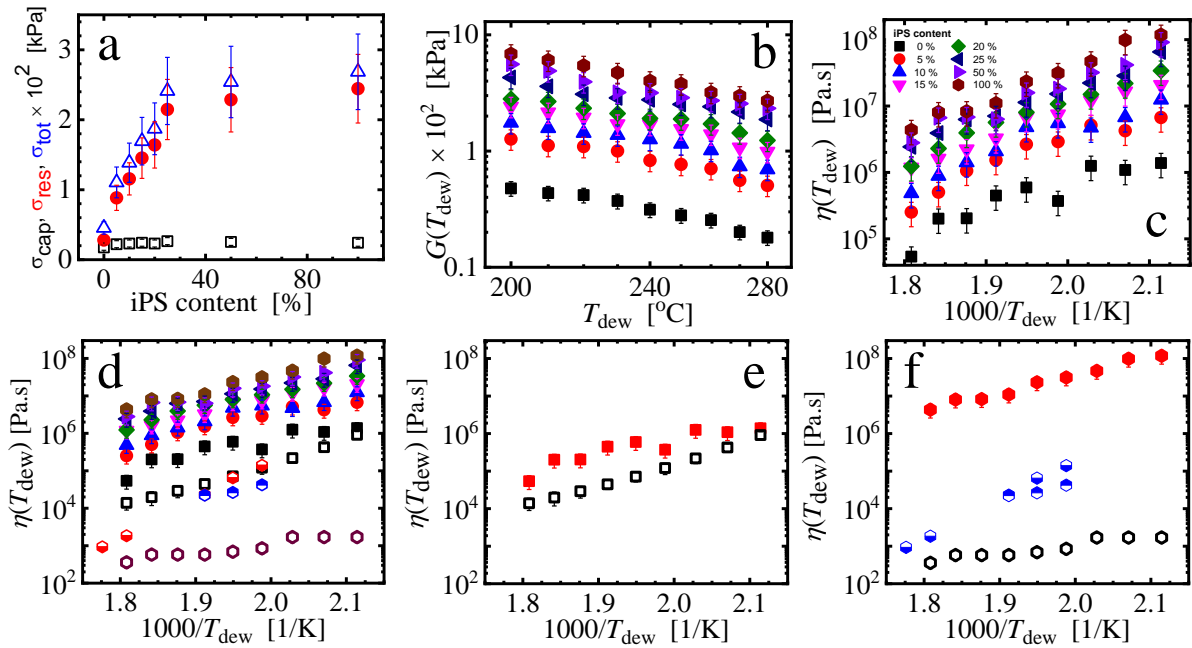


Fig. 4.30: (a) Linear plot of capillary stress (σ_{cap} , black squares), residual stresses (σ_{res} , red circles) and total stress ($\sigma_{\text{tot}} = \sigma_{\text{cap}} + \sigma_{\text{res}}$, blue up triangles) as a function of iPS400K content for the averaged values of B_v from Table 4.1. The derivations of the values of σ_{cap} , σ_{res} and σ_{tot} are found in Appendix D. (b) Logarithmic plot of shear modulus $G(T_{\text{dew}})$ as a function of T_{dew} at different iPS400K content. (c) Semi-logarithmic plot of effective viscosity $\eta_{\text{non-equ}}(T_{\text{dew}})$ as a function of $1000/T_{\text{dew}}$ at different iPS400K content. Different symbols and colors in (b) and (c) are explained in the legend in (c). In (d), the same data as in (c) in comparison with literature values for the zero-shear viscosity $\eta_0(T_{\text{dew}})$ of iPS400K (open hexagons) and iPpMS608K (open squares), respectively. In addition, the shear viscosity values were found from dewetting experiments (Chandran, & Reiter, 2016) on equilibrated iPS400K films (half-filled blue hexagons). In (e) and (f), a comparison between the literature values for the zero-shear viscosity (open symbols) with the values of the viscosity (filled symbols) derived from the present experiments for pure iPS400K and iPpMS608K films, respectively is given. In (f), shear viscosity values found from dewetting experiments (Chandran, & Reiter, 2016) on equilibrated iPS400K films (half-filled hexagons) are shown.

From the dewetting experiments performed at various temperatures and under conditions of a variable driving force (varying total stress), non-equilibrium shear modulus $G(T_{\text{dew}})$ as a function of strain using equations (4.12) and (4.13) was obtained. The results are plotted in Fig. 4.30(b). Based on available literature data for the plateau modulus G_N^0 of iPS400K ($G_N^0 = 156$ kPa) (Huang et al., 2011) and atactic PpMS ($G_N^0 = 145$ kPa) (Kempf, Barroso, & Wilhelm, 2010) the values obtained were comparable. For iPpMS608K, the obtained values compared to the values of $G(T_{\text{dew}})$ were somewhat lower while for iPS400K they were somewhat higher compared to the literature values of the plateau modulus G_N^0 .

The corresponding “non-equilibrium viscosity” is shown in Fig. 4.30(c).

$$\eta_{\text{non-equ}}(T_{\text{dew}}) = G(T_{\text{dew}}) \cdot \tau(T_{\text{dew}}) \quad (4.19)$$

Notice that $\eta_{\text{non-equ}}(T_{\text{dew}})$ increased with increasing iPS400K content. As for the temperature dependence, $\eta_{\text{non-equ}}(T_{\text{dew}})$ followed a kind of Arrhenius behaviour, i.e., $\eta_{\text{non-equ}}(T_{\text{dew}}) = \eta_0 \cdot \exp(E_\eta/k_B T_{\text{dew}})$ (Wang, Shyong, & Porter, 1995) with a characteristic activation energy E_η (energy required to activate flow). Similar to the values of E_a shown in Fig. 4.27(b) derived from the temperature dependence of $\tau_r \in \{\tau_v, \tau_w\}$, the values of E_η were found to increase with increasing iPS400K content as shown in Fig. 4.31.

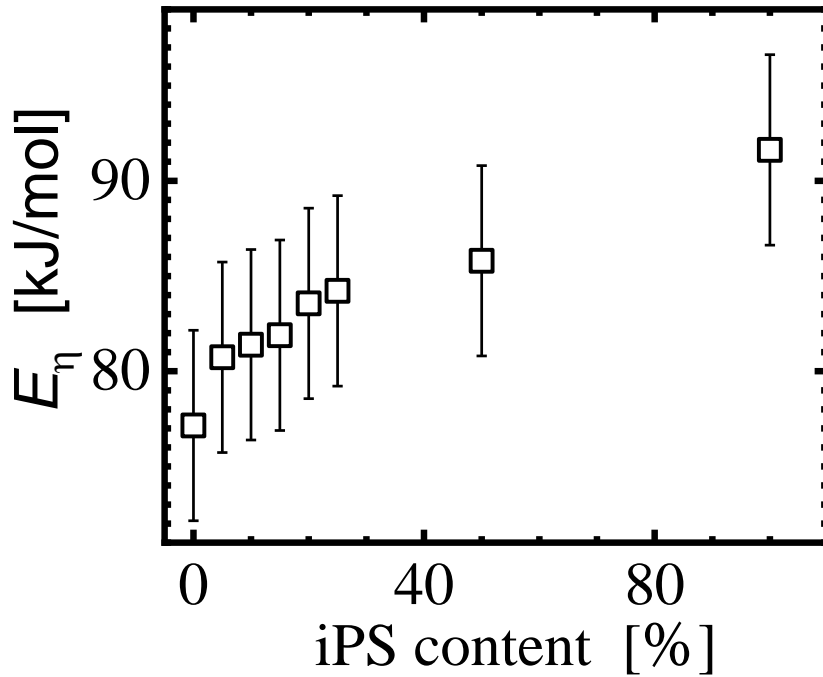


Fig. 4.31: Linear plot of activation energy E_η as a function of iPS400K content.

Using the bulk plateau modulus (G_N^0) and the obtained reptation times (τ_{rep}), the zero-viscosities were calculated from $\eta_0 = G_N^0 \cdot \tau_{\text{rep}}$. Furthermore, the temperature-dependence of τ_{rep} was obtained using the Williams-Landel-Ferry (WLF) (Schluze, Handge, & Abetz, 2017) parameters. As can be seen from a comparison with literature values for the zero-shear viscosity $\eta_0(T_{\text{dew}})$ of iPS400K and iPpMS608K, one can clearly discern differences (see Figs. 4.30(d) – 4.30(f)). While for iPpMS608K the values of $\eta_{\text{non-equ}}(T_{\text{dew}})$ are rather close to the published values of the zero-shear viscosity, the situation is strikingly different for iPS400K. For the freshly prepared films, observed values were about four orders in magnitude higher than literature values for the zero-shear viscosity of iPS400K. Interestingly, as discussed in reference (Chandran, & Reiter, 2016), the shear viscosity of iPS films after long incubation times (equilibrated films) was still higher than $\eta_0(T_{\text{dew}})$. This difference in behaviour of iPpMS608K and iPS400K is correlated with a significantly higher value of the residual stresses

σ_{res} , a higher shear modulus $G(T_{\text{dew}})$ and longer relaxation times $\tau(T_{\text{dew}})$ of iPS400K. Tentatively, this difference might be related to the stronger tendency of iPS400K to form transient clusters of correlated polymer chains, also reflected in an extremely high nucleation density of as-prepared (spin-coated) iPS films, as seen in recent crystallization experiments (Poudel et al., 2018a)

CHAPTER FIVE

CONCLUSIONS AND RECOMMENDATIONS

5.1 Introduction

The study demonstrated and discussed the importance of non-equilibrium conformations in controlling the rheological properties of isotactic poly(*para*-methylstyrene) (iPpMS) and its blend with isotactic polystyrene (iPS400K) with respect to preparation conditions and blending dynamics via dewetting. All the investigated films were prepared through spin-coating technique. In the following sections, conclusions and recommendations for the usability of the material and for further research are given.

5.2 Conclusions

In conclusion, the non-equilibrium states of the iPpMS608K films were systematically carried out by varying the solution concentration (c) ($6 \text{ mg/ml} \leq c \leq 25 \text{ mg/ml}$), spin-coating speed (ω) ($500 \text{ rpm} \leq \omega \leq 12\,000 \text{ rpm}$), dewetting temperature ($T_{\text{dew}} \geq 120 \text{ }^\circ\text{C}$) and iPS400K blending ($0 \% \leq \text{iPS400K} \leq 100 \%$) in order to control their relaxation dynamics. It was shown that a novel dewetting behaviour of thin iPpMS608K films on slippery substrates exhibited two distinctly different stages of dewetting. The early dewetting stage and the late dewetting stage transiting at a point where the rim width had reached a maximum value by relaxation process. At this late dewetting stage, the polymer behaved like a viscous fluid and dewetting was controlled by slippage, which induced a Rayleigh-Plateau-type rim-instability (McGraw et al., 2010) and led to droplet formation. Further, it was observed that the residual stresses of iPpMS608K films did not depend on film thickness alone but also on spin-coating speed. Intriguingly, iPpMS608K films prepared at higher spin-coating speed ($> 2000 \text{ rpm}$) were associated with large number of residual stresses and could relax 8 times faster than films

prepared at low spin-coating speed (≤ 2000 rpm) (less residual stresses). At the same time, *iPpMS608K* films prepared from dilute solutions were associated with more residual stresses and short stress relaxation times when compared to films prepared from high solution concentration.

Since $(\sigma_{\text{res}} + \sigma_{\text{cap}})/\sigma_{\text{cap}}$ did not vary with dewetting temperature, then it means the amount of residual stresses did not depend on temperature and did not have a chance to change and thus should depend solely on how the films were prepared or aged. The decrease in the deduced modulus with increasing dewetting temperature of *iPpMS608K* films might be a manifestation of the non-equilibrium chain conformations of spin-coated polymers (Chandran et al., 2017; Sharma, & Reiter, 1996). Observing a (slightly) temperature dependent elastic modulus might be related to the same causes which are responsible for deviations in relaxation times and activation energies from the corresponding values of equilibrated polymer melts (Chandran, & Reiter, 2016).

The amount of residual stress did not vary with dewetting temperature even after introducing *iPS400K* in *iPpMS608K* matrix, implying that dewetting was so fast that possible phase separation did not occur during dewetting. It was observed that presence of *iPS400K* in *iPpMS608K* system led to increase in amount of residual stresses, relaxation times and corresponding activation energy, possibly due to an increased tendency for the formation of transient clusters in blends with increased *iPS400K* content. These transient clusters may require cooperative movement of a higher number of segments. In other words, it is possible to tune the rheological properties of *iPpMS608K* system through blending. The observed difference in non-equilibrium viscosity between *iPpMS608K* and *iPS400K* was correlated with a significantly higher residual stress, a higher non-equilibrium shear modulus and longer relaxation time of *iPS400K*. Deduced activation energies from the temperature dependence of

various characteristic times (stress relaxation times, surface relaxation time and the time characterizing the adsorption of polymers) can be less than the activation energies observed for equilibrated melts (Majumder et al., 2018; Poudel et al., 2018a). The activation energy deduced from temperature – dependence viscosity of 200 nm *iPpMS608K* was 83 ± 10 kJ/mol compared to the bulk value of 100 ± 10 kJ/mol. In comparison to *iPS400K*, *iPpMS608K* exhibited reduced energy barrier for flow indicating that the transient clusters of monomers could have a short lifetime in *iPpMS608K*. It is believed that the observed difference might be related to the stronger tendency of *iPS400K* to form transient clusters of correlated polymer chains. Thus, the here presented study demonstrates clearly that systematic dewetting experiments provide a convenient and simple approach for a quantitative determination of rheological properties of thin polymer films.

Dewetting process in *iPpMS608K* and its blend with *iPS400K* has led to production of some simple patterns such as strips and fingers (ordered or disordered). Patterning by dewetting has been proved to be an efficient and economic way to fabricate large area, ordered structures for both scientific investigation and industrial needs.

5.3 Recommendations

5.3.1 Recommendations based on the study

The demand for development of new technologies where miniaturization is required has led to innovative studies into polymer materials at nanometer scale. However, material structures or devices at such a scale are always trapped in non-equilibrium conformation states. Residual stress in polymer materials if left unchecked can severely reduce materials' performance and reliability by inducing mechanical instabilities or increase the defect formation or complete interfacial failure. The study investigated and measured the amount of residual stresses in

iPpMS608K films and its blend with iPS400K. Consequently, the residual stresses in iPpMS608K can be monitored and controlled by being very keen with preparation parameters. Additionally, the residual stresses can be enhanced through blending with other polymers of high residual stresses like isotactic polystyrene.

Basing on results of the study, it is now possible to control residual stress in iPpMS608K films by varying solution concentration and spin-coating speed. The residual stresses were found to decrease with increase in solution concentration or with decrease in spin-coating speed. In quantifying the amount of residual stress in these films, it was found that the residual stress gradually decreases with increasing annealing time. Further, blending iPpMS608K with iPS400K led to increase in the amount of residual stress in iPpMS608K by 5 orders of magnitude. Consequently, the understanding and control of residual stress could lead to improved optimization and performance of iPpMS608K polymer film coatings useful in nanoscale device applications such as sensors.

Controlled dewetting technique of iPpMS608K under varied preparation conditions, and the tunability of the iPpMS608K through blending, can in general be recommended for production of inkjet printing applications such as printable optical elements where the Rayleigh-Plateau instability is desired. Since some patterns generated by dewetting can hardly be achieved by other techniques like lithography, they can be used as original molds to reproduce the pattern or to produce even more complex patterns combined with some functional materials, functional structures and even in nanophotonics where pattern formation (similar to dewetting patterns) is involved. As most of the dewetting patterns produced by dewetting are on the order of microns, which is the right length scale for cell, the patterns can be used as biosensor chips, scaffolds for cell organization and some other bio-techniques. The stress relaxation analysis

done showed that polymeric samples can be tested at a strain value maintained constant for a defined time period especially in dynamical-mechanical characterization of polymer biomaterials which allows studying the viscoelastic behaviour of polymer materials. Keeping in mind that usually, in biomedical applications, the material is subjected to the same mechanical pattern at different times, it should be useful to test samples for more than once. Lastly, faster relaxation of *iPpMS608K* polymers would interest industries as this method can save them processing time by a significant factor.

5.3.2 Recommendations for further studies

The dewetting dynamics in *iPpMS608K* was characterized by a transition at $T_{dew} \geq 220$ °C where the initial dewetting velocity increased at a slow pace (accelerated at a decelerating rate). What could be the reason(s) for the observation? What kind of non-equilibrium experiments can be set up to consider the properties of the system at $T_{dew} \geq 220$ °C? The residual stresses in *iPS400K* were a factor of 5 more than those for *iPpMS608K* films. In addition, the zero-shear viscosity of *iPS400K* at equilibrium was found to be less than that of *iPpMS608K*. Why is it then that *iPpMS608K* still dewetted faster than *iPS400K*? What could be the molecular reasons behind the deviations and the compositional heterogeneities that can be observed for thin *iPpMS608K* - *iPS400K* blend films?

The surface of the polymer film is described as a frozen-in liquid. After annealing above the glass transition temperature in case of stable polymer films, the surface roughness spectrum is changed and dominated by the Van der Waals interaction. Can roughness correlation above entanglement weight have any effect on the relaxation dynamics of *iPpMS608K* films and its blend with *iPS400K*? What happens in case of floated *iPpMS608K* films on *iPS400K* films? What could be the role of substrate on the rate of stress relaxation of *iPpMS608K* films?

REFERENCES

- Al Akhrass, S., Reiter, G., Hou, S. Y., Yang, M. H., Chang, Y. L., Chang, F. C., Wang, C. F., & Yang, A. C. M. (2008). Viscoelastic Thin Polymer Films under Transient Residual Stresses: Two-Stage Dewetting on Soft Substrates. *Physical Review Letters*, *100*, 178301. <https://doi.org/10.1103/PhysRevLett.100.178301>
- Atwater, H. A., & Polman, A. (2010). Plasmonics for Improved Photovoltaic Devices. *Nature Materials*, *9*(3), 205 – 213. <https://doi.org/10.1038/nmat2629>
- Bäumchen, O., Fetzer, R., Klos, M., Lessel, M., Marquant, L., Hähl, H. & Jacobs, K. (2012). Slippage and Nanorheology of Thin Liquid Polymer Films. *J. Phys.: Condens. Matter*, *24*, 325102. <https://doi.org/10.1088/0953-8984/24/32/325102>
- Bäumchen, O., & Jacobs, K. (2010). Slip Effects in Polymer Thin Films. *Journal of Physics: Condensed Matter*, *22*(3), 033101. <https://doi.org/10.1088/0953-8984/22/3/033101>
- Blossey, R. (2012). *Thin Liquid Films: Dewetting and Polymer Flow*. Springer Verlag: Germany. <https://doi.org/10.1017/CBO9781107415324.004>
- Blossey, R., Münch, A., Rauscher, M., & Wagner, B. (2006). Slip vs. Viscoelasticity in Dewetting Thin Films. *European Physical Journal E*, *20*, 267 – 271. <https://doi.org/10.1140/epje/i2006-10018-0>
- Bodiguel, H. & Fretigny, C. (2006). Viscoelastic Dewetting of a Polymer Film on a Liquid Substrate. *Eur. Phys. J. E*, *19*, 2, 185 - 193. <https://doi.org/10.1140/epje/e2006-00021-8>
- Boschetti-de-Fierro, A., Spindler, L., Reiter, G., Olmos, D., Magonov, S., & Abetz, V. (2007). Thin Film Morphology in Triblock Terpolymers with One and Two Crystallizable Blocks. *Macromolecules*, *40*(15), 5487 – 5496. <https://doi.org/10.1021/ma0703812>
- Bower, D. I. (2003). *An Introduction to Polymer Physics*. Cambridge University Press: New York. <https://doi.org/10.1119/1.1533063>.
- Boyd, R. H. & Smith, G. D. (2007). *Polymer Dynamics and Relaxation*. Cambridge University Press: New York. <https://www.amazon.com/Polymer-Dynamics-Relaxation-Richard-Boyd/dp/0521814197>
- Brochard-Wyart, F., Debregeas, G., Fondcave, R., & Martin, P. (1997). Dewetting of Supported Viscoelastic Polymer Films: Birth of Rims. *Macromolecules*, *30*(24), 1211 – 1213. <https://doi.org/10.1021/ma960929x>
- Brochard-Wyart, F., & de Gennes, P. -G. (2003). *Dynamics of Partial Wetting. Series in Condensed Matter*, 417 – 430. https://doi.org/10.1142/9789812564849_0045
- Brochard-Wyart, F., de Gennes, P. -G., Hervet, H., & Redon, C. (1994). Wetting and Slippage of Polymer Melts on Semi-Ideal Surfaces. *Langmuir*, *10*(5), 1566-1572. <https://doi.org/10.1021/la00017a040>

- Brochard-Wyart, F., Martin, P., & Redon, C. (1993). Liquid/Liquid Dewetting. *Langmuir*, 9 (12), 3682-3690. <https://doi.org/10.1021/la00036a053>
- Callaghan, T. A., & Paul, D. R. (1993). Interaction Energies for Blends of Poly(methyl methacrylate), Polystyrene, and Poly(α -methylstyrene) by the Critical Molecular Weight Method. *Macromolecules*, 26, 2439 - 2450. <https://doi.org/10.1021/ma00062a008>
- Chandran, S., Baschnagel, J., Cangialosi, D., Fukao, K., Glynos, E., Janssen, L. M. C., Müller, M., Muthukumar, M., Steiner, U., Xu, J., Napolitano, S., & Reiter, G. (2019). Processing Pathways Decide Polymer Properties at the Molecular Level. In *Macromolecules*, 52(19), 7146–7156. <https://doi.org/10.1021/acs.macromol.9b01195>
- Chandran, S., Dold, S., Buvignier, A., Krannig, K. S., Schlaad, H., Reiter, G., & Reiter, R. (2015). Tuning Morphologies of Langmuir Polymer Films Through Controlled Relaxations of Non-Equilibrium States. *Langmuir*, 31(23), 6426–6435. <https://doi.org/10.1021/acs.langmuir.5b01212>
- Chandran, S., Handa, R., Kchaou, M., al Akhrass, S., Semenov, A. N., & Reiter, G. (2017). Time Allowed for Equilibration Quantifies the Preparation Induced Nonequilibrium Behaviour of Polymer Films. *ACS Macro Letters*, 6, 1296 - 1300. <https://doi.org/10.1021/acsmacrolett.7b00815>
- Chandran, S., & Reiter, G. (2016). Transient Cooperative Processes in Dewetting Polymer Melts. *Physical Review Letters*, 2016, 116, 088301. <https://doi.org/10.1103/PhysRevLett.116.088301>
- Chandran, S., & Reiter, G. (2019). Segmental Rearrangements Relax Stresses in Nonequilibrated Polymer Films. *ACS Macro Letters*, 8, 646 - 650. <https://doi.org/10.1021/acsmacrolett.9b00116>
- Chang, L. L., & Woo, E. M. (2003a). Surface Morphology and Flory-Huggins Interaction Strength in UCST Blend System Comprising Poly(4-methyl styrene) and Isotactic Polystyrene. *Polymer*, 44(5), 1711 - 1719. [https://doi.org/10.1016/S0032-3861\(02\)00915-1](https://doi.org/10.1016/S0032-3861(02)00915-1)
- Chang, L. L., & Woo, E. M. (2003b). UCST Behaviour in Blend Systems of Isotactic Polystyrene/Poly(4-methyl styrene) in Comparison with Atactic Polystyrene/Poly(4-methyl styrene). *Colloid and Polymer Science*, 281, 1147 - 1156. <https://doi.org/10.1007/s00396-003-0890-5>
- Chang, L. L., Woo, E. M., & Liu, H. L. (2004). Criteria Dilemma of Phase Behaviour in Ternary Blends Comprising Polystyrene, Poly(α -methylstyrene), and Poly(4-methylstyrene). *Polymer*, 45, 6909 - 6918. <https://doi.org/10.1016/j.polymer.2004.07.058>
- Cho, K. S., Rubinstein, M., & Colby, R. H. (2003). *Polymer Physics*. Springer Verlag: Germany. <https://doi.org/10.1002/pi.1472>
- Chowdhury, M., Freyberg, P., Ziebert, F., Yang, A. C. M., Steiner, U., & Reiter, G. (2012). Segmental Relaxations have Macroscopic Consequences in Glassy Polymer Films. *Physical Review Letters*, 109, 136102. <https://doi.org/10.1103/PhysRevLett.109.136102>

- Chowdhury, M., Sheng, X., Ziebert, F., Yang, A. C. M., Sepe, A., Steiner, U., & Reiter, G. (2016). Intrinsic Stresses in Thin Glassy Polymer Films Revealed by Crack Formation. *Macromolecules*, 49(23), 9060–9067. <https://doi.org/10.1021/acs.macromol.6b01640>
- Christensen, R. M., & Freund, L. B. (2010). *Theory of Viscoelasticity*. Academic Press: New York. <https://doi.org/10.1115/1.3408900>
- Chung, J. Y., Chastek, T. Q., Fasolka, M. J., Ro, H. W., & Stafford, C. M. (2009). Quantifying Residual Stress in Nanoscale Thin Polymer Films via Surface Wrinkling. *ACS Nano.*, 3, 844–852. <https://doi.org/10.1021/nn800853y>
- Colmenero, J., & Arbe, A. (2007). Segmental Dynamics in Miscible Polymer Blends: Recent Results and Open Questions. *Soft Matter*, 3, 1474 - 1485. <https://doi.org/10.1039/b710141d>
- Damman, P., Gabriele, S., Coppée, S., Desprez, S., Villers, D., Vilmin, T., Raphaël, E., Hamieh, M., Akhrass, S. al, & Reiter, G. (2007). Relaxation of Residual Stress and Reentanglement of Polymers in Spin-Coated Films. *Physical Review Letters*, 91(21), 216101. <https://doi.org/10.1103/PhysRevLett.99.036101>
- de Gennes, P. -G. (1990). *Introduction to Polymer Dynamics*. Cambridge University Press: New York.
- de Gennes, P.-G., Brochard-Wyart, F., & Quéré, D. (2004). *Capillarity and Wetting Phenomena*. Cambridge University Press: Sydney. <https://doi.org/10.1007/978-0-387-21656-0>
- de Gennes, P. -G., & Deutsch, J. M. (1991). Introduction to Polymer Dynamics. *Physics Today*, 44(10), 113. <https://doi.org/10.1063/1.2810290>
- Ferry, J. D. (1980). *Viscoelastic Properties of Polymers*. Third Edition; John Wiley & Sons: Singapore.
- Fetters, L. J., Lohse, D. J., & Graessley, W. W. (1999). Chain Dimensions and Entanglement Spacing in Dense Macromolecular Systems. *Journal of Polymer Science, Part B: Polymer Physics*, 37, 1023 - 1033. [https://doi.org/10.1002/\(SICI\)1099-0488\(19990515\)37:10<1023::AID-POLB7>3.0.CO;2-T](https://doi.org/10.1002/(SICI)1099-0488(19990515)37:10<1023::AID-POLB7>3.0.CO;2-T)
- Fleming, R. J., & Bower, D. I. (2003). An Introduction to Polymer Physics. *American Journal of Physics*, 71(3), 285-290. <https://doi.org/10.1119/1.1533063>
- Flory, P. J. (1942). Thermodynamics of High Polymer Solutions. *Journal of Chemical Physics*, 10, 51–61. <https://doi.org/10.1063/1.1723621>
- Forrest, J. A., & Dalnoki-Veress, K. (2001). The Glass Transition in Thin Polymer Films. *Advances in Colloid and Interface Science* 94(1-3), 167-195. [https://doi.org/10.1016/S0001-8686\(01\)00060-4](https://doi.org/10.1016/S0001-8686(01)00060-4)
- Gabriele, S., Damman, P., Sclavons, S., Desprez, S., Coppée, S., Reiter, G., Hamieh, M., al Akhrass, S., Vilmin, T., & Raphaël, E. (2006). Viscoelastic Dewetting of Constrained

- Polymer Thin Films. *Journal of Polymer Science, Part B: Polymer Physics*, 44, 20, 3022 – 3030. <https://doi.org/10.1002/polb.20919>
- Gabriele, S., Sclavons, S., Reiter, G., & Damman, P. (2006). Disentanglement Time of Polymers Determines the Onset of Rim Instabilities in Dewetting. *Physical Review Letters*, 96(15), 156105. <https://doi.org/10.1103/PhysRevLett.96.156105>
- Gentili, D., Foschi, G., Valle, F., Cavallini, M., & Biscarini, F. (2012). Applications of Dewetting in Micro and Nanotechnology. *Chemical Society Reviews*, 41, 4430-4443. <https://doi.org/10.1039/c2cs35040h>
- Glück, A. (2016). *Dewetting Thin Films: Experiments with iPpMS Examining the Influence of Temperature, Film Thickness and Pre-Heating*. Bachelor Thesis, Albert-Ludwigs Universität Freiburg, Germany.
- Gunesin, B., & Gustafson, R. J. (1989). Melting Point Determination of Isotactic Poly(p-methylstyrene). *Journal of Polymer Science Part A: Polymer Chemistry*, 27, 4439 – 4440. <https://doi.org/10.1002/pola.1989.080271322>
- Gupta, T. D., Martin-Monier, L., Yan, W., Bris, A. L., Nguyen-Dang, T., Page, A. G., Ho, K. – T., Yesilkoey, F., Altug, H., Qu, Y., & Sorin, F. (2019). Self-Assembly of Nanostructured Glass Metasurfaces via Templated Fluid Instabilities. *Nature Nanotechnology*, 14, 320–327. <https://doi.org/10.1038/s41565-019-0362-9>
- Hamieh, M., al Akhrass, S., Hamieh, T., Damman, P., Gabriele, S., Vilmin, T., Raphaël, E., & Reiter, G. (2007). Influence of Substrate Properties on the Dewetting Dynamics of Viscoelastic Polymer Films. *Journal of Adhesion*, 367-381. <https://doi.org/10.1080/00218460701282497>
- Harismiadis, V. I., van Bergen, A. R. D., Saraiva, A., Kontogeorgis, G. M., Fredenslund, A., & Tassios, D. P. (1996). Miscibility of Polymer Blends with Engineering Models. *AIChE Journal*, 42(11), 3170 - 3180. <https://doi.org/10.1002/aic.690421117>
- Huang, C. L., Chen, Y. C., Hsiao, T. J., Tsai, J. C., & Wang, C. (2011). Effect of Tacticity on Viscoelastic Properties of Polystyrene. *Macromolecules*, 44, 6155 – 6161. <https://doi.org/10.1021/ma200695c>
- Kanaya, T. (2013). Glass Transition, Dynamics and Heterogeneity of Polymer Thin Films Preface. In T. Kanaya (Ed.), *Glass Transition, Dynamics and Heterogeneity of Polymer Thin Films* (Vol. 252, pp. V–VI). Springer-Verlag: Germany. <https://doi.org/10.1007/978-3-642-34339-1>
- Karasz, F. E., Bair, H. E., & O'Reilly, J. M. (1965). Thermal Properties of Atactic and Isotactic Polystyrene. *Journal of Physical Chemistry*, 69, 8, 2657 - 2667. <https://doi.org/10.1021/j100892a030>
- Kchaou, M., Alcouffe, P., Chandran, S., Cassagnau, P., Reiter, G., & al Akhrass, S. (2018). Tuning Relaxation Dynamics and Mechanical Properties of Polymer Films of Identical Thickness. *Physical Review E*, 97, 032507. <https://doi.org/10.1103/PhysRevE.97.032507>

- Kempf, M., Barroso, V. C., & Wilhelm, M. (2010). Anionic Synthesis and Rheological Characterization of Poly(*p*-methylstyrene) Model Comb Architectures with a Defined and Very Low Degree of Long-Chain Branching. *Macromol. Rapid Commun.*, *31*, 2140 – 2145. <https://doi.org/10.1002/marc.201000412>
- Kempf, M., Ahirwal, D., Cziep, M., & Wilhelm, M. (2013). Synthesis and Linear and Nonlinear Melt Rheology of Well-Defined Comb Architectures of PS and PpMS with a Low and Controlled Degree of Long-Chain Branching. *Macromolecules*, *46*, 4978 - 4994. <https://doi.org/10.1021/ma302033g>
- Koenderink, A. F., Alù, A., & Polman, A. (2015). Nanophotonics: Shrinking Light-Based Technology. *American Association for the Advancement of Science*, *348*(6234), 516 - 521. <https://doi.org/10.1126/science.1261243>
- Kojio, K., Kiyoshima, Y., Kajiwara, T., Higaki, Y., Sue, H. J., & Takahara, A. (2019). Effect of Blend Composition on Scratch Behaviour of Polystyrene/Poly(2,6-dimethyl-1,4-phenyleneoxide) Blends. *Macromolecular Chemistry and Physics*, *1800371*, 1 – 6. <https://doi.org/10.1002/macp.201800371>
- Li, B. T., Wu, Y. X., Cheng, H., & Liu, W. H. (2012). Synthesis of Linear Isotactic-Rich Poly(*p*-methylstyrene) via Cationic Polymerization Co-initiated with AlCl₃. *Polymer*, *53*(17), 3726 – 3734. <https://doi.org/10.1016/j.polymer.2012.04.003>
- Li, S. H. & Woo, E. M. (2006). Miscibility in Blends of Isotactic/Syndiotactic Polystyrenes at Melt or Quenched Amorphous. *Macromol. Mater. Eng.*, *291*(11), 1397 - 1406. <https://doi.org/10.1002/mame.200600240>
- Macosko, C. W., Guégan, P., Khandpur, A. K., Nakayama, A., Marechal, P., & Inoue, T. (1996). Compatibilizers for Melt Blending: Premade Block Copolymers. *Macromolecules*, *29*(17), 5590 - 5598. <https://doi.org/10.1021/ma9602482>
- Mainardi, F., & Spada, G. (2011). Creep, Relaxation and Viscosity Properties for Basic Fractional Models in Rheology. *The European Physics Journal: Special Topics*, *193*, 133 – 160. <https://doi.org/10.1140/epjst/e2011-01387-1>
- Majumder, S., Busch, H., Poudel, P., Mecking, S., & Reiter, G. (2018). Growth Kinetics of Stacks of Lamellar Polymer Crystals. *Macromolecules*, *51*(21), 8738–8745. <https://doi.org/10.1021/acs.macromol.8b01765>
- Makhlouf, A. S. H. (2014). Handbook of Smart Coatings for Materials Protection. In *Handbook of Smart Coatings for Materials Protection*. Elsevier: Germany. <https://doi.org/10.1533/9780857096883>
- Malhotra, S. L., Lessard, P., Minh, L., & Blanc Hard, L. P. (1980). Thermal Decomposition and Glass-Transition Temperature Study of Poly-*p*-methylstyrene. *Journal of Macromolecular Science: Part A: Chemistry*, *A14*(4), 517 – 540. <https://doi.org/10.1080/00222338008081033>

- Manfredi, C., Guerra, G., de Rosa, C., Busico, V., & Corradini, P. (1995). Effects of *p*-Methylstyrene Comonomeric Units on the Polymorphic Behaviour of Syndiotactic Polystyrene. *Macromolecules*, 28, 6508 - 6515. <https://doi.org/10.1021/ma00123a017>
- Marquant, L. (2013). *Rim Instability in Dewetting of Thin Polymer Films*. PhD dissertation, University of Saarlandes, Saarbrücken, Germany. <https://doi.org/10.22028/D291-23050>
- McGraw, J. D., Bäumchen, O., Klos, M., Haefner, S., Lessel, M., Backes, S., & Jacobs, K. (2014). Nanofluidics of Thin Polymer Films: Linking the Slip Boundary Condition at Solid-Liquid Interfaces to Macroscopic Pattern Formation and Microscopic Interfacial Properties. *Advances in Colloid and Interface Science*, 210, 13 – 20. <https://doi.org/10.1016/j.cis.2014.03.010>
- McGraw, J. D., Jago, N. M., Dalnoki-Veress, K. (2011). Capillary Levelling as a Probe of Thin Film Polymer Rheology. *Soft Matter*, 7, 7832–7838. <https://doi.org/10.1039/C1SM05261F>
- McGraw, J. D., Li, J., Tran, D. L., Shi, A. C., & Dalnoki-Veress, K. (2010). Plateau-Rayleigh Instability in a Torus: Formation and Breakup of a Polymer Ring. *Soft Matter*, 6, 1258-1262. <https://doi.org/10.1039/b919630g>
- McGraw, J. D., Niguès, A., Chennevière, A., & Siria, A. (2017). Contact Dependence and Velocity Crossover in Friction between Microscopic Solid/Solid Contacts. *Nano Letters*, 17(10), 6335–6339. <https://doi.org/10.1021/acs.nanolett.7b03076>
- Mitov, Z., & Kumacheva, E. (1998). Convection-Induced Patterns in Phase Separating Polymeric Fluids. *Phys. Rev. Lett.*, 81, 3427 – 3430. <https://doi.org/10.1103/PhysRevLett.81.3427>
- Müller-Buschbaum, P. (2003). Dewetting and Pattern Formation in Thin Polymer Films as Investigated in Real and Reciprocal Space. *Journal of Physics Condensed Matter*, 15, R1549–R1582. <https://doi.org/10.1088/0953-8984/15/36/201>
- Müller-Buschbaum, P., Gutmann, J. S., & Stamm, M. (2000). Influence of Blend Composition on Phase Separation and Dewetting of Thin Polymer Blend Films. *Macromolecules*, 33, 4886 - 4895. <https://doi.org/10.1021/ma991073>
- Müller-Buschbaum, P., O'Neill, S. A., Affrossman, S., & Stamm, M. (1998). Phase Separation and Dewetting of Weakly Incompatible Polymer Blend Films. *Macromolecules*, 31, 5003 - 5009. <https://doi.org/10.1021/ma971802q>
- Negash, S., Tatek, Y. B., & Tsige, M. (2018). Effect of Tacticity on the Structure and Glass Transition Temperature of Polystyrene Adsorbed onto Solid Surfaces. *Journal of Chemical Physics*, 148, 134705. <https://doi.org/10.1063/1.5010276>
- Nies, E., & Stroeks, A. (1990). A Modified Hole Theory of Polymeric Fluids. 1. Equation of State of Pure Components. *Macromolecules*, 23(18), 4088–4092. <https://doi.org/10.1021/ma00220a010>
- Okada, T. (1979). Carbon-13 Relaxation of Methyl Derivatives of Polystyrene in Solution. *Polymer Journal*, 11(11), 843 - 848. <https://doi.org/10.1295/polymj.11.843>

- Osswald, T., & Rudolph, N. (2015). *Polymer Rheology: Fundamentals and Applications*. Hanser Publications: Munich.
- Peschka, D., Haefner, S., Marquant, L., Jacobs, K., Münch, A., & Wagner, B. (2019). Signatures of Slip in Dewetting Polymer Films. *Proceedings of the National Academy of Sciences*, *116*(19), 9275 – 9284. <https://doi.org/10.1073/pnas.1820487116>
- Plans, J., MacKnight, W. J. & Karasz, F. E. (1984). Equilibrium Melting Point Depression for Blends of Isotactic Polystyrene with Poly(2, 6-dimethylphenylene oxide). *Macromolecules*, *17*, 810 - 814. <https://doi.org/10.1021/ma00134a048>
- Poudel, P., Chandran, S., Majumder, S., & Reiter, G. (2018a). Controlling Polymer Crystallization Kinetics by Sample History. *Macromolecular Chemistry and Physics*, *219*(3), 1700325. <https://doi.org/10.1002/macp.201700315>
- Poudel, P., Majumder, S., Chandran, S., Zhang, H., & Reiter, G. (2018b). Formation of Periodically Modulated Polymer Crystals. *Macromolecules*, *51*(15), 6119 –6126. <https://doi.org/10.1021/acs.macromol.8b01366>
- Raegen, A., Chowdhury, M., Calers, C., Schmatulla, A., Steiner, U., & Reiter, G. (2010). Aging of Thin Polymer Films Cast from a Near-Theta Solvent. *Physical Review Letters*, *105*, 227801. <https://doi.org/10.1103/PhysRevLett.105.227801>
- Rauscher, M., Münch, A., Wagner, B., & Blossey, R. (2005). A Thin-Film Equation for Viscoelastic Liquids of Jeffreys Type. *European Physical Journal E*, *17*, 373 – 379. <https://doi.org/10.1140/epje/i2005-10016-8>
- Redon, C., Brochard-Wyart, F., & Rondelez, F. (1991). Dynamics of Dewetting. *Colloids and Surfaces A: Physicochemical and Engineering Aspects*, *66*(6), 715 - 718. <https://doi.org/10.1103/PhysRevLett.66.715>
- Reiter, G. (1993). Unstable Thin Polymer Films: Rupture and Dewetting Processes. *Langmuir*, *9* (5), 1344 - 1351. <https://doi.org/10.1021/la00029a031>
- Reiter, G. (1994). Dewetting as a Probe of Polymer Mobility in Thin Films. *Macromolecules*, *27*(11), 3046 - 3052. <https://doi.org/10.1021/ma00089a023>
- Reiter, G. (2005). Evolution of Rim Instabilities in the Dewetting of Slipping Thin Polymer Films. *Journal of Adhesion*, 381 - 395. <https://doi.org/10.1080/00218460590944747>
- Reiter, G. (2013). Probing Properties of Polymers in Thin Films via Dewetting. *Advances in Polymer Science*, *252*, 29 – 64. https://doi.org/10.1007/12_2012_174
- Reiter, G. (2020). The Memorizing Capacity of Polymers. *Journal of Chemical Physics*, *152*(15), 150901. <https://doi.org/10.1063/1.5139621>
- Reiter, G., Al Akhrass, S., Hamieh, M., Damman, P., Gabriele, S., Vilmin, T., & Raphael, E. (2009). Dewetting as an Investigative Tool for Studying Properties of Thin Polymer Films. *Eur. Phys. J. Spec. Top.*, *166*, 165 - 172. <https://doi.org/10.1140/epjst/e2009-00900-5>

- Reiter, G., Castelein, G., & Sommer, J.-U. (2003). Crystallization of Polymers in Thin Films: Model Experiments. In *Polymer Crystallization*. Springer-Verlag: Germany. https://doi.org/10.1007/3-540-45851-4_8
- Reiter, G., Hamieh, M., Damman, P., Sclavons, S., Gabriele, S., Vilmin, T., & Raphaël, E. (2005). Residual Stresses in Thin Polymer Films Cause Rupture and Dominate Early Stages of Dewetting. *Nature Materials*, 4, 754 - 758. <https://doi.org/10.1038/nmat1484>
- Reiter, G., Khanna, R., & Sharma, A. (2003). Self-Destruction and Dewetting of Thin Polymer Films: The Role of Interfacial Tensions. *Journal of Physics Condensed Matter*, 15 S331 – S335. <https://doi.org/10.1088/0953-8984/15/1/345>
- Reiter, G., & Tikhomirov, G. (2001). Dewetting of Highly Elastic Thin Polymer Films. *Physical Review Letters*, 87, 186101. <https://doi.org/10.1103/physrevlett.87.186101>
- Röttele, A., Thurn-Albrecht, T., Sommer, J. U., & Reiter, G. (2003). Thermodynamics of Formation, Reorganization, and Melting of Confined Nanometer-Sized Polymer Crystals. *Macromolecules*, 36(4), 1257–1260. <https://doi.org/10.1021/ma021434c>
- Runt, J. P. (1981). Polymer Blends Containing Isotactic Polystyrene: Thermal Behaviour of Model Systems. *Macromolecules*, 14, 420 - 423. <https://doi.org/10.1021/ma50003a035>
- Sawamura, S., Miyaji, H., Izumi, K., Sutton, S. J., & Miyamoto, Y. (1998). Growth Rate of Isotactic Polystyrene Crystals in Thin Films. *Journal of the Physical Society of Japan*, 67(10), 3338 – 3341. <https://doi.org/10.1143/JPSJ.67.3338>
- Schäffer, E. (2001). *Instabilities in Thin Polymer Films: Structure Formation and Pattern Transfer*. PhD dissertation, University of Konstanz, Germany.
- Schäffer, E., Harkema, S., Blossey, R., & Steiner, U. (2002). Temperature-gradient-induced instability in polymer films. *Eur. Phys. Lett.*, 60 255. <https://doi.org/10.1209/epl/i2002-00344-9>
- Schluze, M., Handge, A. U., Abetz, V. (2017). Preparation and Characterization of Open-Celled Foams using Polystyrene-b-Poly(4-vinylpyridine) and Poly(4-methylstyrene)-b-Poly(4-vinylpyridine) Diblock Copolymers. *Polymer*, 108, 400 – 412. <https://doi.org/10.1016/j.polymer.2016.12.005>
- Schneider, C. A.; Rasband, W. S.; Eliceiri, K. W. (2012). NIH Image to ImageJ: 25 Years of Image Analysis. *Nat. Methods*, 9, 671 - 675. <https://doi.org/10.1038/nmeth.2089>
- Schubert, D. W. (1997). Spin-Coating as a Method for Polymer Molecular Weight Determination. *Polymer Bulletin*, 38, 177 – 184. <https://doi.org/10.1007/s002890050035>
- Şenocak, A., Alkan, C., & Karadağ, A. (2016). Thermal Decomposition and a Kinetic Study of Poly(*Para*-Substituted Styrene)s. *American Journal of Analytical Chemistry*, 7, 246 – 253. <https://doi.org/10.4236/ajac.2016.73021>

- Sharma, A. (2001). Auto-Optimization of Dewetting Rates by Rim Instabilities in Slipping Polymer Films. *Physical Review Letters*, 87, 166103. <https://doi.org/10.1103/PhysRevLett.87.166103>
- Sharma, A., & Reiter, G. (1996). Instability of Thin Polymer Films on Coated Substrates: Rupture, Dewetting, and Drop Formation. *Journal of Colloid and Interface Science*, 178(2), 383 – 399. <https://doi.org/10.1006/jcis.1996.0133>
- Shu, H. L., & Woo, E. M. (2006). Miscibility in Blends of Isotactic/Syndiotactic Polystyrenes at Melt or Quenched Amorphous. *Macromolecular Materials and Engineering*, 291(11), 1397 – 1406. <https://doi.org/10.1002/mame.200600240>
- Sommer, J.-U., & Reiter, G. (2005). Crystallization in Ultra-Thin Polymer Films. *Thermochimica Acta*, 432(2), 135 – 147. <https://doi.org/10.1016/j.tca.2005.04.017>
- Stroeks, Alexander, & Nies, E. (1990). A Modified Hole Theory of Polymeric Fluids. 2. Miscibility Behaviour and Pressure Dependence of the System Polystyrene/Cyclohexane. *Macromolecules*, 23(18), 4092 – 4098. <https://doi.org/10.1021/ma00220a011>
- Stroeks, A., Paquaij, R., & Nies, E. (1991). Miscibility Behaviour of the System Polystyrene/Poly(*p*-methylstyrene). *Polymer*, 32(14), 2653 - 2658. [https://doi.org/10.1016/0032-3861\(91\)90347-L](https://doi.org/10.1016/0032-3861(91)90347-L)
- Sunthar, P. (2010). Polymer Rheology. In *Rheology of Complex Fluids*. Springer-Verlag: Germany. https://doi.org/10.1007/978-1-4419-6494-6_8
- Sutton, S. J., Izumi, K., Miyaji, H., Miyamoto, Y., & Miyashita, S. (1997). The Morphology of Isotactic Polystyrene Crystals Grown in Thin Films: The Effect of Substrate Material. *Journal of Materials Science*, 32, 21, 5621 - 5627. <https://doi.org/10.1023/A:1018688827486>
- Taguchi, K., Miyamoto, Y. & Toda, A. (2019). Molecular Weight Dependence of Crystal Growth in Isotactic Polystyrene Ultrathin Films. *ACS Macro Lett.*, 8(10), 1227–1232. <https://doi.org/10.1021/acsmacrolett.9b00516>
- Tanaka, G., Imai, S. & Yamakawa, H. (1970). Experimental Test of the Two-Parameter Theory of Dilute Polymer Solutions: Poly- *p* -methylstyrene. *J. Chem. Phys.*, 52(5), 2639 - 2650. <https://doi.org/10.1063/1.1673352>
- Thomas, K. R., Chenneviere, A., Reiter, G., & Steiner, U. (2011). Nonequilibrium Behaviour of Thin Polymer Films. *Physical Review E - Statistical, Nonlinear, and Soft Matter Physics*, 83(2), 021804. <https://doi.org/10.1103/PhysRevE.83.021804>
- Thomas, S., Grohens, Y., & Jyotishkumar, P. (2015). *Characterization of Polymer Blends: Miscibility, Morphology and Interfaces*. Second Ed., Wiley - VCH: Toronto. <https://doi.org/10.1002/9783527645602>
- Utracki, L. A. (2003). Introduction to Polymer Blends. In *Polymer Blends Handbook*. Springer-Verlag: Germany. https://doi.org/10.1007/0-306-48244-4_1

- Utracki, Leszek A., & Wilkie, C. A. (2014). Polymer Blends Handbook. In *Polymer Blends Handbook*. Springer-Verlag: Germany. <https://doi.org/10.1007/978-94-007-6064-6>
- Vilmin, T., & Raphaël, E. (2005). Dewetting of Thin Viscoelastic Polymer Films on Slippery Substrates. *European Physics Letters*, 72, 781 – 785. <https://doi.org/10.1209/epl/i2005-10312-y>
- Vilmin, T., & Raphaël, E. (2006). Dewetting of Thin Polymer Films. *European Physical Journal E*, 21(2), 161 – 174. <https://doi.org/10.1140/epje/i2006-10057-5>
- Vilmin, T., Raphaël, E., Damman, P., Sclavons, S., Gabriele, S., Hamieh, M., & Reiter, G. (2006). The Role of Nonlinear Friction in the Dewetting of Thin Polymer Films. *European Physics Letters*, 73, 906 – 912. <https://doi.org/10.1209/epl/i2005-10480-8>
- Wang, C., Lin, C. C., & Tseng, L. C. (2006). Miscibility, Crystallization and Morphologies of Syndiotactic Polystyrene Blends with Isotactic Polystyrene and with Atactic Polystyrene. *Polymer*, 47(1), 390 - 402. <https://doi.org/10.1016/j.polymer.2005.10.123>
- Wang, J. Shyong, & Porter, R. S. (1995). On the Viscosity-Temperature Behaviour of Polymer Melts. *Rheological Acta*, 34(5), 496 – 503. <https://doi.org/10.1007/BF00396562>
- Wu, S. (1989). Chain Structure and Entanglement. *J. Polym. Sci. Part B Polym. Phys.*, 27, 723 - 741. <https://doi.org/10.1002/polb.1989.090270401>
- Wu, T., Valencia, L., Pfohl, T., Heck, B., Reiter, G., Lutz, P. J., & Mülhaupt, R. (2019). Fully Isotactic Poly(*p*-methylstyrene): Precise Synthesis via Catalytic Polymerization and Crystallization Studies. *Macromolecules*, 52, 4839 – 4846. <https://doi.org/10.1021/acs.macromol.9b00640>
- Xenopoulos, A., Londono, J. D., Wignall, G. D., & Wunderlich, B. (1994). Phase Separation in Blends of Polystyrene and Poly(*p*-methylstyrene) using Thermal Analysis and Small - Angle Scattering. *Mat. Res. Symp. Proc.*, 321, 107 - 112. <https://doi.org/10.1557/PROC-321-107>
- Yamaguchi, M., Suzuki, K. I., & Maeda, S. (2002). Enhanced Strain Hardening in Elongational Viscosity for HDPE/Cross-linked HDPE Blend. I. Characteristics of Cross-linked HDPE. *Journal of Applied Polymer Science*, 86(1), 73 – 78. <https://doi.org/10.1002/app.10914>
- Yang, S., Xu F., Ostendorp, S., Wilde, G., Zhao, H., & Lei Y. (2011). Template-Confined Dewetting Process to Surface Nanopatterns: Fabrication, Structural Tunability, and Structure-Related Properties. *Adv. Funct. Mater.* 21, 2446 – 2455. <https://doi.org/10.1002/adfm.201002387>
- Ye, J., Zuev D. & Makarov, S. (2018). Dewetting Mechanisms and their Exploitation for the Large Fabrication of Advanced Nanophotonics Systems. *International Materials Reviews*, 1 – 36. <https://doi.org/10.1080/09506608.2018.1543832>
- Yeh, G. S. Y. & Lambert, S. L. (1972). Crystallization Kinetics of Isotactic Polystyrene from Isotactic - Atactic Polystyrene Blends. *J. Polym. Sci: Part A-2*, 10, 1183 - 1191. <https://doi.org/10.1002/pol.1972.160100701>

- Young, J. R. & Lovell, P. A. (1991). *An Introduction to Polymers*. Second Ed., Chapman and Hall: London.
- Ziebert, F., & Raphaël, E. (2009). Dewetting Dynamics of Stressed Viscoelastic Thin Polymer Films. *Physical Review E - Statistical, Nonlinear, and Soft Matter Physics*, 79, 031605. <https://doi.org/10.1103/PhysRevE.79.031605>

APPENDICES

Appendix A: Supporting information for chapter one

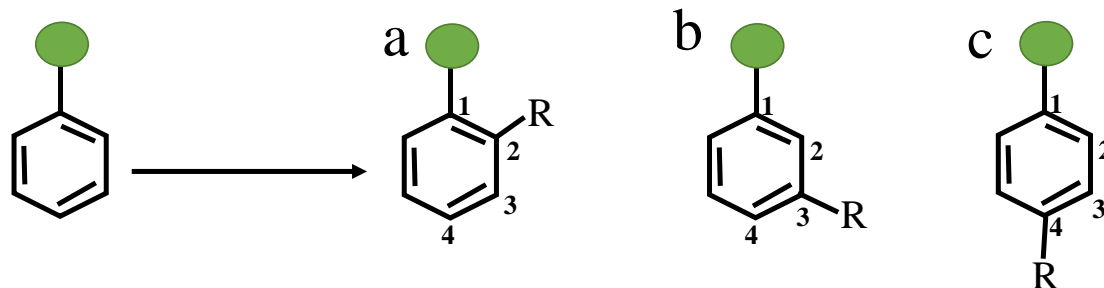


Fig. A1: Electrophilic aromatic substitution process exhibiting the (a) *ortho* [1,2]-, (b) *Meta* [1,3]- and (c) *para* [1,4]-products. The *ortho*-, and *para*-products are called major whereas the *meta*-product is referred to as minor. The numerals 1 – 4 show how the group (R) changes position.

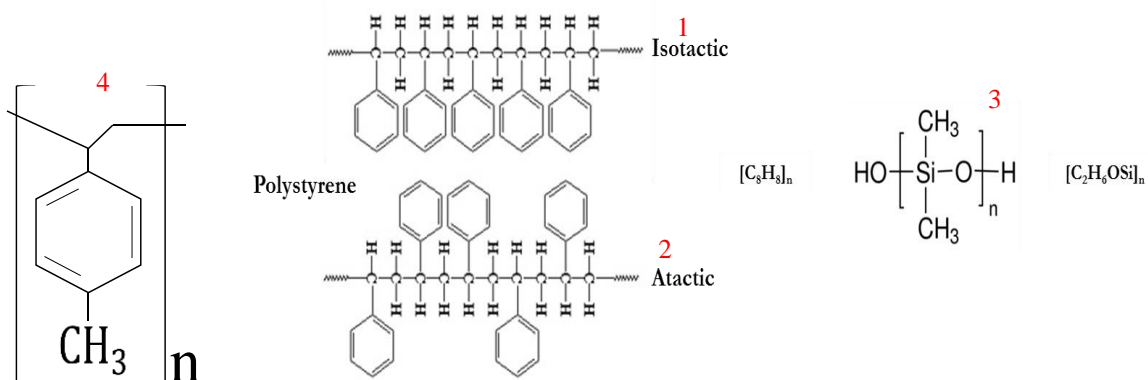


Fig. A2: Molecular structure of *iPpMS608K*, *iPS400K*, *aPS* and *PDMS* followed by their chemical formula. Image credits: www.nptel.ac.in and www.sigmaldrich.com

Appendix B: Supporting information for chapter two

Estimation of strain function from hole radius and rim width

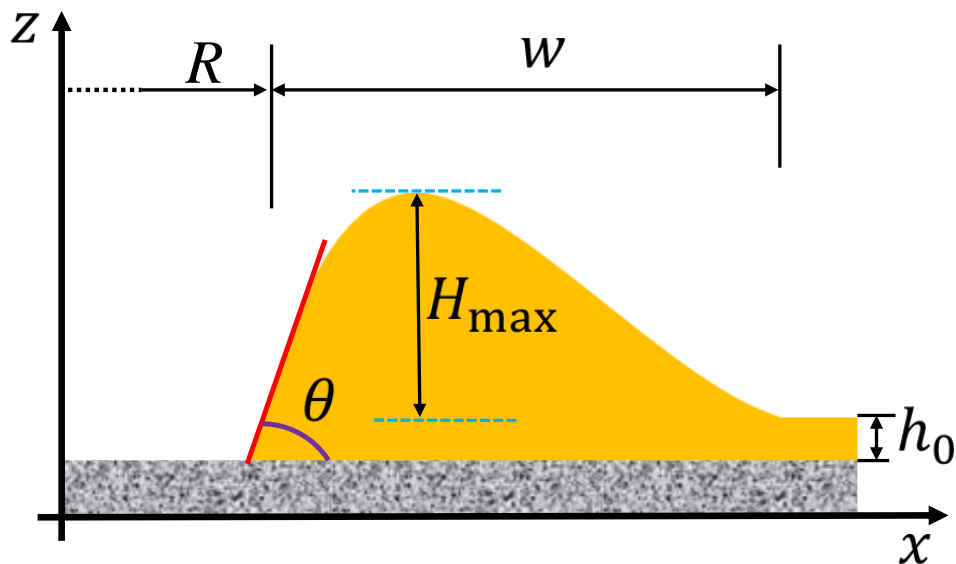


Fig. B1: Determination of maximum height of the rim in terms of the maximum width of the rim and the dewetted distance when this maximum is reached. R is the radius of the dewetted hole and w is the width of the rim, H_{\max} is the maximum height of the rim, θ is the contact angle and h_0 is the film thickness.

Based on volume conservation of an incompressible fluid, the volume of the dewetted hole, which is $\pi R^2 \cdot h_0$, has to be identical to the volume of the rim, yielding (Brochard-Wyart et al., 1994)

$$\pi R^2 \cdot h_0 = 2\pi R \int_R^{R+w} z(x) dx \approx 2\pi R \cdot w^2 \cdot \theta \cdot s \quad (\text{B1})$$

(for small θ , $\tan \theta \approx \theta$)

According to Brochard-Wyart et al. (1994) for strong slippage ($z \ll b$, with b being the slippage length), the value of $s \cong 0.1$. Approximating the cross-section of the rim by a rectangle with an area of $w \cdot H_{\text{average}}$;

$$H_{\text{average}} \approx \theta_E \cdot w \cdot s \quad (\text{B2})$$

Hence, equation (B1) yields

$$H_{\text{average}} = Rh_0/2w \quad (\text{B3})$$

At early times (in the elastic regime), the acting driving forces will deform the rim elastically, until these driving forces are balanced by the elastic restoring forces. At this point the maximum height of the rim (H_{max}) is reached. At that point, the maximum strain is defined (for the current study) as the ratio H_{max}/h_0 . Setting $H_{\text{average}} = H_{\text{max}}$ gives;

$$\varepsilon_{\text{max}} = H_{\text{max}}/h_0 = (H(\tau_{w(\text{max})}) - h_0)/h_0 = (Rh_0/2w)/h_0 = R/2w \quad (\text{B4})$$

Appendix C: Supporting information for chapter three

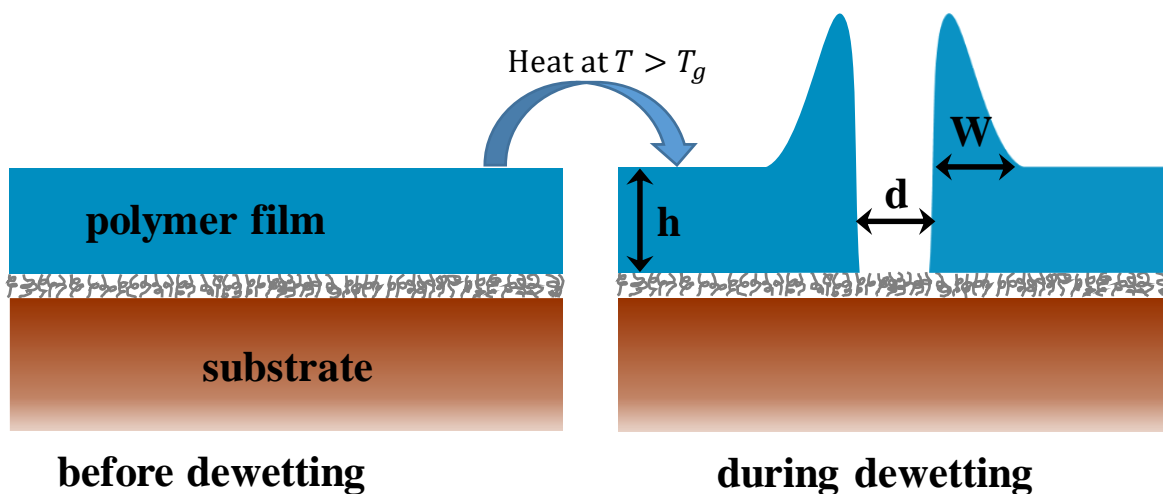


Fig. C1: A sketch showing thin films before and after dewetting (h – film thickness, d – dewetted distance, w – rim width)

Hole radius and rim width measurements in ImageJ program

ImageJ program was used to measure the hole radius of the dewetted holes for the spin-coated iPpMS608K and its iPS400K400K blend on PDMS coated silicon wafers. To start the measurements, the micrograph to be measured has to be opened on the ImageJ window. To set the scale, one has to go to ImageJ window and click on **analyze > set scale**. A dialog box pops up as shown in **Fig. C2 (numeral 2)** where the distance in pixels is entered. This tells us how many pixels correspond to 1 inch on the image. Every optical microscope has a different objective lens magnification as shown with numeral 3.

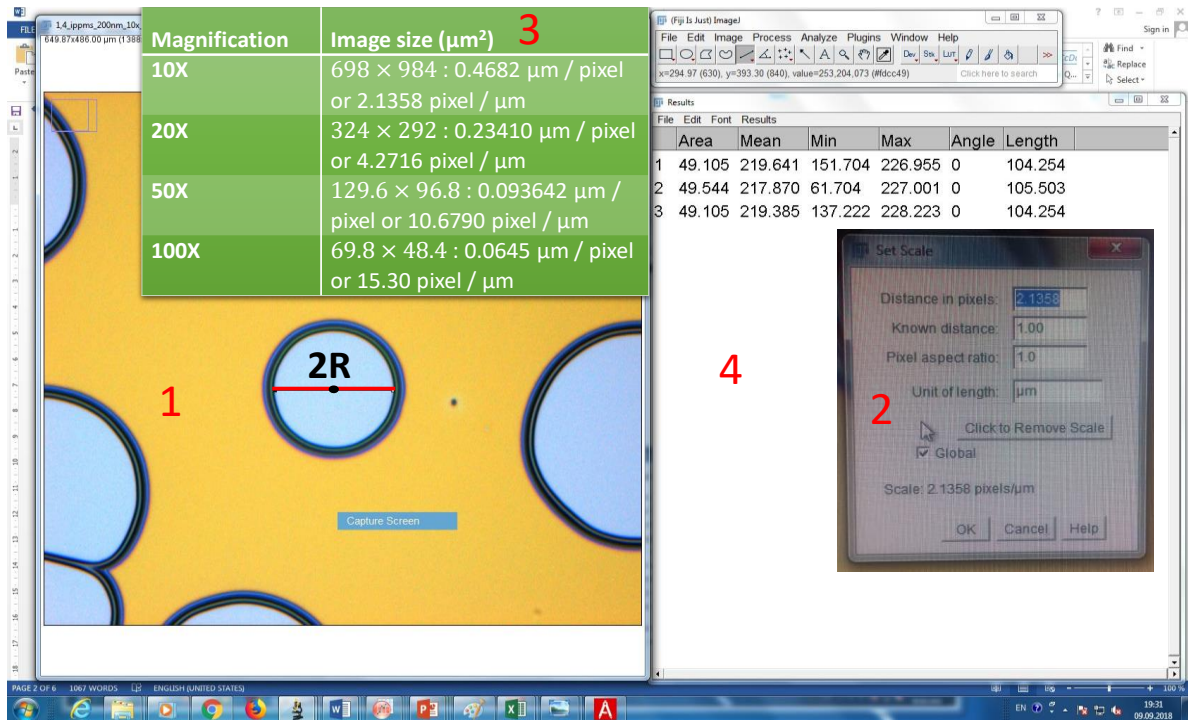


Fig. C2: Measurement of the radius of the hole and rim width using ImageJ program

To determine the diameter of the hole, at least three measurements are taken along the middle of the hole and the highest distance gives the diameter of the hole as shown in **Fig. C2 (within the measurement window – numeral 1)**. To do this, one **clicks on the straight line selection tool** on ImageJ menu and then draws a straight line from one end of the dewetted circular hole to the other end. To ensure that the line is straight, **press and hold on shift button** on the computer keyboard as you draw the line. It should also be noted that the horizontal / vertical angle along the diameter must be zero to make sure that the line is straight. To take measurement of the diameter of the hole, **press and hold on control + M** on the computer keyboard. A result box pops up displaying the length of the dewetted distance in the final column (**indicated by numeral 4 of Fig. C2**). To move to the next point of measurement, **press and hold on shift button + P** on the computer keyboard.

The diameter of the dewetted hole is then divided by 2 to obtain the radius. The rim width is measured directly using the same procedure. Although the area of the hole can be measured by ImageJ program and the radius of the hole calculated, some of the graphs reported in the earlier reports exhibited scattered dewetting velocity data at higher dewetting times. This makes it difficult to get a clear trend from the scattered data which is important in understanding the dynamics of the dewetting velocity-time relationship at higher dewetting times. The direct measurement of radius of the hole yields best results. However, at higher dewetting time, the rate at which the holes grow is low and therefore, direct measurement of radius is difficult. In this case, determination of the hole radius by finding the area of the hole becomes useful.

Error analysis in dewetting velocity

$$V(t_i) = \frac{R_i - R_{i-1}}{t_i - t_{i-1}}$$

$$V = \frac{R_2 - R_1}{t_2 - t_1}$$

$$\delta V = |V| \cdot \sqrt{\left(\frac{\delta(R_2 - R_1)}{R_2 - R_1}\right)^2 + \left(\frac{\delta(t_2 - t_1)}{t_2 - t_1}\right)^2}$$

For $\delta(t_2 - t_1) = 0$,

$$\delta V = |V| \cdot \frac{\delta(R_2 - R_1)}{|R_2 - R_1|}$$

But $\delta(R_2 - R_1) = \sqrt{(\delta R_2)^2 + (\delta R_1)^2}$,

$$\therefore \delta V = |V| \cdot \frac{\sqrt{(\delta R_2)^2 + (\delta R_1)^2}}{|R_2 - R_1|}$$

Hence,

$$\delta V = |V| \cdot \frac{\sqrt{(\delta R_i)^2 + (\delta R_{i-1})^2}}{|R_i - R_{i-1}|}$$

Steps followed in finding the incubation time

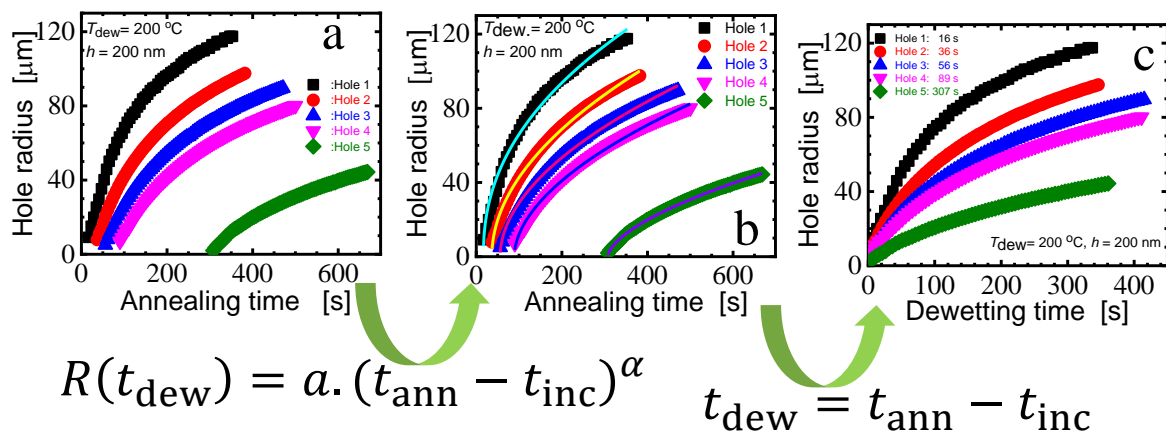


Fig. C3: Procedure for finding the incubation time and dewetting time through curve fittings.

Appendix D: Supporting information for chapter four

Activation energy calculations: Blend system

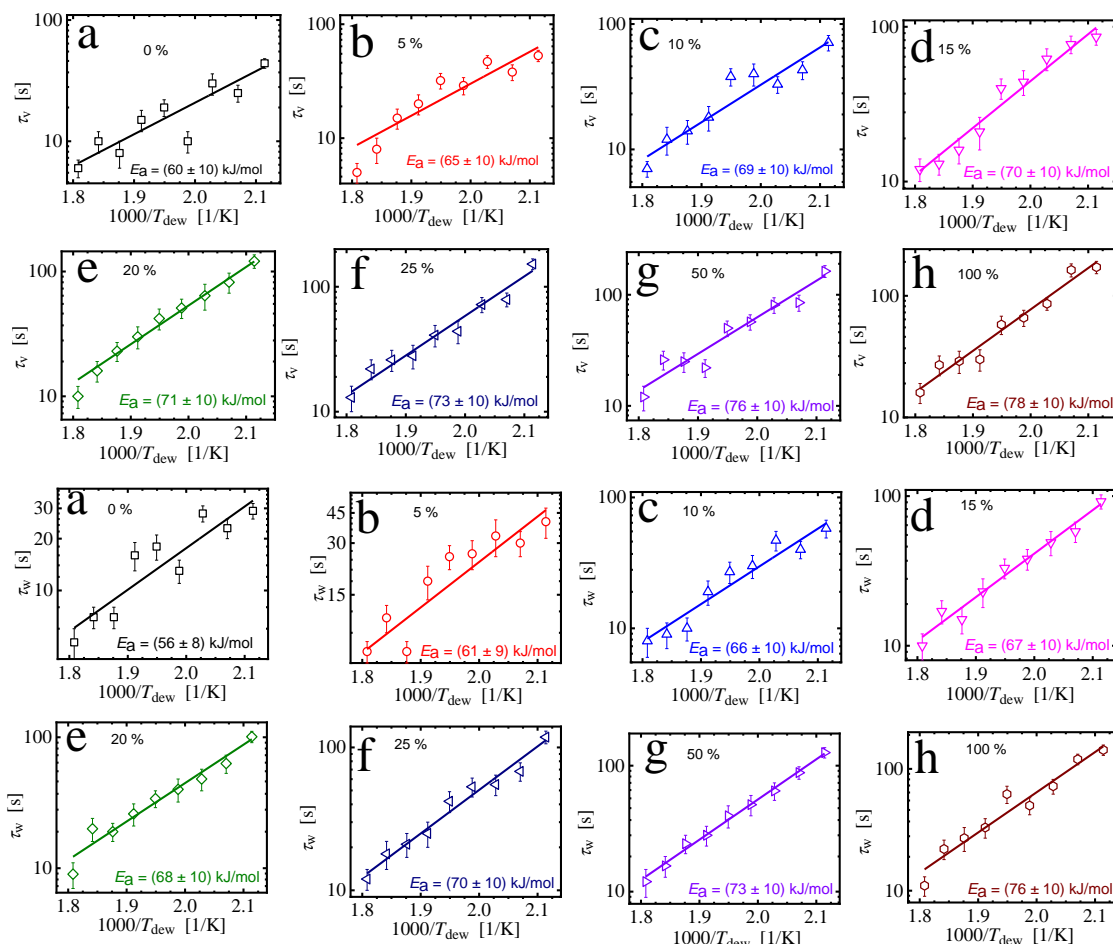


Fig. D1: Semi-logarithmic plots of relaxation time $\tau_r \in [\tau_v, \tau_w]$ as a function of $1000/T_{dew}$ at different iPS400K content. The activation energies in both cases were calculated from $\ln\tau_r = \ln\tau_0 + E_\eta/k_B T_{dew}$ or $\ln\{\tau_r\}/\tau_0 = E_a/k_B T_{dew}$ (we set $\tau_r \in \{\tau_v, \tau_w\}$, $k_B T_{dew} \equiv RT_{dew}$, $R = 8.314$ kJ/mol)

Stress calculations

To calculate stress in the prepared films, the surface energies of both isotactic polystyrene (iPS400K) and isotactic poly(*para*-methylstyrene) (iPpMS) polymers are required. Since rheological properties of both polymers has not been completely done based on literature, the surface energies of their respective atactic counterparts, aPS and aPpMS have been used.

According to reference,(Kempf et al., 2013) the surface tension γ_L of atactic poly(*para*-methylstyrene) is $\gamma_L = 25.8 \text{ mJ/m}^2$ at 20°C and that of atactic polystyrene is $\gamma_L = 28.3 \text{ mJ/m}^2$ at 20°C . For polymers, γ_L decreases with increasing temperature by ca. $-0.08 \text{ mJm}^{-2}\text{K}^{-1}$ (Kempf, Barroso & Wilhelm, 2010). For simplicity and as the exact value of γ_L for iPPMS is not known, $\gamma_L = 25.8 \text{ mJ/m}^2$ was used and $\gamma_L = 28.3 \text{ mJ/m}^2$ as a minimum value for iPS400K for the purpose of estimating the capillary stresses. Using the experimentally determined values of contact angles for holes dewetting at 240°C at different iPS400K content, Table D1 gives the calculated stresses ($\sigma_{\text{cap}} = |S|/h_0$, $|S| = \gamma_L(1 - \cos \theta_{\text{equ}})$, $\sigma_{\text{res}} = \sigma_{\text{cap}}(\overline{B}_v - 1)$, $\sigma_{\text{tot}} = \sigma_{\text{cap}} + \sigma_{\text{res}}$).

iPS400K %	θ_{dyn}	σ_{cap} kPa	$\overline{B}_v - 1$	σ_{res} kPa	σ_{tot} kPa
0	0.37	17.5	1.6	28.0	45.5
5	0.40	22.1	4.0	88.4	110.5
10	0.41	23.1	5.0	115.5	138.6
15	0.42	24.2	6.0	145.2	169.4
20	0.41	23.1	7.1	164.0	187.1
25	0.44	26.5	8.1	214.7	241.2
50	0.43	25.4	9.0	228.6	254.0
100	0.42	24.2	10.1	244.4	268.2

Table D1: Calculated values of σ_{cap} , σ_{res} , and $\sigma_{\text{tot}} = \sigma_{\text{cap}} + \sigma_{\text{res}}$ in iPPMS and the corresponding blends at $T_{\text{dew}} = 240^\circ\text{C}$. The \overline{B}_v values were taken from Table 1 of the main text.